

**AEDC-TR-11-T-2**



**HITRAN/HITEMP Spectral Databases and  
Uncertainty Propagation by Means of Monte Carlo  
Simulation with Application to Tunable Diode  
Laser Absorption Diagnostics**

**William J. Phillips  
David H. Plemmons  
Nickolas A. Galyen  
Aerospace Testing Alliance**

**February 2011**

**Technical Report for Period October 2009 – September 2010**

**Statement A: Approved for public release; distribution is unlimited.**

**ARNOLD ENGINEERING DEVELOPMENT CENTER  
ARNOLD AIR FORCE BASE, TENNESSEE  
AIR FORCE MATERIEL COMMAND  
UNITED STATES AIR FORCE**

## NOTICES

When US Government drawings, specifications, or other data are used for any purpose other than a definitely related Government procurement operation, the Government thereby incurs no responsibility nor any obligation whatsoever, and the fact that the Government may have formulated, furnished, or in any way supplied the said drawings, specifications, or other data, is not to be regarded by implication or otherwise, as in any manner licensing the holder or any other person or corporation, or conveying any rights or permission to manufacture, use, or sell any patented invention that may in any way be related thereto.

Qualified users may obtain copies of this report from the Defense Technical Information Center.

References to named commercial products in this report are not to be considered in any sense as an endorsement of the product by the United States Air Force or the Government.

## DESTRUCTION NOTICE

For unclassified, limited documents, destroy by any method that will prevent disclosure or reconstruction of the document.

## APPROVAL STATEMENT

### Prepared by:



W. J. PHILLIPS  
Aerospace Testing Alliance



D. PLEMMONS  
Aerospace Testing Alliance



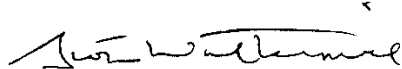
N. GALYEN  
Aerospace Testing Alliance

### Reviewed by:



CARRIE REINHOLTZ  
Project Manager  
Technology Branch (TTSY), USAF

### Approved by:



SCOTT WALTERMIRE  
Technical Director  
Technology Branch (TTSY), USAF

**REPORT DOCUMENTATION PAGE**

*Form Approved  
OMB No. 0704-0188*

The public reporting burden for this collection of information is estimated to average 1 hour per response, including the time for reviewing instructions, searching existing data sources, gathering and maintaining the data needed, and completing and reviewing the collection of information. Send comments regarding this burden estimate or any other aspect of this collection of information, including suggestions for reducing the burden, to Department of Defense, Washington Headquarters Services, Directorate for Information Operations and Reports (0704-0188), 1215 Jefferson Davis Highway, Suite 1204, Arlington, VA 22202-4302. Respondents should be aware that notwithstanding any other provision of law, no person shall be subject to any penalty for failing to comply with a collection of information if it does not display a currently valid OMB control number.

**PLEASE DO NOT RETURN YOUR FORM TO THE ABOVE ADDRESS**

<b>1. REPORT DATE (DD-MM-YYYY)</b> xx-02-2011	<b>2. REPORT TYPE</b> Technical Report	<b>3. DATES COVERED (From – To)</b> Oct. 2009 – Nov 2010
--	---	---

<b>4. TITLE AND SUBTITLE</b> HITRAN/HITEMP Spectral Databases and Uncertainty Propagation by Means of Monte Carlo Simulation with Application to Tunable Diode Laser Absorption Diagnostics	<b>5a. CONTRACT NUMBER</b>
	<b>5b. GRANT NUMBER</b>
	<b>5c. PROGRAM ELEMENT NUMBER</b>

<b>6. AUTHOR(S)</b> Phillips, William J., Plemmons, David H., and Galyen, Nickolas A. Aerospace Testing Alliance	<b>5d. PROJECT NUMBER</b> 12713
	<b>5e. TASK NUMBER</b>
	<b>5f. WORK UNIT NUMBER</b>

<b>7. PERFORMING ORGANIZATION NAME(S) AND ADDRESS(ES)</b> Arnold Engineering Development Center/TTSY Air Force Materiel Command Arnold Air Force Base, TN 37389-6000	<b>8. PERFORMING ORGANIZATION REPORT NO.</b>  AEDC-TR-11-T-2
---	--

<b>9. SPONSORING/MONITORING AGENCY NAME(S) AND ADDRESS(ES)</b> Office of Secretary of Defense (OSD) Test Resource Management Center (TRMC) Test and Evaluation/Science and Technology (T&E/S&T) Advanced Propulsion Test Technology (APTT) 1225 South Clark Street, Suite 1200, Arlington, VA 22202	<b>10. SPONSOR/MONITOR'S ACRONYM(S)</b>
	<b>11. SPONSOR/MONITOR'S REPORT NUMBER(S)</b>

**12. DISTRIBUTION/AVAILABILITY STATEMENT**  
**Statement A:** Approved for public release, distribution is unlimited.

**13. SUPPLEMENTARY NOTES**  
Available in the Defense Technical Information Center (DTIC).

**14. ABSTRACT**  
A merged HITRAN2008/HITEMP2010 spectral database and the distribution of spectral database parameters uncertainty was compiled for the two most prevalent combustion by-product gases, H<sub>2</sub>O and CO<sub>2</sub>.  
A Monte Carlo based uncertainty analysis methodology for application to tunable diode lasers or other high spectral resolution measurements was developed. This technique was applied in a sensitivity analysis of absorption measurements. Seven different representative data reduction methods were applied to four different hypothetical measurement scenarios typical of high-speed flow diagnostics. Through the use of the Monte Carlo analysis, the key input parameters that affect the uncertainty in retrieved gas temperatures, absorbing specie number density, velocity, and total number density were identified. Rough estimates of uncertainties in gas properties based on uncertainties of spectral parameters in the merged HITRAN2008/HITEMP2010 database were provided. Recommendations for further investigations, improvements, as well as guidance in the use of a Monte Carlo based analysis are presented.

**15. Subject Terms**  
HITRAN, HITEMP, spectral database, Monte Carlo, TDL, diode laser, uncertainty propagation

<b>16. SECURITY CLASSIFICATION OF:</b>			<b>17. LIMITATION OF ABSTRACT</b>	<b>18. NUMBER OF PAGES</b>	<b>19A. NAME OF RESPONSIBLE PERSON</b>
<b>A. REPORT</b>	<b>B. ABSTRACT</b>	<b>C. THIS PAGE</b>			William J. Phillips
Unclassified	Unclassified	Unclassified	Same as Report	91	<b>19B. TELEPHONE NUMBER (Include area code)</b> 931-454-4664

This page is intentionally left blank.

## **PREFACE**

The work reported herein was conducted by the Arnold Engineering Development Center (AEDC), Air Force Materiel Command (AFMC), at the request of the Test and Evaluation/Science and Technology (T&E/S&T) Advanced Propulsion Test Technology (APTT). The T&E/S&T APTT Executing Agent was Thomas Fetterhoff. The AEDC AF Project Manager was Carrie Reinholtz. The research was conducted by Aerospace Testing Alliance (ATA), the operations, maintenance, information management, and support contractor for AEDC, Arnold Air Force Base, AFMC, TN 37389. The research was conducted within the Instrumentation/Diagnostics Section of the Applied Technology Branch under Air Force Project Number 12713. The ATA Project Manager was Bonnie Heikkinen.

## **ACKNOWLEDGEMENT**

The authors would like to thank the Test Resource Management Center (TRMC) Test and Evaluation/Science and Technology (T&E/S&T) program for their support. This work is funded by T&E/S&T program through the Advance Propulsion Test Technology (APTT area.)

This page is intentionally left blank.

## CONTENTS

		<u>Page</u>
1.0	INTRODUCTION.....	7
2.0	BACKGROUND .....	8
2.1	Absorption Process .....	8
3.0	HITRAN AND HITEMP DATABASES .....	12
4.0	DATA REDUCTION .....	17
4.1	Baseline Experimental Configuration .....	17
4.2	Data Reduction Methodologies .....	19
4.2.1	Integrated Linear Absorbance (LAINT).....	19
4.2.2	Integrated Nonlinear Absorbance (NLINT) .....	20
4.2.3	Nonlinear Spectral Transmittance Curve Fit for Absorbing Specie Number Density with Measured Background (NLFIT1).....	20
4.2.4	Nonlinear Spectral Transmittance Curve Fit for Absorbing Specie Number Density with Floating Background (NLFIT2) .....	21
4.2.5	Nonlinear Spectral Transmittance Curve Fit for Absorbing Specie Number Density and Temperature with Floating Background (NLFIT3) .....	21
4.2.6	Nonlinear Spectral Transmittance Curve Fit for Absorbing Specie Number Density and Total Number Density with Floating Background (NLFIT4) .....	21
4.2.7	Nonlinear Spectral Transmittance Curve Fit for Absorbing Specie Number Density, Total Number Density, and Temperature with Floating Background (NLFIT5).....	22
5.0	ERROR PROPAGATION BY MEANS OF MONTE CARLO SIMULATION .....	22
6.0	TEST CASES .....	24
7.0	RESULTS.....	28
7.1	Case 1: O <sub>2</sub> .....	31
7.2	Case 2 and Case 3: H <sub>2</sub> O .....	43
7.3	Case 4: CO.....	61
8.0	CONCLUSIONS.....	73
9.0	RECOMMENDATIONS .....	75
10.0	SUMMARY .....	76
	REFERENCES.....	78

## FIGURES

### Figure

1. Schematic of a Simple Tunable Laser Absorption Measurement. ....	9
2. Uncertainties Associated with H <sub>2</sub> O Spectral Lines in the HITRAN 2008 Database .....	15
3. Uncertainties Associated with CO <sub>2</sub> Spectral Lines in the HITRAN 2008 Database .....	15
4. Uncertainties Associated with H <sub>2</sub> O Spectral Lines in the Merged HITRAN-2008 and HITEMP-2010 Database .....	16
5. Uncertainties Associated with CO <sub>2</sub> Spectral Lines in the Merged HITRAN-2008 and HITEMP-2010 Database .....	16
6. Schematic of Hypothetical Measurement Geometry Used in the Baseline Spectral Calculations.....	19
7. Schematic of Monte Carlo Simulation Methodology. ....	23
8. Spectral Transmittance of the Blue-Shifted 764.28-nm (13,084.203 cm <sup>-1</sup> ) O <sub>2</sub> Transition Utilized in the Work of Plemmons and Galyen and Employed in Case 1 of this Work.....	25
9. Spectral Transmittance of the Blue-Shifted H <sub>2</sub> O Absorption Features Utilized in the Work of O'Bryne and the Cases 2 and 3 Calculations of This Work.....	27
10. Spectral Transmittance of the Blue-Shifted CO Absorption Features Utilized in the Work of Lowry and Fisher and the Case 4 Calculations of This Work .....	28
11. Simulated Case 1 Data with Addition of Noise and Resultant Curve Fit .....	29
12. Simulated Data for Case 2 and Associated Curve Fit.....	29
13. Simulated Data for Case 3 and Associated Curve Fit.....	30
14. Simulated Data for Case 4 and Associated Curve Fit.....	30
15. Actual and Retrieved Average Velocities with 4,000 and 8,000 Points in the Red- and Blue-Shifted Second-Derivative Spectra (Case 1: O <sub>2</sub> ) .....	31
16. Percent Error in Mean Velocity as a Function of 2 <sup>nd</sup> Derivative Spectral Intensity Noise or Uncertainty for 4,000 and 8,000 Points Per Spectrum (Case 1: O <sub>2</sub> ).....	32
17. Uncertainty in Velocity as a Percent of the Mean Velocity vs. the Uncertainty in the 2 <sup>nd</sup> Derivative Spectral Intensity for 4,000 and 8,000 Points Per Spectra (Case 1: O <sub>2</sub> ).....	32
18. Actual and Mean Number Densities Retrieved from the MC Analysis Using the Seven Data Reduction Methodologies as a Function of Uncertainty in the Spectral Line Strength (Case 1: O <sub>2</sub> ).....	33
19. Percent Error in Retrieved O <sub>2</sub> Number Density as a Function of Uncertainty in the Spectral Line Strength (Case 1: O <sub>2</sub> ).....	34
20. Uncertainty in Retrieved O <sub>2</sub> Number Density as a Function of Uncertainty in the Spectral Line Strength for Various Data Reduction Methodologies (Case 1: O <sub>2</sub> ) .....	34
21. Actual and Mean Values of Mass Flux as a Function of Uncertainty in the Spectral Line Strength for Various Data Reduction Methodologies (Case 1: O <sub>2</sub> ) .....	35
22. Percent Error in Retrieved Mass Flux as a Function of Uncertainty in the Spectral Line Strength (Case 1: O <sub>2</sub> ).....	36

23. Uncertainty in Retrieved Mass Flux as a Function of Uncertainty in the Spectral Line Strength for Various Data Reduction Methodologies (Case 1: O <sub>2</sub> ) .....	36
24. Uncertainty in Retrieved Mass Flux as a Function of Uncertainty in the Spectral Line Foreign Gas Broadening Parameter for Various Data Reduction Methodologies (Case 1: O <sub>2</sub> ) .....	37
25. Uncertainty in Retrieved Mass Flux as a Function of Uncertainty in the Spectral Line Self-(O <sub>2</sub> ) Broadening Parameter for Various Data Reduction Methodologies (Case 1: O <sub>2</sub> ) .....	37
26. Uncertainty in Retrieved Total Specie Number Density as a Function of Uncertainty in the Pressure Broadening Parameter (Case 1: O <sub>2</sub> ) .....	39
27. Uncertainty in Retrieved Total Number Density as a Function of Uncertainty in Broadening Temperature Correction Exponent (Case 1: O <sub>2</sub> ).....	39
28. Uncertainty in Retrieved Absorbing Specie Number Density as a Function of Uncertainty in the Spectral Line Width Temperature Adjustment Exponent for Various Data Reduction Methodologies (Case 1: O <sub>2</sub> ).....	40
29. Uncertainty in Retrieved Absorbing Specie Number Density as a Function of Uncertainty in the Temperature (Case 1: O <sub>2</sub> ).....	40
30. Uncertainty in Retrieved Absorbing Specie Number Density as a Function of Uncertainty in the Mean Background Level (Case 1: O <sub>2</sub> ).....	41
31. Uncertainty in Retrieved Absorbing Specie Number Density as a Function of Uncertainty in Intensity (Case 1: O <sub>2</sub> ).....	42
32. Uncertainty in Retrieved Temperature as a Function of Uncertainty in the Air or Foreign Gas Broadening Parameter (Case 1: O <sub>2</sub> ) .....	43
33. Error in Retrieved Velocity a Function of Uncertainty in the Second-Derivative Spectral Intensity for Case 2 (1,000 K) and Case 3 (2,000 K) Conditions .....	44
34. Uncertainty in Retrieved Velocity a Function of Uncertainty in the Second-Derivative Spectral Intensity for Case 2 (1,000 K) and Case 3 (2,000 K) Conditions .....	45
35. Retrieved Absorbing Specie Number Density vs. Uncertainty in Line Strength for Case 2 Condition at 1,000 K .....	47
36. Retrieved Absorbing Specie Number Density Error vs. Uncertainty in Line Strength for Case 2 Condition at 1,000 K.....	47
37. Uncertainty in Retrieved Absorbing Specie Number Density Error vs. Uncertainty in Line Strength for Case 2 Condition at 1,000 K.....	48
38. Retrieved Absorbing Specie Number Density vs. Uncertainty in Line Strength of for Case 3 Condition at 2,000 K.....	48
39. Retrieved Absorbing Specie Number Density Error vs. Uncertainty in Line Strength for Case 3 Condition at 2,000 K.....	49
40. Uncertainty in Retrieved Absorbing Specie Number Density Error vs. Uncertainty in Line Strength for Case 3 Condition at 2,000 K.....	49
41. Actual and Retrieved Temperature for Case 2 (1,000 K) and Case 2 (2,000 K) Conditions vs. Uncertainty in Line Strengths .....	50

42. Error in Average Retrieved Temperatures for Case 2 (1,000 K) and Case 2 (2,000 K) Conditions vs. Uncertainty in Line Strengths ..... 50

43. Uncertainty in Retrieved Temperature for Case 2 (1,000 K) and Case 3 (2,000 K) Conditions vs. Uncertainty in Line Strength ..... 51

44. Uncertainty in Retrieved Absorbing Specie Number Density For Case 2 (1,000 K) vs. Uncertainty in Air Pressure Broadening Parameters ..... 51

45. Uncertainty in Retrieved Temperature for Cases 2 and 3 (1,000 K and 2,000 K) vs. Uncertainty in the Air Pressure Broadening Parameter ..... 52

46. Uncertainty in Retrieved Temperature for Cases 2 and 3 (1,000 K and 2,000 K) vs. Uncertainty in the Air Pressure Broadening Parameter Temperature Correction Exponent ..... 52

47. Actual and Retrieved Mean Total Number Densities for Cases 2 and 3 (1,000 K and 2,000 K) vs. Uncertainty in the Air Pressure Broadening Parameter ..... 53

48. Uncertainty in Total Number Densities for Cases 2 and 3 (1,000 K and 2,000 K) vs Uncertainty in the Air Pressure Broadening Parameter..... 53

49. Uncertainty in Total Number Densities for Cases 2 and 3 (1,000 K and 2,000 K) vs. Uncertainty in the Air Pressure Broadening Parameter Temperature Correction Exponent ..... 54

50. Actual and Retrieved Total Number Densities for Cases 2 and 3 (1,000 K and 2,000 K) vs. Uncertainty in Spectral Line Strength Parameter ..... 54

51. Uncertainty in Retrieved Total Number Densities for Cases 2 and 3 (1,000 K and 2,000 K) vs. Uncertainty in Spectral Line Strength Parameter ..... 55

52. Actual and Retrieved Absorbing Specie Number Density for Case 2 (1,000 K) Conditions vs. Uncertainty in the Mean Background Intensity Level ..... 56

53. Actual and Retrieved Absorbing Specie Number Density for Case 3 (2,000 K) Conditions vs. Uncertainty in the Mean Background Intensity Level ..... 56

54. Uncertainty in Absorbing Specie Number Density for Case 2 (1,000 K) Conditions vs. Uncertainty in the Mean Background Intensity Level ..... 57

55. Uncertainty in Absorbing Specie Number Density for Case 3 (2,000 K) Conditions vs. Uncertainty in the Mean Background Intensity Level ..... 57

56. Actual and Retrieved Absorbing Specie Number Density for Case 2 (1,000 K) Conditions vs. Uncertainty in the Intensity Level..... 58

57. Actual and Retrieved Absorbing Specie Number Density for Case 3 (2,000 K) Conditions vs. Uncertainty in the Intensity Level..... 59

58. Uncertainty in Absorbing Specie Number Density vs. Uncertainty in the Intensity for Test Case 2 (1,000 K)..... 59

59. Uncertainty in Absorbing Specie Number Density vs. Uncertainty in the Intensity for Test Case 3 (2,000 K)..... 60

60. Uncertainty in Retrieved Temperature vs. Uncertainty in the Intensity Level for Case 2 (1,000 K) and Case 3 (2,000 K) Conditions ..... 60

61. Uncertainty in Retrieved Total Number Density vs. Uncertainty in the Intensity Level for Case 2 (1,000 K) and Case 3 (2,000 K) Conditions..... 61

62. Error in Retrieved Velocity a Function of Uncertainty in the Second-Derivative Spectral Intensity for Case 4 .....	64
63. Uncertainty in Retrieved Velocity a Function of Uncertainty in the Second-Derivative Spectral Intensity for Case 4 .....	64
64. Retrieved Absorbing Specie Number Density vs. Uncertainty in Line Strength for CO Absorption Case 4 Condition at 2,000 K .....	65
65. Retrieved Absorbing Specie Number Density Error vs. Uncertainty in Line Strength for CO Absorption Case 4 Condition at 2,000 K .....	65
66. Uncertainty in Retrieved Absorbing Specie Number Density Error vs. Uncertainty in Line Strength for the CO Absorption Case 4 Condition at 2,000 K .....	66
67. Uncertainty in Mass Flux for Test Case 4 (CO, 2,000 K) Conditions vs. Uncertainty in the Line Strength .....	66
68. Actual and Retrieved Temperature for Case 4 (CO, 2,000 K) Conditions vs. Uncertainty In Line Strengths .....	67
69. Error in Average Retrieved Temperatures for Case 4 (CO, 2,000 K) and Conditions vs. Uncertainty in Line Strengths .....	67
70. Uncertainty in Retrieved Temperature for Case 4 (CO 2,000 K) Conditions vs. Uncertainty In Line Strength .....	68
71. Actual and Retrieved Total Number Density for Test Case 4 (CO, 2,000 K) Conditions vs. Uncertainty In Line Strength .....	68
72. Error in Mean Total Number Density for Test Case 4 (CO, 2,000 K) Conditions vs. Uncertainty In Line Strength .....	69
73. Uncertainty in Total Number Density for Test Case 4 (CO, 2,000 K) Conditions vs. Uncertainty In Line Strength .....	69
74. Uncertainty in Total Number Density for Test Case 4 (CO, 2,000 K) Conditions vs. Uncertainty In Air Broadening Parameter .....	70
75. Uncertainty in Total Number Density for Test Case 4 (CO, 2,000 K) Conditions vs. Uncertainty In Pressure Broadening Temperature Correction Exponent .....	70
76. Absorbing Specie Number Density for Test Case 4 (CO, 2,000 K) Conditions vs. Uncertainty In Mean Background Level .....	71
77. Uncertainty in Absorbing Specie Number Density for Test Case 4 (CO, 2,000 K) Conditions vs. Uncertainty In Mean Background Level .....	71
78. Uncertainty in Absorbing Specie Number Density for Test Case 4 (CO, 2,000 K) Conditions vs. Uncertainty In Mean Background Level .....	72
79. Uncertainty in Retrieved Temperature for Test Case 4 (CO, 2,000 K) Conditions vs. Uncertainty in the Spectrum .....	72
80. Uncertainty in Retrieved Total Number Density for Test Case 4 (CO, 2,000 K) Conditions vs. Uncertainty in the Spectrum .....	73

## TABLES

### Table

1. Statistics of HITRAN-2008 Spectral Database.....	13
2. Statistics of Merged HITRAN-2008 and HITEMP-2010 Spectral Database .....	14
3. List of Various Test Case Conditions .....	24
4. Molecular Spectral Parameters from HITRAN 2008 Used in Monte Carlo Simulations.....	26

## APPENDICES

### Appendix

A. Wavelength Modulated Spectroscopy .....	81
B. Wing Correction to Integrated Absorbance Calculations .....	85
C. Predominate Spectral Line Profiles .....	86
 NOMENCLATURE .....	 91

## 1.0 INTRODUCTION

Optical-based gas diagnostics plays a pivotal role in flow characterization in the modern aerodynamic and aeropropulsion test community. (Refs. 1-7) Whether it is applied to measurements of humidity in an aerodynamic wind tunnel, mass flow in a vehicle or facility, or quantification of specie concentration for combustion efficiency determination, optical diagnostics is gaining acceptance as a key Test and Evaluation (T&E) diagnostic tool. Although the area of optical diagnostics is extremely diverse with techniques such as coherent Anti-Stokes Raman spectroscopy (CARS), laser-induced fluorescence (LIF) spectroscopy, and absorption spectroscopy, the attention here will be devoted totally to absorption spectroscopy, particularly to laser absorption spectroscopy, which currently composes the widest application in optical spectroscopic-based diagnostics. Note that many of the ensuing discussions are applicable to other optical diagnostic techniques that rely on high to moderate spectral resolution such as Fourier transform infrared (FTIR) spectroscopy.

The gaining acceptance of optical diagnostics is due in no small part to the development of more robust systems and software for the acquisition of these data. The advent of the digital computer and a frequency stabilized laser make FTIR spectroscopy a routine staple in gas metrology. FTIR is also the instrument of choice for acquisition of remote spectral signature data acquisition due to its relatively high optical throughput. The development of tunable diode laser (TDL) systems has greatly increased the ability to nonintrusively probe flow fields to ascertain a plethora of parameters including specie concentration, temperature, velocity, and pressure. Early TDL systems with sufficiently high spectral resolution such as the Pb-salt laser showed early promise and were routinely applied in a laboratory environment for mid-infrared applications. (Refs. 8-11) However, they suffered from several issues including lack of reliability, repeatability, output power, and the need for cryogenic cooling. The growth of the telecommunication industry led to a sizable investment in near-infrared TDLs. By the 1980s near-infrared systems capable of gas diagnostics measurements were becoming available on the commercial market. These lasers are now routinely used for many gas diagnostics measurements. The availability of low light loss fiber optics in the near-infrared has made the use of near-infrared TDL even more palatable by providing optical access in testing environments not previously possible. In recent years, the quantum cascade laser (QCL), initially developed by Lucent Laboratories, has been commercially available and is applied to many gas diagnostics applications. (Refs. 12-17) Its relatively high output power, narrow spectral line-width, ability to operate without the need for cryogenics, and operation in mid-IR spectral range makes it a very valuable tool for current and future ground-test and flight-test applications.

Typical test and evaluation customers are accustomed to obtaining data with stated uncertainties. If optical diagnostics is to mature and gain additional acceptance in the T&E community, it is necessary to gain insight into the uncertainty in the parameters retrieved by these systems. Assigning uncertainties to these parameters via a "one size fits all" approach is untenable due to the wide diversity of data acquisition and analysis methods. Applications of absorption spectroscopy across the T&E community provide a wide spectrum of measurement conditions with widely different species of interest, temperature ranges, pressure ranges, and velocities. In addition, the development of robust commercially available and custom-developed instrumentation necessitates the continuing evolution of data analysis methodologies to take full advantage of new instrumentation capabilities. Therefore, it is too early in the technological maturation process to define specific data reduction methodologies. However, a thorough investigation into uncertainty propagation provides much needed guidance. Such analyses provide valuable insight into what specific input data, measurement parameters, and/or

instrumentation have the greatest impact on the retrieved data uncertainty. In addition, these analyses can result in finding flaws and strengths of certain data reduction methodologies for specific test conditions. These insights are invaluable to both the researchers trying to provide the best possible data to the test customer and to the science and technology program managers by identifying those technological short falls that require continued development.

This report describes a detailed study on several of the key parameters affecting the uncertainty of high-resolution, spectroscopic-based flow diagnostics. It is beyond the scope of this work to address all possible scenarios. The approach taken here is to provide some guidance into what key parameters affect the data obtained from TDL diagnostics or similar systems. Special attention is given to the HITRAN/HITEMP molecular spectral parameter database. As will be seen in the following discussions, these fundamental molecular parameters play a pivotal role in defining the overall accuracy of spectroscopic-based diagnostics. The approach taken to address uncertainty analysis is through the use of Monte Carlo statistical-based analysis. The Monte Carlo technique was chosen due to its robustness and ability to easily propagate uncertainties through physics based models and data analysis algorithms that are not necessarily deterministic in nature. The reader will find there is ample room for improvement and refinement. Many sources of error in “real world” applications are not addressed here due to the limited scope and resources associated with this effort. These include uncertainty in retrieved flow parameters due to a nonuniform flow field, specific instrumentation-related issues such as limited temporal/frequency response and digitization error, and detailed refinements in spectral line shapes such as Dicke spectral line narrowing, spectral line mixing, or line shape models.

## 2.0 BACKGROUND

### 2.1 ABSORPTION PROCESS

The absorption process through a homogenous gas is governed by the Lambert-Beer law given by

$$I(\omega) = I^o(\omega)e^{-k(\omega)} \quad (1)$$

where  $I^o(\omega)$  represents the incident intensity at optical frequency,  $\omega$  ( $\text{cm}^{-1}$ ),  $I(\omega)$  is the transmitted intensity, and  $k(\omega)$  is the absorbance. Figure 1 schematically illustrates a simple absorption measurement. The absorbance carries the pressure, temperature, concentration, path length, velocity, and molecular specific parameter functional dependence. Most of the physics of the absorption process are inherent in the absorbance. The absorbance can be represented to a very high degree of accuracy by

$$k(\omega) = \sum_{\alpha} \sum_j S_{\alpha,i} f_{\alpha,i}(\omega) \quad (2)$$

where  $S_{\alpha,i}$  is the integrated absorbance of the  $i^{\text{th}}$  spectral line of the  $\alpha^{\text{th}}$  specie and  $f_{\alpha,i}(\omega)$  is the line shape function (cm) which has a unity integral normal

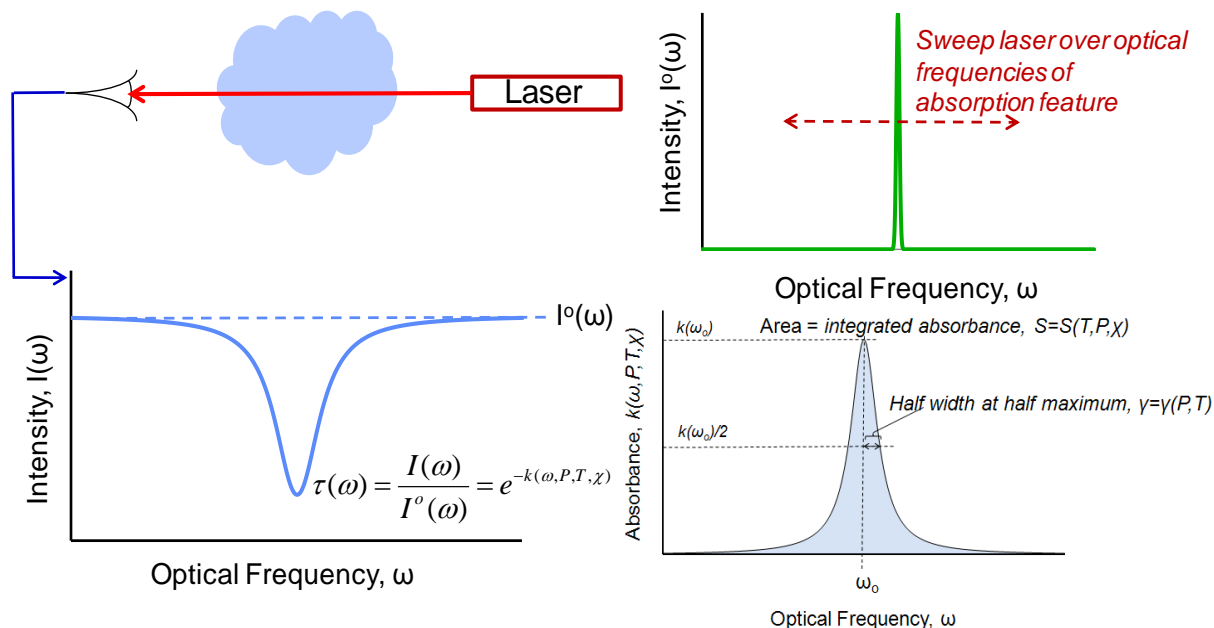


**Figure 1. Schematic of a Simple Tunable Laser Absorption Measurement**

$$\int f_{\alpha,i}(\omega) d\omega = 1 \quad (3)$$

The integrated absorbance can be expressed in terms of the line strength,  $S^o$ , with units of  $\text{cm}^{-1}/[\text{molecules}/\text{cm}^2]$

$$S_{\alpha,i} = N_{\alpha} l S_{\alpha,i}^o \quad (4)$$

where  $l$  is the path length (centimeters) and  $N_{\alpha}$  is the molecular number density ( $\text{molecules}/\text{cm}^3$ ) of the  $\alpha^{\text{th}}$  specie. The product  $N_{\alpha} l$  is sometimes referred to as the column density ( $\text{molecules}/\text{cm}^2$ ). This can be put into a functional form depending on pressure and mole fraction of the absorbing species given by

$$S_{\alpha,i} = \chi_{\alpha} \frac{P}{kT} l S_{\alpha,i}^o \quad (5)$$

where  $P$  is the pressure ( $\text{dynes}/\text{cm}^2$ ),  $\chi_{\alpha}$  is the mole fraction of the  $\alpha^{\text{th}}$  specie, and  $k$  is Boltzmann's constant.

The line strength is temperature dependent, pressure independent, proportional to the Boltzmann distribution of the initial state of the transition (lower state for absorption), and proportional to the transition probability for the transition. Since the line strength is temperature dependent it is usually quoted at some reference temperature, typically 296 K. The line strength at other temperatures can be determined by adjusting the line strength at a specified reference temperature,  $T_0$ . This is done by multiplying the line strength at a reference temperature by the ratio of the Boltzmann distribution and stimulated emission terms at temperature  $T$  and the reference temperature  $T_0$ . This is expressed as

$$S_{\alpha,i}^0(T) = S_{\alpha,i}^0(T_0) \frac{e^{-E_{\alpha,i}hc/kT} Q_{\alpha}(T_0) (1 - e^{-\frac{\omega_0 hc}{kT}})}{e^{-E_{\alpha,i}hc/kT_0} Q_{\alpha}(T) (1 - e^{-\frac{\omega_0 hc}{kT_0}}} \quad (8)$$

where  $E_i$  is the lower state energy of the transition ( $\text{cm}^{-1}$ ),  $h$  is Planck's constant,  $c$  is the speed of light in a vacuum, and  $Q_{\alpha}(T)$  is the partition function for the absorbing specie given by

$$Q_{\alpha}(T) = \sum_{i=\text{all states}} g_{\alpha,i} e^{-E_{\alpha,i}hc/kT} \quad (9)$$

where  $g_{\alpha,i}$  is the degeneracy of the  $i^{\text{th}}$  energy state and  $k$  is Boltzmann's constant. The partition function is typically tabulated for each specie as a function of temperature.

The choice of line shape function is currently a debated issue. However, most investigators utilize one of three options: Doppler profile, Lorentz profile, or Voigt profile. The Doppler profile is derived by considering the Doppler optical frequency shift due to the relative velocity of the absorbing molecule and then applying the Maxwellian distribution of velocities. The resultant profile is given by

$$f_i(\omega) = \frac{\sqrt{\ln 2}}{\gamma_D \sqrt{\pi}} e^{-\ln 2 \frac{(\omega - \omega_i)^2}{\gamma_D^2}} \quad (10)$$

where  $\omega_i$  is the optical frequency of the line center ( $\text{cm}^{-1}$ ) and  $\gamma_D$  is the Doppler half-width at half-maximum (HWHM) given by

$$\gamma_D = \frac{\omega_i}{c} \sqrt{\frac{2kN_A T \ln 2}{M_W}} \quad (\text{cm}^{-1}) \quad (11)$$

where  $N_A$ ,  $M_W$ , and  $c$  are Avogadro's number, the molecular weight, and the speed of light in vacuum, respectively.

The Lorentz profile can be obtained by considering the perturbation of the upper and lower energy levels of the absorbing molecule while undergoing collisions with other molecules. The perturbations shift quantum state levels both up and down, giving rise to a range of transitions possible between two otherwise degenerate energy states. The Lorentz profile is given by

$$f_i(\omega) = \frac{\gamma_{L,i}}{\pi [(\omega - \omega_i)^2 + \gamma_{L,i}^2]} \quad (\text{cm}) \quad (12)$$

where  $\gamma_L$  represents the collisional-induced, or pressure-broadening, HWHM. This pressure-broadened HWHM is a function of temperature and partial pressures. The pressure-induced shift is ignored here as it is generally small and its neglect does not represent any appreciable effect in the following discourse. The pressure dependence of the Lorentz HWHM is given by

$$\gamma_{L,i}(T, P) = \sum_{\beta=\text{all specie}} P_{\beta} \gamma_{L,i,\beta}^0(T) \quad (13)$$

Here,  $P_\beta$  is the partial pressure of the  $\beta^{\text{th}}$  specie in atmospheres and  $\gamma_{L,i,\beta}^o(T)$  is the pressure-broadening parameter at temperature T for the  $i^{\text{th}}$  spectral line perturbed by the  $\beta^{\text{th}}$  specie. The broadening parameters are generally quoted at some reference temperature, typically 296 K, and then corrected to the appropriate temperature using the semi-empirical temperature correction given by (Ref. 18)

$$\gamma_L^o(T) = \gamma_L^o(T_o) \left( \frac{T_o}{T} \right)^\eta \quad (14)$$

The temperature correction exponent generally has values near 0.75.

The Voigt profile is the convolution of the Doppler and Lorentz profile and is the most widely applicable profile. Close examination of spectra have shown that these are not extremely accurate in many applications where one needs to address spectral line mixing and molecular collision velocity effects. However, for many applications involving isolated spectral lines the Voigt profile is sufficient to first order and will be used in the remaining analysis. The Voigt profile is given by

$$f(\omega) = \frac{\sqrt{\ln 2} a}{\gamma_D \sqrt{\pi} \pi} \int_{-\infty}^{\infty} \frac{e^{-y^2}}{(x-y)^2 + a^2} dy \quad (15)$$

where

$$a = \sqrt{\ln 2} \frac{\gamma_L}{\gamma_D} \quad (16)$$

$$x = \sqrt{\ln 2} \frac{\omega - \omega_i}{\gamma_D} \quad (17)$$

The Voigt profile can be expressed in terms of the complex error function that can be readily calculated using many different proposed algorithms (Refs. 19-21). The form of the Voigt profile used in the following calculations is that of Humlicek (Ref. 19). The effects of an extreme range of temperatures and pressures is illustrated in Appendix C.

It should be noted that in the preceding discussions it has been assumed that the bulk gas velocity is zero. To account for a Doppler shift due to the gas bulk velocity, one needs only to Doppler shift the spectral line location. The Doppler shift for a spectral line for nonrelativistic speeds ( $v/c \ll 1$ ) can be approximated as

$$\Delta\omega = \omega_i \frac{v}{c} \quad (18)$$

where  $v$  is the component of the velocity along the optical line-of-sight. The new spectral line center position of a moving gas can then be given by

$$\omega_i \rightarrow \omega_i - \omega_i \frac{v}{c} \cos\theta \quad (19)$$

where  $v$  and  $\theta$  represent the bulk gas speed and the angle between the gas velocity and the light propagation vector.

Note that in all the preceding discussions it has been assumed that the absorbing media is homogenous in temperature, pressure, velocity, and concentration. The following discussions are restricted to homogenous paths since the intent here is to shed light on what specific input parameters, spectral data, or instrumentation parameters may have the greatest effect on retrieved gas properties of interest. Effects of flow nonuniformity are better addressed on a “by application” basis as the shape of the flow parameter spatial distribution is application specific.

### 3.0 HITRAN AND HITEMP DATABASES

It is apparent from the above discussion that any data reduction or modeling of spectral absorption is highly dependent on the molecular spectral parameters listed above. These parameters are the lower state energies, line strength, pressure-broadening parameter, etc. The most comprehensive source used in the spectroscopic community is the HITRAN spectral database.

The HITRAN database was initiated in the 1970s and consists of a compilation of fundamental molecular spectral parameters required for calculation of line-by-line atmospheric absorption spectra. (Refs. 22-28) The information included in each record of the spectral database includes the line position, lower state energy, air and self broadening parameters at 296 K, the line strength at 296 K, and the pressure-broadening temperature exponent. Other information is also included that is not necessarily required, under normal conditions, for calculation of absorption spectra. These additional data include the upper and lower state rotational and vibration quantum numbers, references to the source of the data, and codes that specify the accuracy range of the various parameters.

There are over 2 million spectral lines from 39 species listed in the latest version of the HITRAN database (HITRAN-2008). A summary of the statistics of the HITRAN-2008 database is listed in Table 1. It is important to note that the lines included in the HITRAN database are those of primary concern to modeling and/or analysis of spectra associated with Earth’s atmosphere or other planetary atmospheres. Absorption lines with appreciable absorption levels at elevated temperatures, so called “hot lines,” are lacking in this atmospheric related database. As a result, another associated database(s) was compiled in 1995, HITEMP-1995. The data in this database are primarily that of the major combustion byproduct gases, H<sub>2</sub>O, CO<sub>2</sub>, and CO. This version of the high-temperature database is supposedly applicable to temperatures in excess of 1000 K. A newer and larger version of HITEMP was issued in 2010 (HITEMP 2010) (Ref. 29). This current update includes new H<sub>2</sub>O and CO<sub>2</sub> line listings based on the work of Barber et. al. and Tashkun et. al, respectively (Ref. 30-31). In addition, additional lines for NO, OH, and CO are included. These high-temperature parameters are based largely on quantum mechanical calculations and/or extrapolations of existing lower temperature HITRAN data to the predicted hot lines. Recently, the HITRAN-2008 and HITEMP-2010 databases were merged into one data set. The number of spectral lines, for each specie, in the merged dataset is given in Table 2. Note that in the merged data set only the number of H<sub>2</sub>O, CO<sub>2</sub>, CO, NO, and OH lines have changed with the line count for the remaining species the same as those of the HITRAN-2008 database.

Uncertainties associated with the various parameters listed in the HITRAN-2008 database are shown in Figs. 2 and 3 for H<sub>2</sub>O and CO<sub>2</sub>. As can be seen from examination of Figs. 2 and 3, much of the data possess uncertainties in the 5 to 20% range with some parameters having no known quoted uncertainties. Figures 4 and 5 show the quoted uncertainties of the merged HITRAN2008/HITEMP2010 spectral database. Although this merged database contains substantially more spectral line information of the primary combustion byproduct gases, there

remains a high degree of uncertainty in the spectral line parameters. The atmospheric modeling community is requesting parameters with subpercent range accuracy. However, the greatest need in the diagnostic community is verified low-uncertainty data of hot lines of combustion byproduct gases. Figures 4 and 5 show the quoted uncertainty statistics of the spectral parameters of H<sub>2</sub>O and CO<sub>2</sub> in the expanded merged HITRAN2008/HITEMP2010 spectral database. The inclusion of the calculated higher temperature lines shifts the overall uncertainty in the spectral parameters even higher with the majority of the spectral lines having uncertainties of 20% or higher. An additional requirement of the diagnostic community, not necessarily shared by the atmospheric modeling community, is the effects of spectral line broadening by other combustion byproducts. In atmospheric modeling applications the vast majority of pressure broadening is due to air. However, in aeropropulsion test and evaluation (T&E) diagnostic applications, combustion byproduct gases such as H<sub>2</sub>O and CO<sub>2</sub> can be present in the low tens of percent range. These gases also possess large electromagnetic moments that result in large pressure broadening parameters. This fact leads to a need for additional information on spectral line broadening by H<sub>2</sub>O and CO<sub>2</sub> not currently addressed in the HITRAN or HITEMP databases.

**Table 1. Statistics of HITRAN 2008 Spectral Database.**  
(The individual isotopologues for H<sub>2</sub>O and CO<sub>2</sub> are the only ones listed here).

HITRAN-2008			
Isotopologue	Number of Lines	Isotopologue	Number of Lines
<sup>1</sup> H <sub>2</sub> <sup>16</sup> O	37432	OH total	31976
<sup>1</sup> H <sub>2</sub> <sup>18</sup> O	9753	HF total	107
<sup>1</sup> H <sub>2</sub> <sup>17</sup> O	6992	HCl total	613
<sup>1</sup> H <sup>16</sup> O <sup>2</sup> H	13238	HBr total	1293
<sup>1</sup> H <sup>18</sup> O <sup>2</sup> H	1611	HI total	806
<sup>1</sup> H <sup>17</sup> O <sup>2</sup> H	175	ClO total	11501
H <sub>2</sub> O total	69201	OCS total	29242
<sup>12</sup> C <sup>16</sup> O <sub>2</sub>	128170	H <sub>2</sub> CO total	37050
<sup>13</sup> C <sup>16</sup> O <sub>2</sub>	49777	HOCl total	16276
<sup>16</sup> O <sup>12</sup> C <sup>18</sup> O	79958	N <sub>2</sub> total	120
<sup>16</sup> O <sup>12</sup> C <sup>17</sup> O	19264	HCN total	4253
<sup>16</sup> O <sup>13</sup> C <sup>18</sup> O	26737	CH <sub>3</sub> Cl total	196171
<sup>16</sup> O <sup>13</sup> C <sup>17</sup> O	2953	H <sub>2</sub> O <sub>2</sub> total	126983
<sup>12</sup> C <sup>18</sup> O	7118	C <sub>2</sub> H <sub>2</sub> total	11340
<sup>17</sup> O <sup>12</sup> C <sup>18</sup> O	821	C <sub>2</sub> H <sub>6</sub> total	22402
<sup>13</sup> C <sup>18</sup> O <sub>2</sub>	121	PH <sub>3</sub> total	20099
CO <sub>2</sub> total	314919	COF <sub>2</sub> total	70601
O <sub>3</sub> total	409686	H <sub>2</sub> S total	20788
N <sub>2</sub> O total	47843	HCOOH total	62684
CO total	4477	HO <sub>2</sub> total	38804
CH <sub>4</sub> total	290091	O total	2
O <sub>2</sub> total	6428	NO <sup>+</sup> total	1206
NO total	105079	HOBr total	4358
SO <sub>2</sub> total	58250	C <sub>2</sub> H <sub>4</sub> total	18378
NO <sub>2</sub> total	104223	CH <sub>3</sub> OH total	19897
NH <sub>3</sub> total	29084	CH <sub>3</sub> Br total	36911
HNO <sub>3</sub> total	487254	CH <sub>3</sub> CN total	3572
Total Number of Lines: 2,713,968			

**Table 2. Statistics of Merged HITRAN-2008 and HITEMP-2010 Spectral Database.**  
 (The individual isotopologues for H<sub>2</sub>O and CO<sub>2</sub> are the only ones listed here. Only the lines for H<sub>2</sub>O, CO<sub>2</sub>, CO, NO, and OH are updated in this dataset from those of HITRAN-2008).

<b>Merge HITRAN-2008 and HITEMP-2010</b>			
Isotopologue	Number of Lines	Isotopologue	Number of Lines
<sup>1</sup> H <sub>2</sub> <sup>16</sup> O	114,209,395	OH total	41,557
<sup>1</sup> H <sub>2</sub> <sup>18</sup> O	9,753	HF total	107
<sup>1</sup> H <sub>2</sub> <sup>17</sup> O	6,992	HCl total	613
<sup>1</sup> H <sup>16</sup> O <sup>2</sup> H	13,238	HBr total	1293
<sup>1</sup> H <sup>18</sup> O <sup>2</sup> H	1,611	HI total	806
<sup>1</sup> H <sup>17</sup> O <sup>2</sup> H	175	ClO total	11,501
H <sub>2</sub> O total	114,241,164	OCS total	29,242
<sup>12</sup> C <sup>16</sup> O <sub>2</sub>	5,881,107	H <sub>2</sub> CO total	37,050
<sup>13</sup> C <sup>16</sup> O <sub>2</sub>	1,732,473	HOCl total	16,276
<sup>16</sup> O <sup>12</sup> C <sup>18</sup> O	2,283,580	N <sub>2</sub> total	120
<sup>16</sup> O <sup>12</sup> C <sup>17</sup> O	604,891	HCN total	4,253
<sup>16</sup> O <sup>13</sup> C <sup>18</sup> O	522,203	CH <sub>3</sub> Cl total	196,171
<sup>16</sup> O <sup>13</sup> C <sup>17</sup> O	36,179	H <sub>2</sub> O <sub>2</sub> total	126,983
<sup>12</sup> C <sup>18</sup> O	132,746	C <sub>2</sub> H <sub>2</sub> total	11,340
<sup>17</sup> O <sup>12</sup> C <sup>18</sup> O	821	C <sub>2</sub> H <sub>6</sub> total	22,402
<sup>13</sup> C <sup>18</sup> O <sub>2</sub>	121	PH <sub>3</sub> total	20,099
CO <sub>2</sub> total	11,194,121	COF <sub>2</sub> total	70,601
O <sub>3</sub> total	409,686	H <sub>2</sub> S total	20,788
N <sub>2</sub> O total	47,843	HCOOH total	62,684
CO total	113,631	HO <sub>2</sub> total	38,804
CH <sub>4</sub> total	290,091	O total	2
O <sub>2</sub> total	6,428	NO <sup>+</sup> total	1,206
NO total	115,610	HOBr total	4,358
SO <sub>2</sub> total	58,250	C <sub>2</sub> H <sub>4</sub> total	18,378
NO <sub>2</sub> total	104,223	CH <sub>3</sub> OH total	19,897
NH <sub>3</sub> total	29,084	CH <sub>3</sub> Br total	36,911
HNO <sub>3</sub> total	487,254	CH <sub>3</sub> CN total	3,572
Total Number of Lines: 127,894,394			

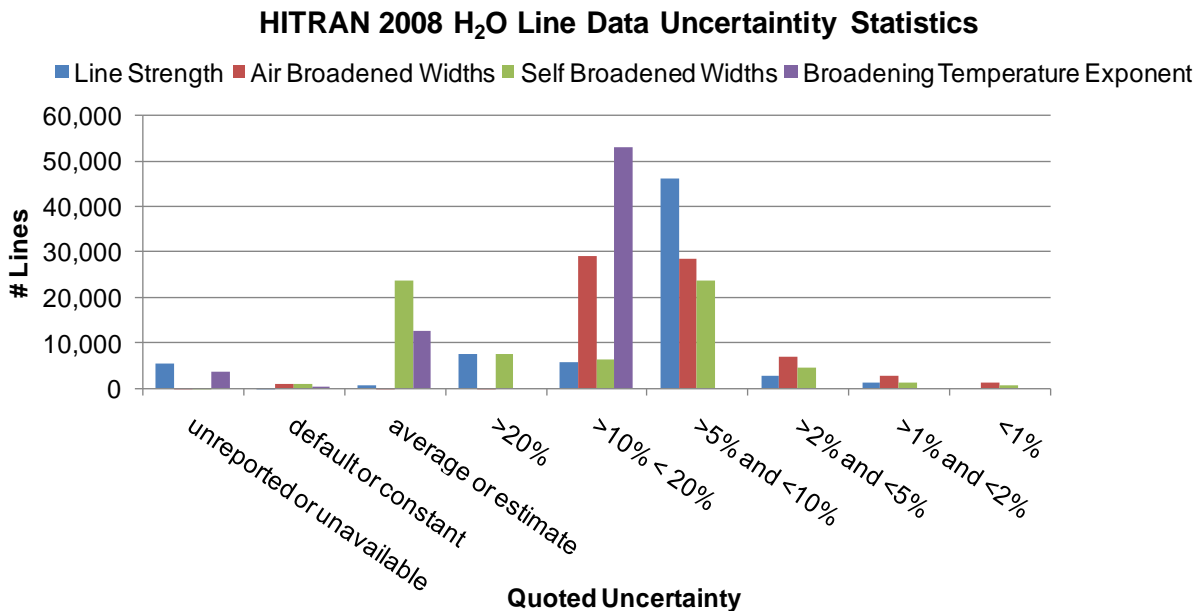


Figure 2. Uncertainties Associated with H<sub>2</sub>O Spectral Lines in the HITRAN 2008 Database

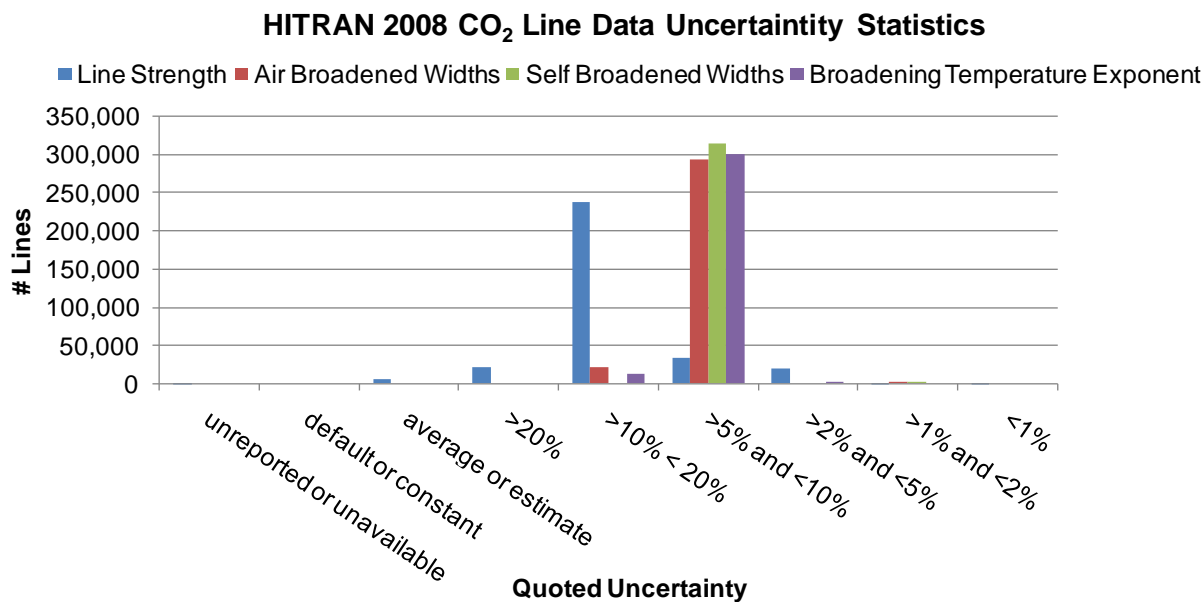


Figure 3. Uncertainties Associated with CO<sub>2</sub> Spectral Lines in the HITRAN 2008 Database

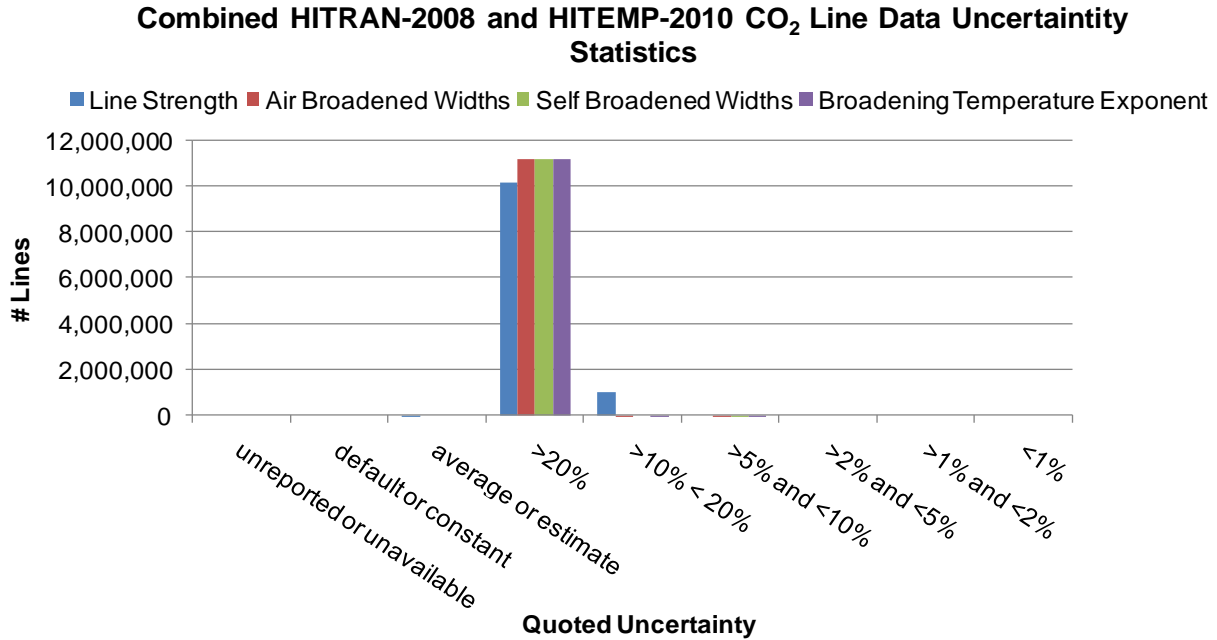


Figure 4. Uncertainties Associated with H<sub>2</sub>O Spectral Lines in the Merged HITRAN-2008 and HITEMP-2010 Database

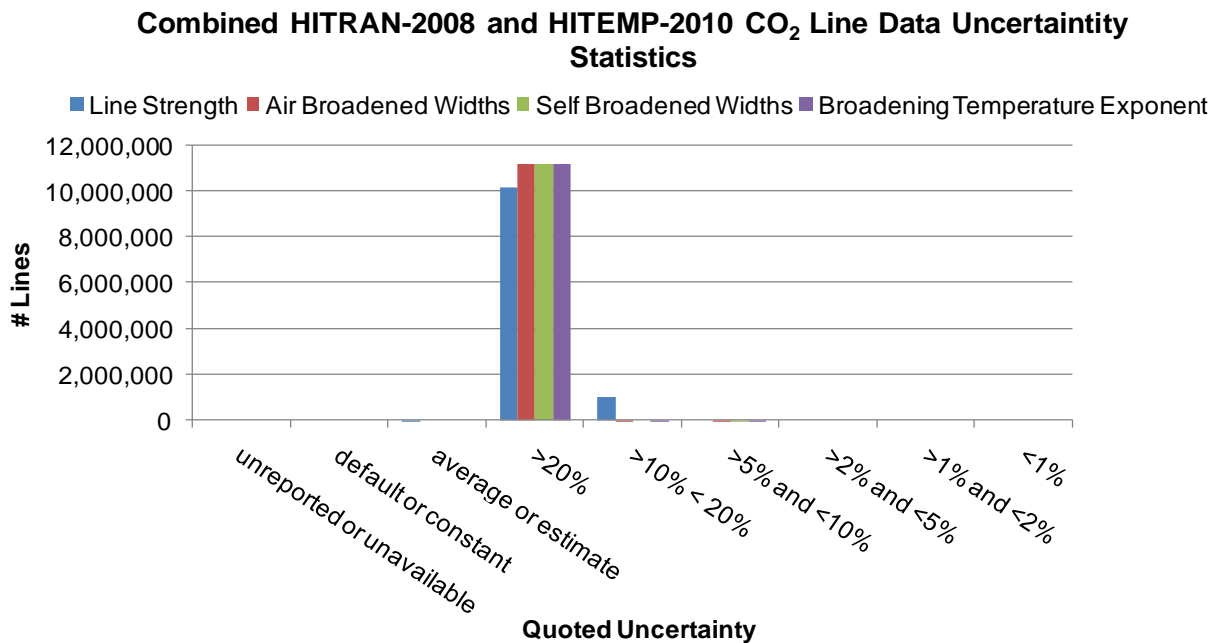


Figure 5. Uncertainties Associated with CO<sub>2</sub> Spectral Lines in the Merged HITRAN-2008 and HITEMP-2010 Database

## 4.0 DATA REDUCTION

There are many data reduction methodologies for retrieving gas properties such as temperature, pressure, velocity, etc., from spectral absorption measurements. The goal of this report is not to document all methodologies nor necessarily identify the best methodologies. The goal of this report is to better understand how best to minimize the uncertainties in the retrieved gas property parameters by identifying their relationship to uncertainties in the input parameters. Only then can one establish a systematic approach to improving the overall performance of optical absorption methods by directing further research and development to minimizing uncertainty in those key input parameters most affecting the uncertainty in the retrieved parameters. Seven different data reduction methodologies are presented.

The basic equations governing the absorption process have been described above. Before delving into uncertainty propagation, the various experimental methods for obtaining absorption measurement need to be addressed. Direct absorption is governed by Eq. (1) and is illustrated in Fig. 1. Here a laser is repeatedly tuned over the absorption feature by changing the wavelength output of the laser by controlling the diode injection current and/or temperature. This can be done very rapidly at rates of several kilohertz with the recorded scans co-added to increase the effective signal-to-noise ratio. Another method employs amplitude modulating the laser output by means of a mechanical chopper and performing synchronous detection using a lock-in amplifier. In this case the laser scan rate has to be much less than the chop rate, which is typically limited to approximately 20 kHz or lower. This requires the scan rate to be near or below the subkilohertz range.

The rapid scan capability of diode lasers makes possible a more sensitive absorption measurement technique known as wavelength modulated spectroscopy (WMS). By scanning the laser with a ramp source at some frequency “ $f$ ” while simultaneously adding a small dither modulation of a much higher frequency “ $f'$ ” the first and second derivative of the transmitted spectral intensity can be detected by selectively detecting the signal at frequency “ $f'$ ” and “ $2f'$ ,” respectively. A description of the technique in more detail is given in Appendix A. By detecting at a much higher frequency “ $2f'$ ” (typically on the order of +100s kHz), one now is operating in the electrical noise spectral region outside the  $1/f$ -noise region associated with the laser, detector/pre-amp, and other electronic components. As a result, a much improved signal-to-noise ratio can be achieved with an associated increase in sensitivity. The downside to utilizing this technique is the difficulty in retrieving quantifiable measurements. However, since this technique can provide the second derivative of the transmitted spectral intensity as a function of wave number at a high signal-to-noise, it is ideally suited to obtaining velocity by means of measuring the spectral Doppler shift. This technique is ideal for situations where there exist low absorbance levels and/or low direct absorption signal-to-noise ratios. Utilization of WMS for measurement of the Doppler shift requires a simple measurement of the spectral distance between shifted peaks in the spectrum. This measurement is ideally suited for WMS 2<sup>nd</sup> derivative spectra due to the high signal-to-noise ratio and the lack of definable absorption features in the direct absorption spectrum. It should be noted that the same laser and detector equipment can be employed to obtain both direct absorption and wavelength modulated spectra. Simply by modifying the laser modulation scheme and analysis of the detector signals, one can determine either direct absorption or wavelength modulated spectra.

### 4.1 BASELINE EXPERIMENTAL CONFIGURATION

A basic configuration for the modeled absorption experimental configuration had to be established for the ensuing calculations. The experimental configuration chosen was that

applied by Galyen and Plemmons in support of recent wind tunnel tests (Ref. 7). This particular application represents a good “real-world” application of TDL absorption spectroscopy and is shown schematically in Fig. 6. This experimental configuration was utilized by Galyen and Plemmons to obtain mass flow or mass flux from laser absorption measurements. The measured parameters were the O<sub>2</sub> number density, from O<sub>2</sub> direct absorption measurements, and velocity from the relative Doppler shift from upstream and downstream measurements. Velocity was obtained from the relative Doppler shift from the second derivative spectrum obtained utilizing wavelength modulated spectroscopy. Two separate absorption beams were utilized with one propagating upstream at a 45-deg angle with respect to the flow velocity, providing a red-shifted spectral line, and another directed downstream at a 45-deg angle with respect to the flow velocity, providing a blue-shifted spectral line. By examining the shift in the peaks, the Doppler shift, actually twice the Doppler shift, can be determined and a path average velocity can be retrieved by means of Eq. (18). Number density of oxygen was determined by the absorption from the 746.28-nm (13084.2-cm<sup>-1</sup>) absorption feature of oxygen. The temperature utilized in these specific measurements was provided by an independent method. The details of the measurements are discussed in Ref. 7.

This experimental configuration is employed in all the modeling presented in this report. The velocity is consistently assumed to be measured by means of the technique described above employing WMS. However, seven different representative data analysis methods for obtaining absorbing specie number density, total number density, and/or temperature are examined. In each case the number density is combined with the velocity to determine the mass flux. Throughout the remainder of the discussions the mass flux is based on the velocity and total density as determined by the absorbing specie number density. Utilizing this method for determining the mass flux necessitates a prior knowledge of the absorbing specie mole fraction. For the case of Galyen and Plemmons’ measurements, this was simply the mole fraction of O<sub>2</sub> in air. However, for combustion streams one would need an independent measurement of total number density or mole fraction. It is assumed in the following work that we have a prior knowledge of the known mole fraction in the determination of the mass flux. An alternative, not considered here, is using the simultaneous measurement of absorbing specie number density and total number density together with the velocity to infer mass flux. However, as will be seen later this would produce a very large uncertainty in mass flux due to our inability to retrieve total number density with any reasonable bounds on its uncertainty in a combustion exhaust environment typical of high-speed aeropropulsion system testing. The retrieved parameters from the various methods discussed below are velocity, mass flux, and absorbing specie number density, and depending on the specific technique, the total number density and temperature are also retrieved. Details of each individual technique are provided below. Each technique is assigned an abbreviated descriptor, in parenthesis, used to designate the various data in the plots and tables.

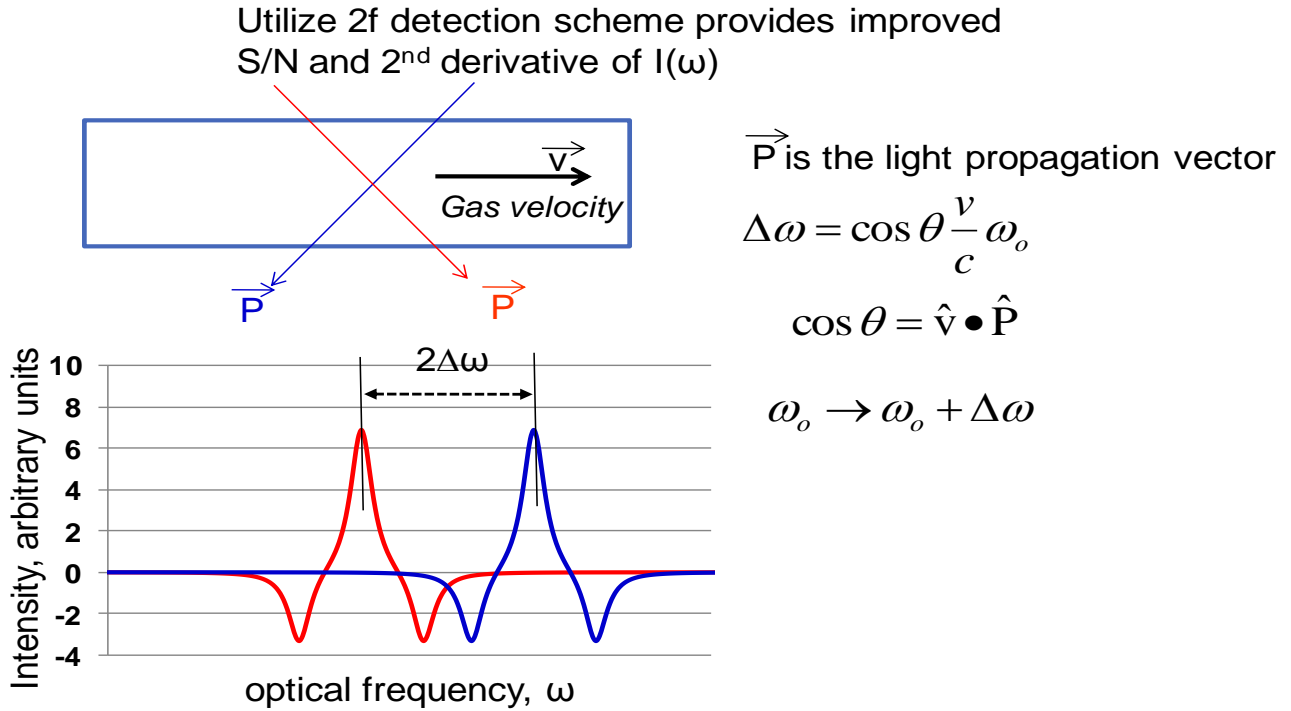


**Figure 6. Schematic of Hypothetical Measurement Geometry Used in the Baseline Spectral Calculations**

#### 4.2 DATA REDUCTION METHODOLOGIES

Seven different data reduction methods are addressed in the following uncertainty analysis. Two of the methods utilize an integrated spectral absorbance approach with the remaining five employing a nonlinear least square curve fitting approach. Each is described in more detail below.

##### 4.2.1 Integrated Linear Absorbance (LAINT)

Provided that the absorption feature is weak, i.e., the absorbance is small or optically thin, then the transmitted intensity from Eq. (1) can be approximated as

$$I(\omega) \approx I^o(\omega)(1 - k(\omega)) \tag{20}$$

Thus the spectral transmittance becomes

$$\tau(\omega) \equiv \frac{I(\omega)}{I^o(\omega)} \approx (1 - k(\omega)) \tag{21}$$

Under this weak absorption or optically thin assumption, the spectral transmittance is linearly proportional to the spectral absorbance. Rearranging and integrating the above equation over all wave numbers gives

$$\int \left[ 1 - \frac{I(\omega)}{I^o(\omega)} \right] d\omega = N_\alpha LS_\alpha^o(T) \tag{22}$$

This can be solved for absorbing specie number density,  $N_a$ , provided an independently measured value of the temperature is available. The line strength at temperature  $T$  is determined from the line strength at a reference temperature using Eq. (8). Note this technique is not directly dependent of the spectral line shape function or pressure-broadening parameters. However, in actuality the integration does not extend over all optical frequencies due to the limited tuning range of the laser diodes. This can then present some line width dependency on the retrievals if the line width is sufficiently large to produce nontrivial absorption in the line wings. A wing correction term is utilized to correct for the limited integration range. This correction term is discussed in Appendix B. The wing correction is applied to this data reduction methodology and to the NLINT methodology discussed below.

Note that the quantity in the integral is determined from the measured unattenuated and attenuated spectral data. The line strength is obtained from the HITRAN database, or other listing, and  $l$ , the path length, is assumed to be known.

#### 4.2.2 Integrated Nonlinear Absorbance (NLINT)

Eliminating the optically thin assumption, i.e., small absorbance values, the spectral absorbance can be determined from the attenuated and unattenuated spectra using

$$N_a l S_a^o(T) = \int k(\omega) d\omega = - \int \ln \left[ \frac{I(\omega)}{I^o(\omega)} \right] d\omega \quad (23)$$

This method also provides the absorbing specie number density, like the LAINT method, but is also applicable when the absorbance levels are sufficiently high that the linear approximation is no longer satisfied. Again, one is required to have an independently determined value of temperature.

#### 4.2.3 Nonlinear Spectral Transmittance Curve Fit for Absorbing Specie Number Density with Measured Background (NLFIT1)

The remaining techniques discussed utilize nonlinear fitting to obtain the retrieved parameters. This particular method assumes one has a measured attenuated spectral intensity,  $I(\omega)$ , and a measurement or independently determined background unattenuated spectral intensity,  $I^o(\omega)$ . The spectral transmittance determined from these measurements is a function of many input parameters including the absorbing specie number density. The parameters listed in the brackets,  $\{ \}$ , below, and in the following nonlinear fit methods, are those parameters used in the nonlinear curve fitting. The optical frequency,  $\omega$ , is an independent variable, and all other variables are assigned values which are perturbed in the Monte Carlo analysis discussed later.

$$\tau(\omega; \{N_a\}, l, N, S_a^o, \gamma_L^o, \eta, E_{low}, T, \omega_o, \nu) = \tau_m(\omega) = \frac{I_m(\omega)}{I_m^o(\omega)} \quad (24)$$

The subscript  $m$  denotes this is either a measured spectral quantity or derived from the measured spectra. All other parameters are assumed to be provided by other means. Utilizing the equations governing the absorption process in Eqs. (1-19), a spectral transmittance is nonlinear-fitted to the measured spectral transmittance data by iteratively adjusting the absorbing specie number density. Unlike the previous two techniques, this technique does not utilize integration over the spectral line and thus does not possess the indirect dependency on the line width that is inherent with a line integration technique when one cannot scan the entire

absorption feature. However, this technique will possess an uncertainty dependence on the broadening parameters since they have to be utilized in the model of spectral transmittance used as the fit function.

#### 4.2.4 Nonlinear Spectral Transmittance Curve Fit for Absorbing Specie Number Density with Floating Background (NLFIT2)

This technique is very similar to the NLFIT1 technique. The difference is that the background or unattenuated spectral intensity is not given and is treated as another fit parameter in the nonlinear fitting process. Therefore, this fitting process involves two fit parameters – the absorbing specie number density and a constant background. The mathematical equivalent of Eq. (24) in this case would be given by

$$\tau(\omega; \{N_\alpha, I^o(\omega)\}, l, N, S_\alpha^o, \gamma_L^o, \eta, E_{low}, T, \omega_o, \nu) = \tau_m(\omega) = \frac{I_m(\omega)}{I^o(\omega)} \quad (25)$$

It should be noted here that in all the simulations performed in this work the background is assumed to be constant (i.e.  $I^o(\omega) = I^o$ ), aside for applied noise. This is not a realistic assumption, but it does not impose a severe restriction on the results, which is to obtain trends of the dependence of the uncertainties of the retrieved parameters on the uncertainties of the input parameters or measurements. For our purpose the retrieved background intensity is an ignored result, but this result must be included in the nonlinear fitting process. This can be, as it is in many cases, generalized to situations where the background is modeled by a low degree polynomial with the coefficients in the polynomial being additional fit parameters.

#### 4.2.5 Nonlinear Spectral Transmittance Curve Fit for Absorbing Specie Number Density and Temperature with Floating Background (NLFIT3)

NLFIT3 is similar to NLFIT2 but employs the additional fit parameter of temperature. This technique is employed often for nonintrusive temperature measurements. The temperature dependence is not straightforward since the line strength and all the broadening parameters have a temperature dependency. Unfortunately, the inclusion of additional fitting parameters typically comes at the expense of numerical stability and requires relatively good signal-to-noise ratio spectral data. This technique is more applicable to situations where one has two or more spectral lines within the spectral scan of the laser. If two or more of the spectral lines possess different lower state energies, one can obtain a strong temperature dependence in the relative strength of the absorption of the two spectral lines owing to its dependency on the Boltzmann distribution. This has been exploited by many researchers and is described in Ref. 10. The equation describing this method is given by

$$\tau(\omega; \{N_\alpha, T, I^o(\omega)\}, l, N, S_\alpha^o, \gamma_L^o, \eta, E_{low}, \omega_o, \nu) = \tau_m(\omega) = \frac{I_m(\omega)}{I^o(\omega)} \quad (26)$$

#### 4.2.6 Nonlinear Spectral Transmittance Curve Fit for Absorbing Specie Number Density and Total Number Density with Floating Background (NLFIT4)

NLFIT4 is similar to NLFIT3. NLFIT4 assumes the temperature is determined by another means and the total number density is an additional fit parameter. This method can be employed to determine pressure from the total number density and as will be seen in later discussions is not very precise at lower pressures or particularly where spectral line shape tends more to a Doppler profile than to a Lorentz or Voigt profile. In these situations the

strength and shape of the spectral absorption has only a weak dependency on total number density, or pressure. Also, at elevated temperatures the pressure-broadening parameters decrease (Eq. [14]) resulting in loss sensitivity to total number density. The equation used to summarize this method is given by

$$\tau(\omega; \{N_{\alpha}, N, I^o(\omega)\}, l, S_{\alpha}^o, \gamma_L^o, \eta, E_{low}, T, \omega_o, \nu) = \tau_m(\omega) = \frac{I_m(\omega)}{I^o(\omega)} \quad (27)$$

#### 4.2.7 Nonlinear Spectral Transmittance Curve Fit for Absorbing Specie Number Density, Total Number Density, and Temperature with Floating Background (NLFIT5)

This technique is an extension of the two previously discussed techniques. This technique requires nonlinear fitting of four parameters; absorbing specie number density, temperature, total number density, and background level. As a result of the additional parameters this method is generally more numerically sensitive to data quality. For this reason it is not typically used, but it is included here for completeness. Usually one has an independent measure of temperature and/or pressure. The governing equation is summarized as

$$\tau(\omega; \{N_{\alpha}, N, T, I^o(\omega)\}, l, S_{\alpha}^o, \gamma_L^o, \eta, E_{low}, \omega_o, \nu) = \tau_m(\omega) = \frac{I_m(\omega)}{I^o(\omega)} \quad (28)$$

### 5.0 ERROR PROPAGATION BY MEANS OF MONTE CARLO SIMULATION

The method of assessing propagated uncertainty employed use of Monte Carlo simulations. The method is described in some detail in the international Guide to the Expression of Uncertainty in Measurements (GUM) prepared by the Joint Committee for Guides in Metrology Bureau International des Poids et Mesures (Refs. 32 and 33). The first step was to generate a baseline transmittance spectrum at known conditions. A Gaussian distribution of random numbers was then employed to add noise to the data or to create a Gaussian-distributed variation in one of the HITRAN or other input parameters utilized in the data analysis. Only one parameter was varied at any given time. This provided a means of determining what specific input parameter uncertainty was most influential in the uncertainty of the output parameters for various data reduction methods. It should be noted that an easy modification to the technique could be incorporated to simultaneously add combinations of specified noise and/or uncertainty of various input parameters to ascertain retrieved parameter uncertainties due to uncertainty in multiple input parameters. The last step in each cycle was to reduce the simulated data, or noise enhanced simulated data, utilizing the perturbed data input parameters. This process constitutes one cycle of the process.

A number of cycles were repeated for each specified parameter and magnitude of the parameter's deviation from the mean or given value. Typically 1000 cycles were performed for each parameter and magnitude in order to maintain a good statistical sample. The computer code input parameters consisted of the mean of the parameter in question and the standard deviation,  $1\sigma$ , about the mean for the probability distribution. The resultant parameters obtained from the data analysis were then averaged and standard deviations calculated for each combination of input parameter and deviation magnitude of the input parameter. Then the standard deviation of the output parameter, as a percent of the mean value, was plotted vs. the standard deviation of the input parameter as a percent of its given value. It should be noted due to the nonlinear nature of the model, the mean of the distribution of the output parameter is not the value of the model evaluated with the mean of the input parameter. This is due to the output

distribution not necessarily being Gaussian. Some of the nonlinear fit data reduction methods would not converge for certain combinations of input parameters and simulated data. These usually occurred at large deviations from the baseline value of the input parameter and could potentially skew the results. A risk mitigation strategy was incorporated where these nonconvergent results were eliminated from the statistics. However, the program flagged any event when the number of random cycles produced less than some prescribed percent of valid values, here 90%. All data and parameter combinations presented in this work meet these criteria. Figure 7 schematically illustrates the operation of the Monte Carlo simulation.

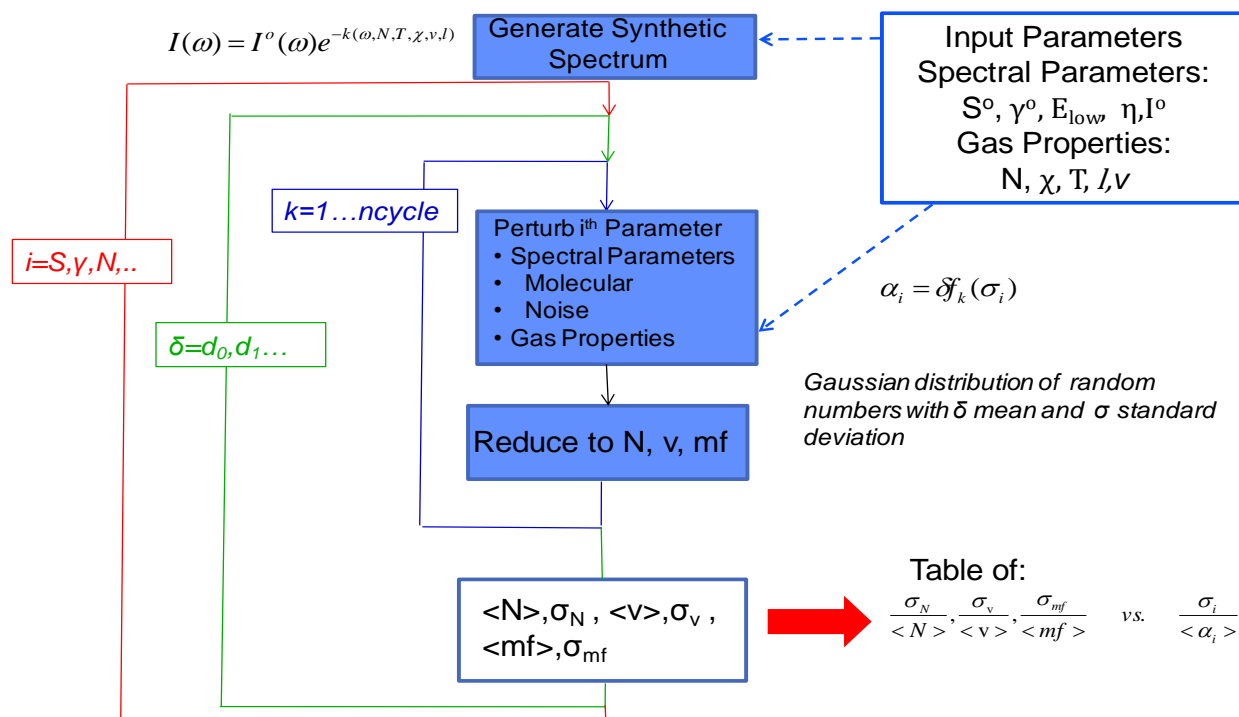


**Figure 7. Schematic of Monte Carlo Simulation Methodology**

This process was performed utilizing all seven data reduction methods listed above in Section 4. Input parameters used in the Monte Carlo analysis performed here included line strength, air or foreign gas broadening parameter, self-gas broadening parameter, broadening parameter temperature correction exponent, lower molecular energy state energy level, total number density, temperature, path length, velocity, mean background or transmitted intensity baseline, intensity or background level, and second-derivative intensity. As a result of the sheer volume of possibilities (i.e., 7 data reduction methods, 12 parameters, 1,000 cycles, 21 variations in magnitude) the Monte Carlo (MC) method employed in this survey study was computationally intensive. As an example, it required approximately 2 days on a 3.2 GHz Windows-XP-based PC for one particularly slow converging case employing 12 spectral lines. Many of the possible input/output parameter combinations are not addressed in this work as they are relatively straightforward or yield no unintuitive insight, such as the effect of optical path length. The use of the MC technique for obtaining uncertainties in retrieved parameters based on specific input parameters, each with specific uncertainties, would drastically reduce the computational resources required. It should be noted that the MC algorithm employed was not written to take advantage of multiple processors. Multithreading the computer code and careful attention to speed optimization could result in a substantial reduction in execution times.

## 6.0 TEST CASES

Four general test cases are presented to cover a range of conditions and spectral regions. These test conditions are listed in Table 3. These specific cases were chosen based on previous applications and the diverse range of gas and spectral properties. Test Case 1 is representative of measurements conducted by Galyen and Plemmons in an experimental wind tunnel and is representative of a relatively high-pressure (0.5 atm), slow (150 m/sec), and weak absorption scenario. Test Cases 2 and 3 were included to examine the effects of increasing temperature and represent a low-pressure and extremely low-absorbance scenario. In addition, Test Cases 2 and 3 consist of multiple absorption lines and have previously been employed by O'Bryne for measurements of a postcombustion flow at atmospheric pressures (Ref. 34). The pressure employed in the cases examined here are reduced from that of O'Bryne to better represent the exhaust of a high-speed propulsion system operating at altitude conditions. The velocity for Test Cases 2 through 4 was increased to 1,500 m/sec to be more representative of a high speed flow environment. Test Case 4 is included to represent a low-pressure, high-temperature, high-speed, strong absorption case that one may anticipate when employing quantum cascade lasers to measure combustion efficiency, via CO concentration, in a high Mach number, high-altitude environment. The particular transitions implemented in Test Case 4 were originally investigated by Lowry and Fisher for application to high temperature environments (Ref. 10). The particular transitions, by test case, are listed in Table 4 along with their associated molecular spectral parameters. An optical path length of 40 cm was chosen for all four test cases.

**Table 3. List of Various Test Conditions**

	T, Kelvin	P, Atm.	V, (m/sec)	Mole Fraction		
				H <sub>2</sub> O	O <sub>2</sub>	CO
Case 1	300	0.5	150		.2094	
Case 2	1,000	0.01	1,500	.1		
Case 3	2,000	0.01	1,500	.1		
Case 4	2,000	0.01	1,500			0.01

Figure 8 is a plot of the O<sub>2</sub> transmission spectrum for Test Case 1 at various temperatures. Notice the decrease in overall absorption with increasing temperature. This is primarily due to the decreasing number density of O<sub>2</sub> with increasing temperature while holding the pressure constant. The spectrum shown is the blue-shifted spectrum one would expect at a velocity of 150 m/sec. At the Test Case 1 conditions the minimum transmittance is approximately 0.9915, which represents a maximum absorbance (Note: all absorbances in this work are base  $e$ ) of approximately  $8.5 \times 10^{-3}$ .

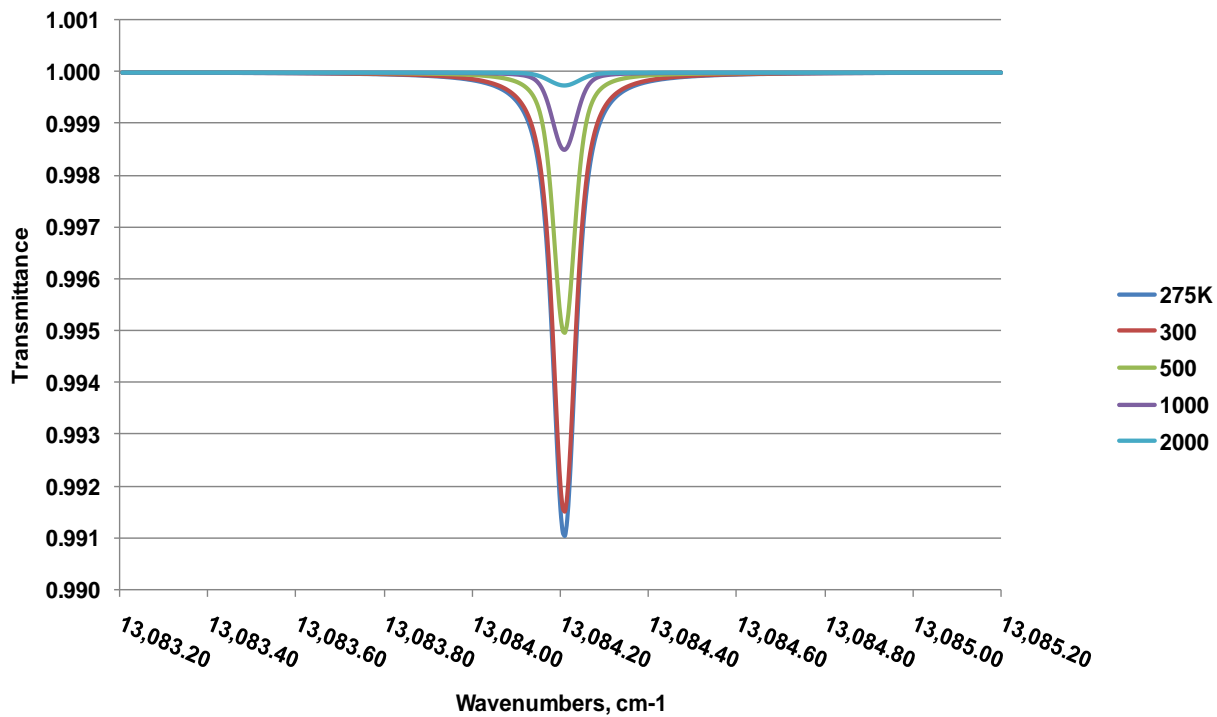


**Figure 8. Spectral Transmittance of the Blue-Shifted 764.28-nm ( $13,084.203\text{-cm}^{-1}$ )  $\text{O}_2$  Transition Utilized in the Work of Plemmons and Galyen and Employed in Case 1 of This Work. (Conditions: pressure = 0.5 atm, temperature = 300 K, path = 40 cm,  $\text{O}_2$  mole fraction = .20946)**

**Table 4. Molecular Spectral Parameters from HITRAN 2008 Used in the Monte Carlo Simulations. Case 1 parameters are for the 764.28 nm O<sub>2</sub> spectral line used by Plemmons and Galyen. (Ref. 7). Case 2 and 3 parameters are those of the H<sub>2</sub>O main isotopologue within the spectral range used by O'Bryne (Ref. 31). Case 4 are those parameters from the HITRAN 2008 database that match the CO spectral lines used in Ref. 10.**

	Specie	$\omega_0$ (cm <sup>-1</sup> )	$S^0$ (cm <sup>-1</sup> /molecules cm <sup>-2</sup> )	$E_{\text{low}}$ (cm <sup>-1</sup> )	$\gamma^0(T_0=296\text{K})$ air (cm <sup>-1</sup> /atm)	$\gamma^0(T_0=296\text{K})$ self (cm <sup>-1</sup> /atm)	$\eta$		
Test Case 1	O <sub>2</sub>	13084.203460	7.435x10 <sup>-24</sup>	190.7748	.0478	.048	.72		
		10542.920570	2.990x10 <sup>-23</sup>	79.49640	.1050	.464	.75		
		10543.091960	2.013x10 <sup>-26</sup>	1045.05790	.0649	.423	.62		
		10543.331830	2.005x10 <sup>-25</sup>	1524.8479	.0274	.260	-.29		
		10543.782370	5.477x10 <sup>-22</sup>	136.76170	.1055	.466	.73		
		10544.217480	5.820x10 <sup>-25</sup>	23.79440	.1051	.507	.77		
		10544.447840	8.000x10 <sup>-25</sup>	503.96810	.0830	.590	.66		
		10545.118900	1.024x10 <sup>-23</sup>	888.63260	.0635	.334	.29		
		10545.243660	3.067x10 <sup>-23</sup>	888.59870	.0577	.423	.29		
		10545.350380	1.468x10 <sup>-22</sup>	142.27850	.0928	.466	.75		
Test Case 2, 3	H <sub>2</sub> O	10545.643100	1.294x10 <sup>-23</sup>	134.90160	.1103	.545	.73		
		10545.736920	2.579x10 <sup>-25</sup>	1122.70850	.0877	.328	.68		
		10545.907690	2.929x10 <sup>-24</sup>	315.77950	.4470	.7795	.78		
		2135.313200	2.288x10 <sup>-23</sup>	2181.36920	.0650	.073	.74		
		2135.546200	1.745x10 <sup>-19</sup>	11.53500	.0748	.082	.75		
		Test Case 4	CO						

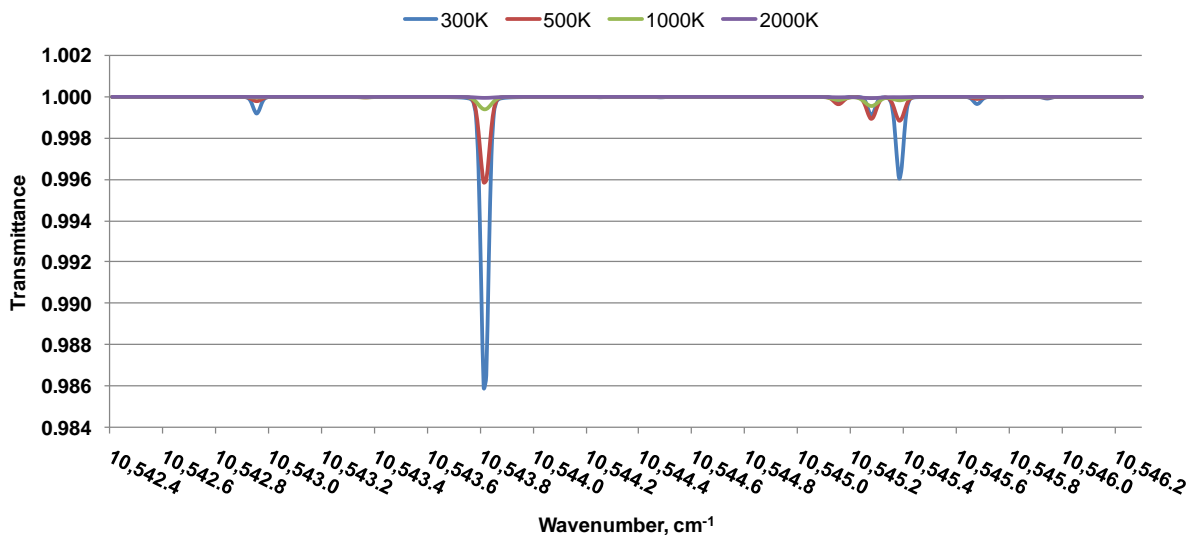


**Figure 9. Spectral Transmittance of the Blue-Shifted H<sub>2</sub>O Absorption Features Utilized in the Work of O’Bryne and the Test Cases 2 and 3 Calculations of this Work. (Conditions: pressure = 0.01 atmosphere, path length = 40 cm, 10% H<sub>2</sub>O).**

The H<sub>2</sub>O absorption features utilized by O’Bryne are shown in Fig. 9. Note, as with the O<sub>2</sub> single absorption line (Case 1), there is a substantial change in overall absorption due to the increasing temperature. As before, this overall change is due to the ideal gas law forcing the number density to decrease with increasing temperature while holding the pressure constant. However, what is key here is the change in the relative magnitude of the absorption between the various features with increasing temperature. This change in relative absorption in the various spectral features is driven by the Boltzmann distribution of number density population in the lower states of the transition and the temperature dependence of the pressure-broadened half-widths. It is this relative change of the various absorption features that is exploited in retrieving temperature from spectral absorption or transmittance spectra.

Absorption cross sections of various infrared active molecules of combustion byproduct gases increase in the mid-IR regions (2-5 $\mu$  or 5000-2000 $\text{cm}^{-1}$ ) over their counterpart in the near-IR (1-2 $\mu$  or 10,000-5000 $\text{cm}^{-1}$ ). The use of these longer wavelengths, hence increased cross sections, is advantageous in applications where the optical path length is limited. As the use of new solid-state lasers, such as the quantum cascade laser, become more prevalent, the mid-IR spectral region will undoubtedly be increasingly employed in gas diagnostics applications where the optical path length may be limited. Therefore, a mid-infrared Test Case 4 was chosen to be representative of potential future mid-infrared diagnostics applications. Test Case 4 utilizes two CO spectral lines selected by Lowry and Fisher for high-temperature diagnostics applications. These lines were specifically chosen as a tradeoff between appreciable absorption, temperature sensitivity, close spectral proximity, and lack of spectral interference. The spectral transmittances for a case of a path length of 40 cm, 0.01 atmosphere pressure, and 1% CO was chosen as representing a nominal high-speed engine exhaust. These conditions are denoted as Case 4 in Table 3. The spectra of CO at various temperatures are shown in Fig. 10, where the relative change in absorption between the two spectral features is more pronounced than that of the Test Case 2 and 3 H<sub>2</sub>O absorption features.

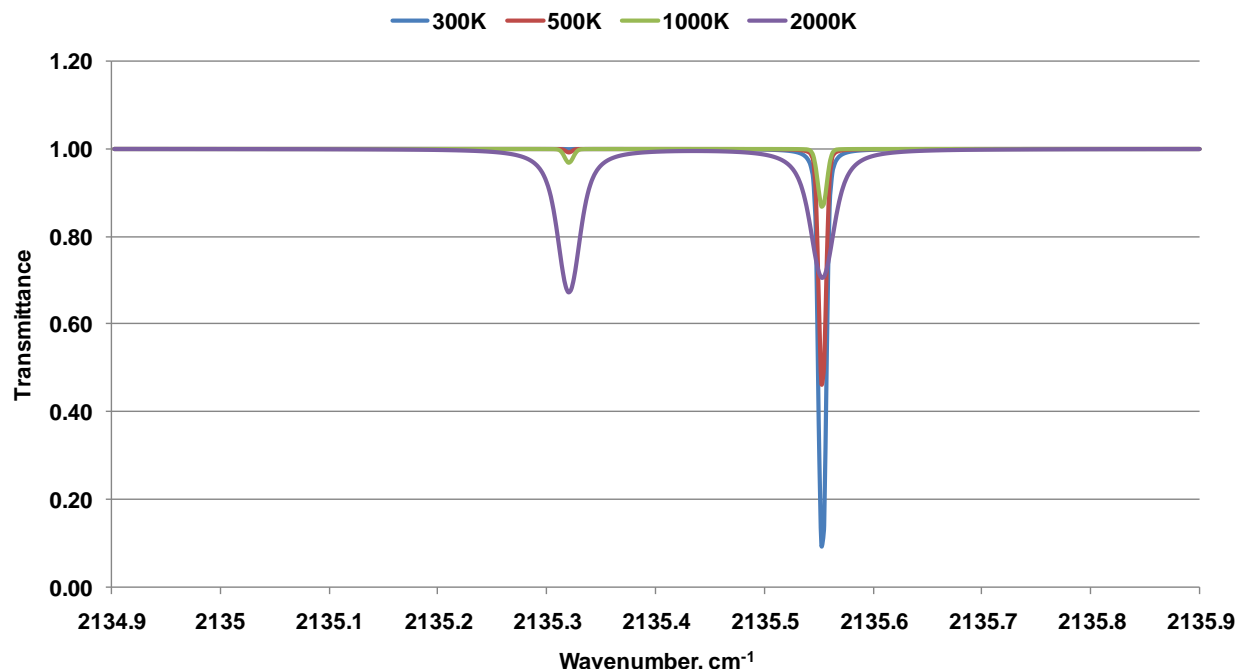


**Figure. 10. Spectral Transmittance of the Blue-Shifted CO Absorption Features Utilized in the Work of Lowry and Fisher and the Case 4 Calculations of this Work. (Conditions: pressure = 0.01 atm, path length = 40 cm, 1% CO).**

## 7.0 RESULTS

Each case in Table 1 was analyzed utilizing the Monte Carlo method. In each case seven different data reduction methods were employed in determining the retrieved parameters of interest. All Monte Carlo simulations were performed using 1,000 samples. The amount of deviation in each input parameter was varied from zero to some specified maximum in 21 steps. In some cases, particularly for H<sub>2</sub>O at the highest temperatures, the transmittance approached unity. In these cases the methods based on nonlinear fitting would not converge. In these particular cases those data were dropped from the sample pool. Nowhere did the number of dropped samples constitute more than 10% of the total number of samples.

The number of spectral data points considered was 400 absorption spectral data points and 4,000 second-derivative absorption data points. These numbers were chosen based on the data of Galyen and Plemmons. The number of second-derivative absorption data points has to be sufficiently large to ensure that the spectral distance between the blue- and red-shifted spectra peaks can be accurately quantified. The spectral scan range for each case was matched closely to those achievable with current technology diode laser scanning systems or previous experiential values obtained from the literature.

Figures 11 through 14 illustrate an example of the data reduction curve fitting applied to synthetic spectra with noise. Figures 11 through 14 each represent Test Cases 1 through 4, respectively. The curve-fitting parameters in these cases were those associated with the NLFIT5 method – absorbing specie number density, total number density, temperature, and a floating background.

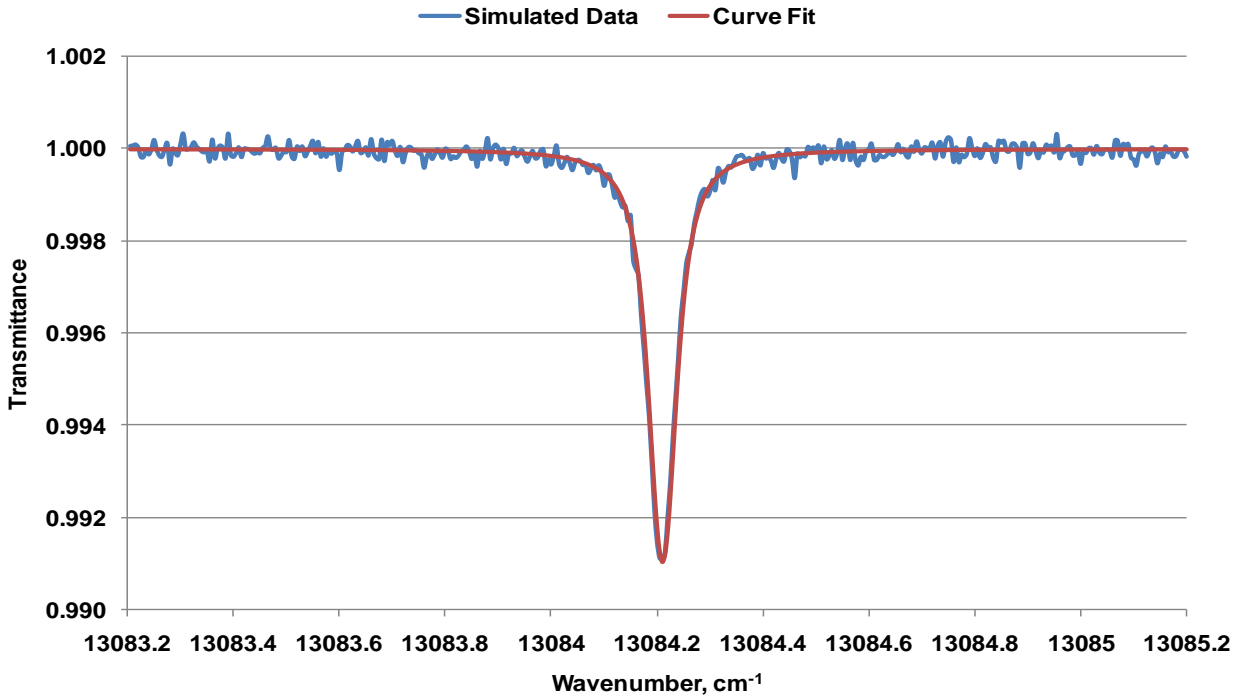


Figure 11. Simulated Case 1 Data with Addition of Noise and Resultant Curve Fit. Simulated signal-to-noise ratio was 10,000:1. Conditions: 300 K, 40 cm path length, 0.5 atmosphere pressure.

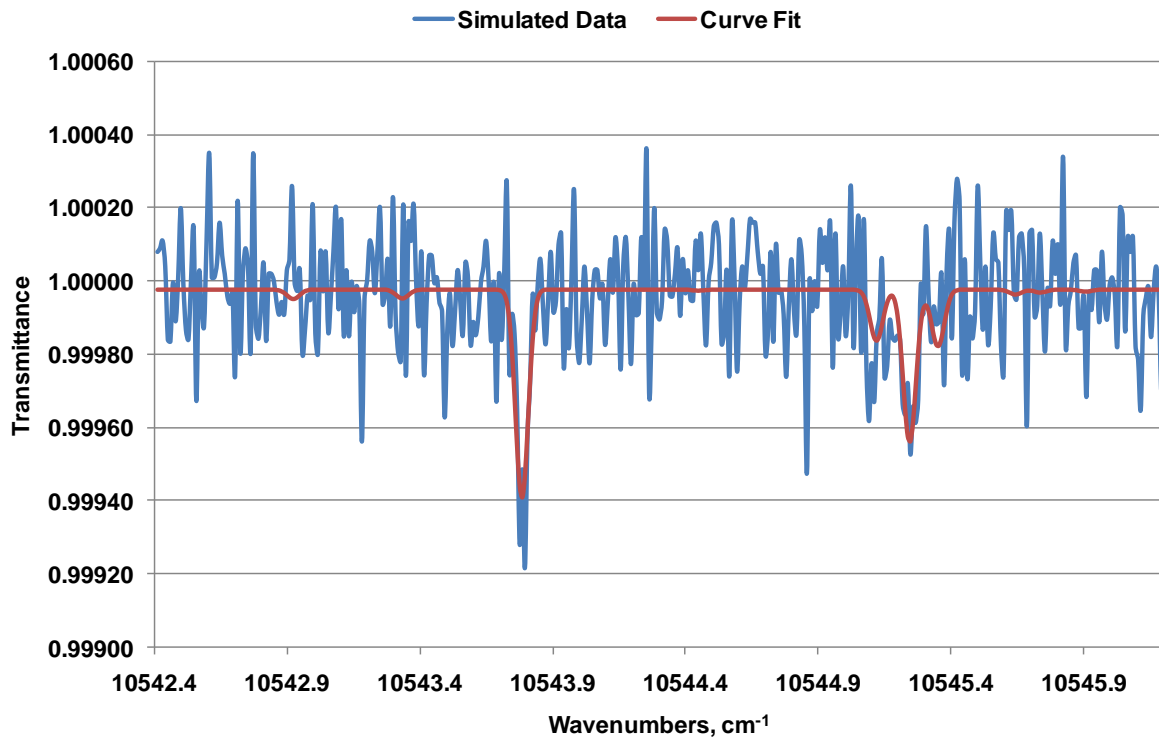


Figure 12. Simulated Data for Case 2 and Associated Curve Fit. Simulated signal-to-noise is 10,000:1. Conditions: 1,000 K, 40 cm path length, 0.01 atmosphere pressure, 10% H<sub>2</sub>O.

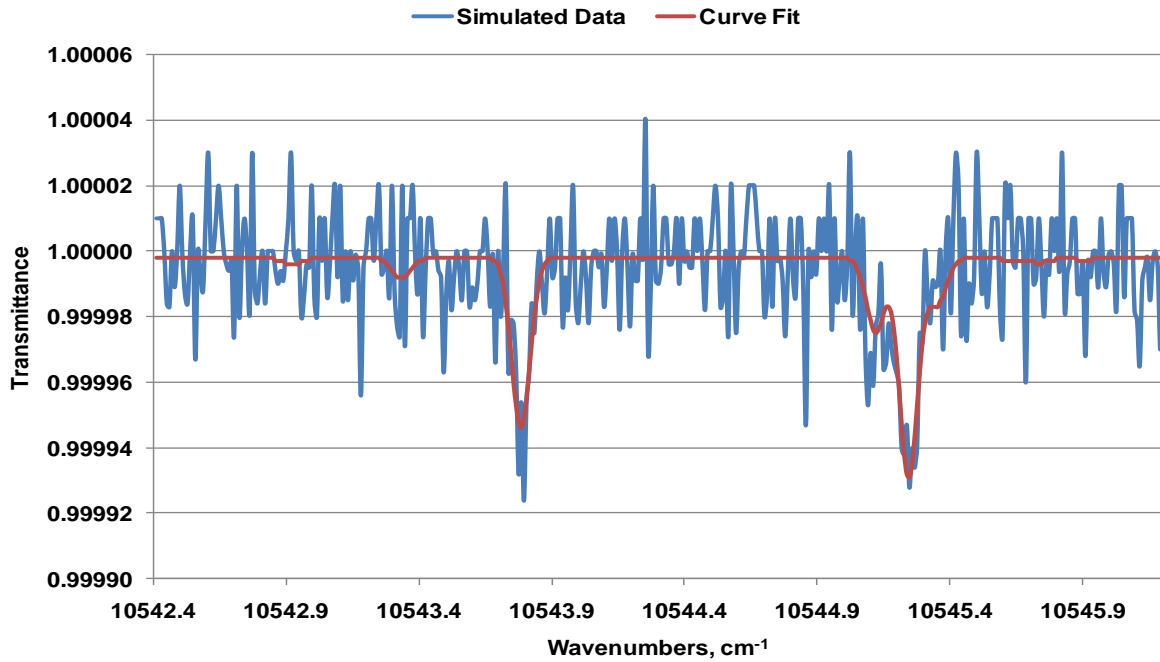


Figure 13. Simulated Data for Case 3 and Associated Curve Fit. Simulated signal-to-noise is 10,000:1. Conditions: 2,000 K, 40 cm path length, 0.01 atmosphere pressure, 10% H<sub>2</sub>O.

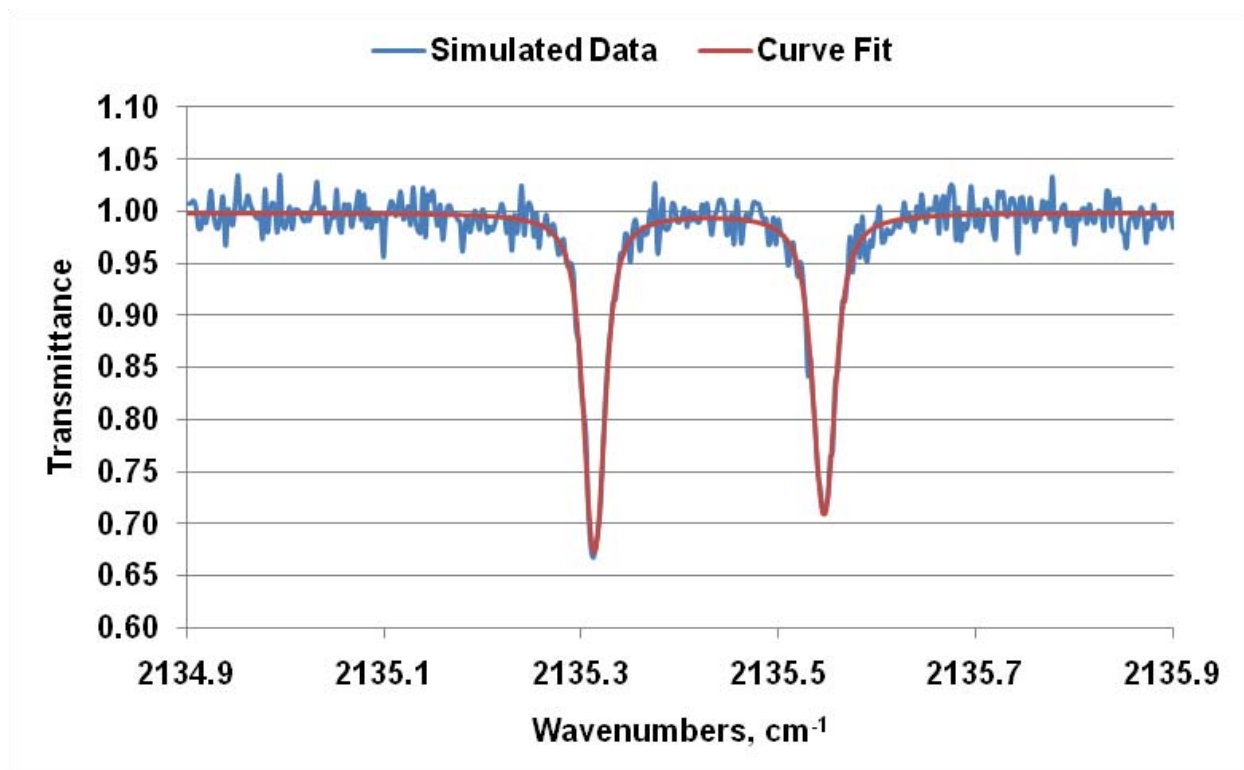
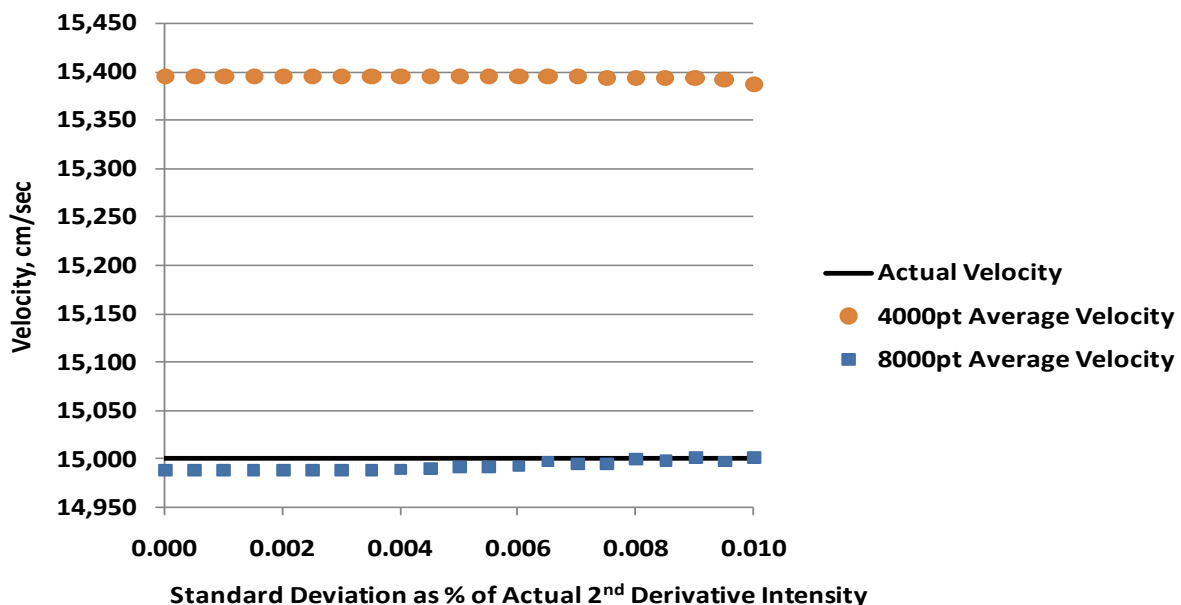


Figure 14. Simulated Data for Case 4 and Associated Curve Fit. Simulated signal-to-noise is 100:1. Conditions: 2,000 K, 40 cm path length, 0.01 atmosphere pressure, 1% CO.

The number of possible input and output parameter uncertainty combinations is large as each retrieved parameter ( $T$ ,  $N_{as}$ ,  $N_{total}$ ,  $v$ ,  $mf$ ) can be plotted vs. uncertainty of all input parameters. Many of these are uncorrelated in that the retrieved parameter has no appreciable dependence on a specific set of input parameters. In the foregoing discussions only those characteristics deemed noteworthy will be discussed. However, one of the powerful characteristics of the MC analysis technique is its ability to provide a wide array of information on cross dependencies of uncertainties of retrieved and input parameters.

## 7.1 CASE 1: O<sub>2</sub>

Monte Carlo analysis results of the O<sub>2</sub> transition at 747.28 nm represent the simplest case since only one spectral line is under consideration. Initial analysis employed 4,000 points to define the second-derivative spectrum. The MC results immediately indicated some interesting information. Figures 15 through 17 have a plot showing the retrieved velocities, relative error, and uncertainty spread in the results. Note the constant approximate 2.5% error in the velocity determination of the absorbing specie number density. It should be noted that throughout this report the percent error quoted is that based on the difference between the known quantity (i.e., the value of the parameter utilized in the calculation of the synthetic baseline spectrum) and the average of the retrieved parameter. This constant 2.5% velocity error is due to the coarseness of the frequency spacing in the data and the relatively small Doppler shift due to the slow 150 m/sec velocity. Increasing the number of second-derivative spectral points to 8,000 points reduced the error to approximately 0.1%. Also, in Fig. 17 one can see another effect of increasing the number of points. Note that as the noise level, or uncertainty, increases the uncertainty in the retrieved velocity also increases, in a monotonic fashion. However, for the 4,000-point case the retrieved velocity exhibits a stair-step behavior typical of insufficient



**Figure 15. Actual and Retrieved Average Velocities with 4,000 and 8,000 Points in the Red- and Blue-Shifted Second-Derivative Spectra (Case 1: O<sub>2</sub>).**

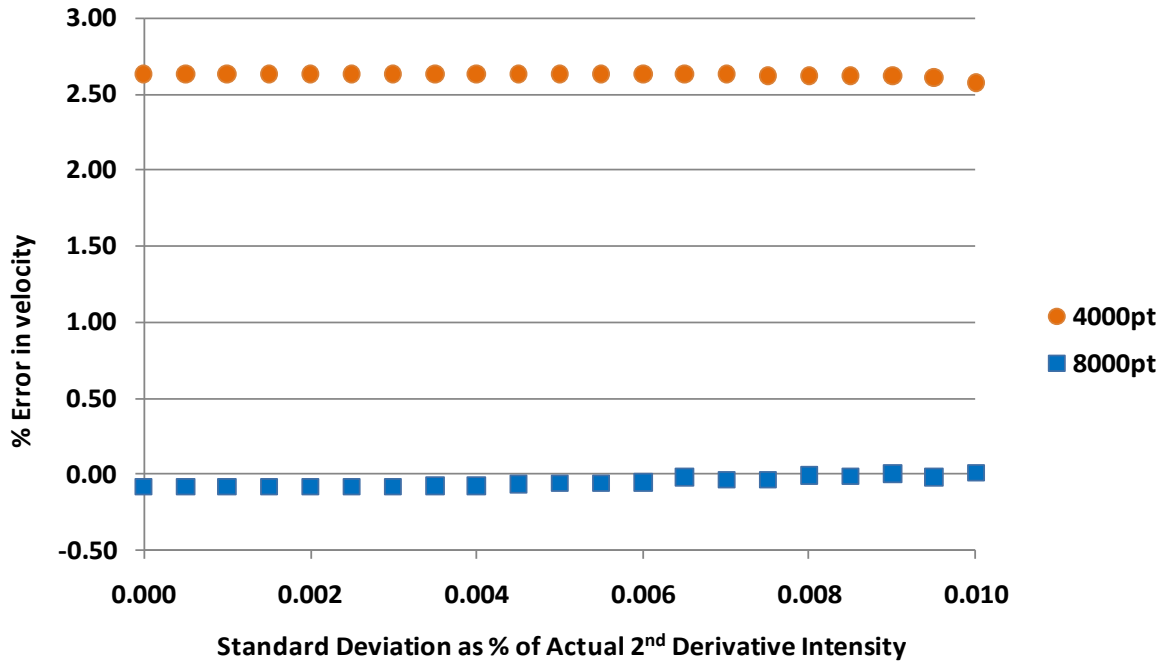


Figure 16. Percent Error in Mean Velocity as a Function of Second-Derivative Spectral Intensity Noise or Uncertainty for 4,000 and 8,000 Points Per Spectrum (Case 1: O<sub>2</sub>)

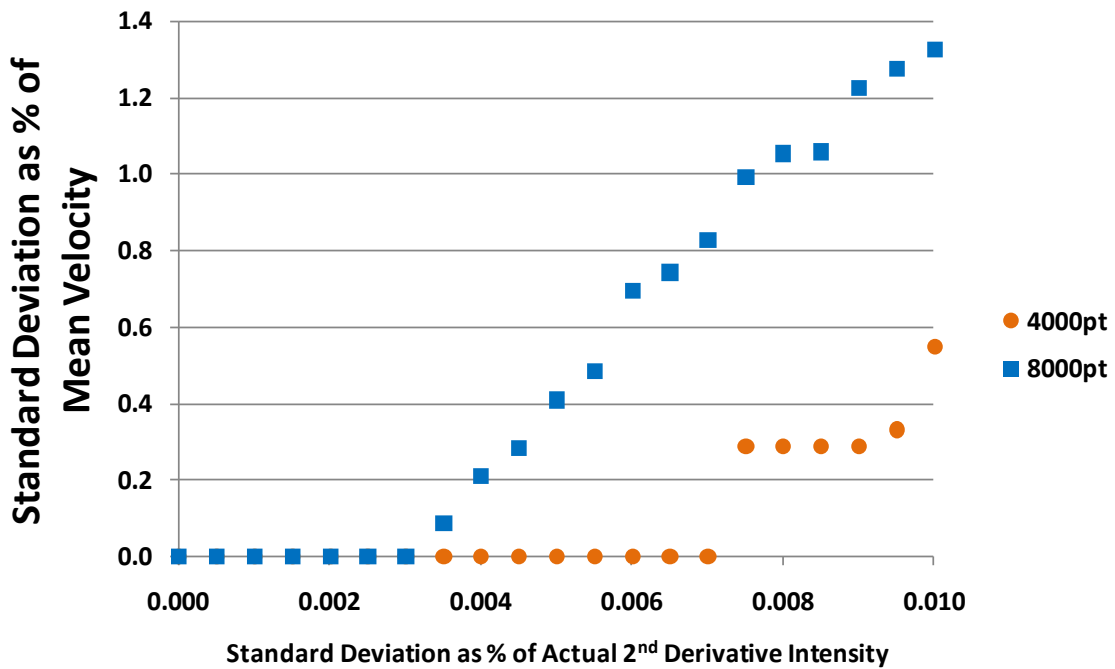
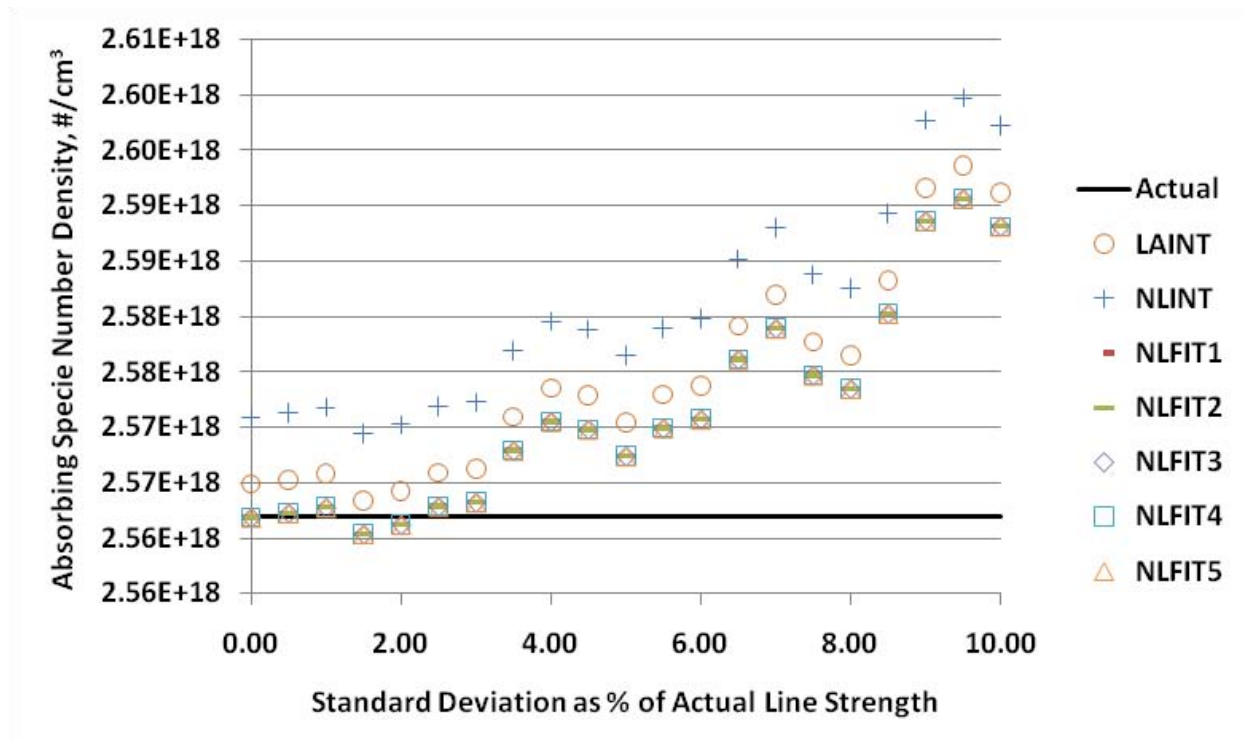


Figure 17. Uncertainty in Velocity as a Percent of the Mean Velocity vs. the Uncertainty in the Second-Derivative Spectral Intensity for 4,000 and 8,000 Points Per Spectra (Case 1: O<sub>2</sub>)

dynamic range. It should be noted here that the data reduction algorithm for velocity employed in this work is based solely on finding the peaks in the blue and red shifted second-derivative spectra by searching for the largest elements in the array. A refinement based on a center-of-mass, quadratic curve fitting, or other techniques may result in better uncertainties and lower error with fewer second-derivative data points.

The absorbing specie number density strongest dependency is on the line strength parameter. Figures 18 through 20 have plots of the retrieved number density of the absorbing specie, its percent error, and its uncertainty as a function of uncertainty in the line strength parameter. Several things are worth noting. The absorbing specie number density error is largest for the line integration techniques LAINT and NLINT. This is because the integration is performed only over the scanned portion of the spectral line. As a result the integrated measured absorbance is less than one would obtain if one could scan over the complete spectrum. The curve-fitting techniques all provided approximately the same mean number density with increasing uncertainty in the line strength. Also, the uncertainty in the retrieved number density varies directly with the uncertainty in the line strength. This is not a surprising result if one notes the line strength parameter and absorbing specie number density always appear as a product in the formulation of the measured spectral transmittance. The mass flux being directly related to the product of the velocity and absorbing specie number density results in a similar error and uncertainty behavior as the absorbing specie number density. The MC output results for the mass flux are shown in Figs. 21 through 23. It should be noted here that this same relationship of the uncertainty in the absorbing specie number density and the mass flux is exhibited in all the following test cases.



**Figure 18. Actual and Mean Number Densities Retrieved from the MC Analysis Using the Seven Data Reduction Methodologies as a Function of Uncertainty in the Spectral Line Strength (Case 1: O<sub>2</sub>)**

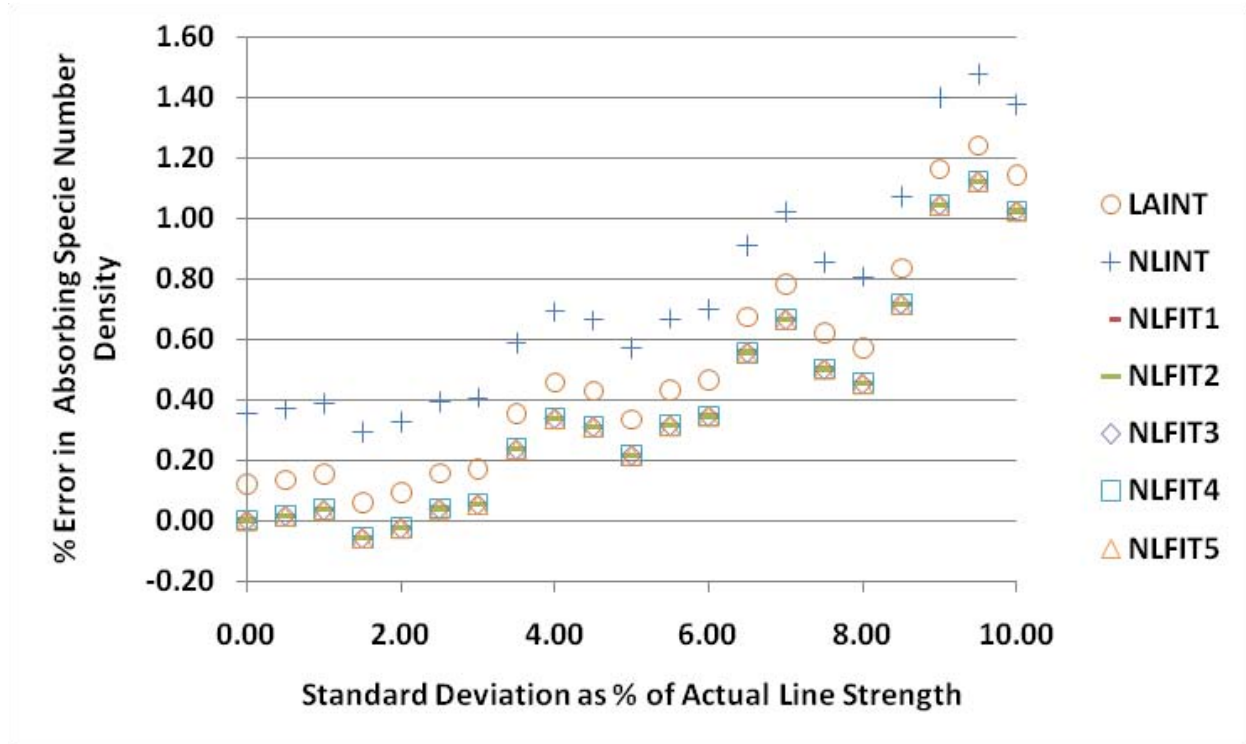


Figure 19. Percent Error in Retrieved O<sub>2</sub> Number Density as a Function of Uncertainty in the Spectral Line Strength (Case 1: O<sub>2</sub>)

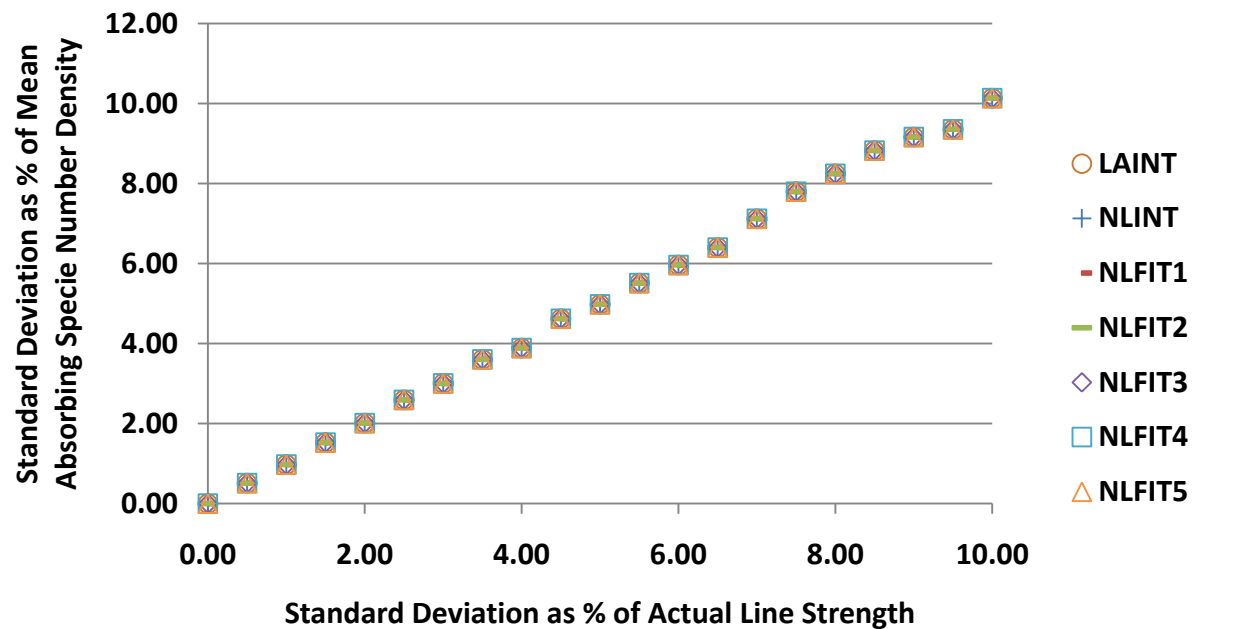


Figure 20. Uncertainty in Retrieved O<sub>2</sub> Number Density as a Function of Uncertainty in the Spectral Line Strength for Various Data Reduction Methodologies (Case 1: O<sub>2</sub>)

It is interesting to note that the integrated absorbance method utilizing the linear absorbance approximation, LAIN, provided better results than the nonlinear integrated absorbance method

NLINT. This was counterintuitive and was further examined. Closer examination discovered that although the nonlinear integrated absorbance model, NLINT, better represented the absorption physical process, the fact that only 400 data points were used in the numerical integration of the synthetic data resulted in another error that yields the serendipitous results. The differences in all the techniques, however, are slight. Figure 20 indicates that regardless of the technique employed the uncertainty in the retrieved absorbing specie number density scales approximately one-to-one with the uncertainty in the spectral line strength parameter.

The pressure-broadening parameters due to air, or foreign gas, and self-broadening parameters typically have rather large uncertainties. The Case 1 condition provides a good example to demonstrate how uncertainty in this parameter can affect retrieved gas properties due to the relatively high pressure (0.5 atm), which will accentuate the pressure broadening. Examination of Figs. 24 and 25 provides insight into these phenomena. First note there is little dependency of the retrieved absorbing specie number density uncertainty on uncertainty in both the foreign or self-broadening parameters for the integrated absorbance techniques LAINT and NLINT. This is not a surprising result since the only dependency on the retrieved absorbing specie number density is through the contribution of the line wing correction. As the spectral line becomes more or less broad due to varying broadening parameters, the limited integration range of the data covers more or less of a spectral line. Therefore, only the relatively small contribution attributable to

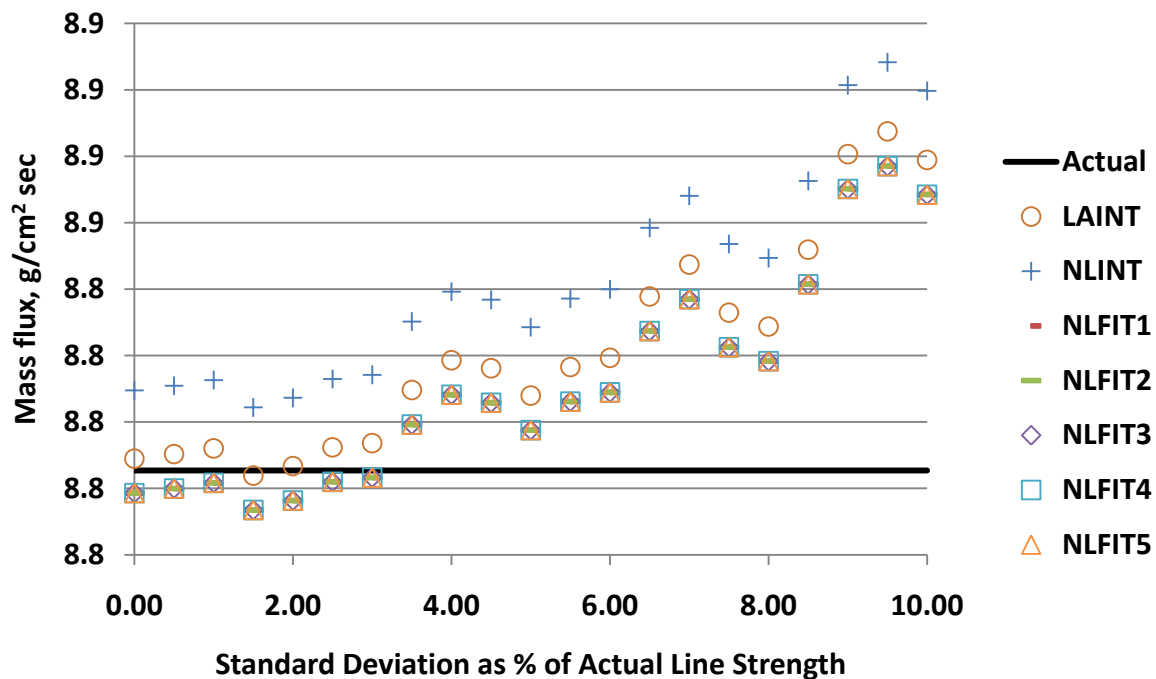


Figure 21. Actual and Mean Values of Mass Flux as a Function of Uncertainty in the Spectral Line Strength for Various Data Reduction Methodologies (Case 1: O<sub>2</sub>)

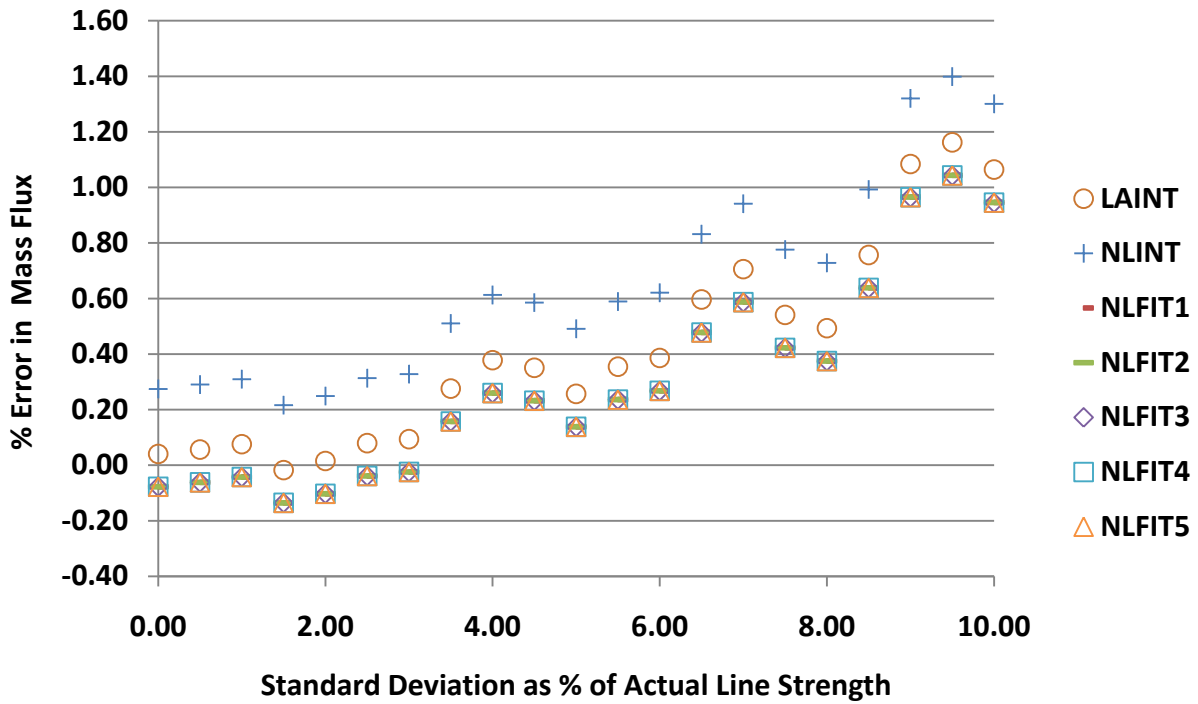


Figure 22. Percent Error in Retrieved Mass Flux as a Function of Uncertainty in the Spectral Line Strength (Case 1: O<sub>2</sub>)

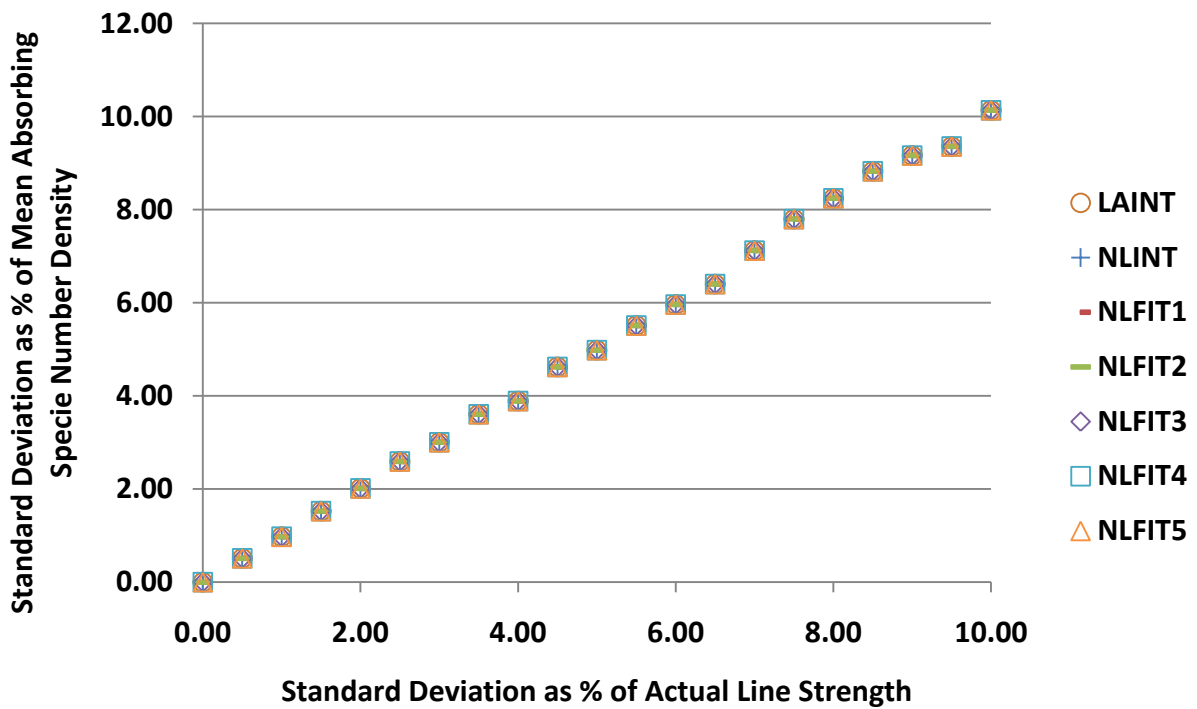


Figure 23. Uncertainty in Retrieved Mass Flux as a Function of Uncertainty in the Spectral Line Strength for Various Data Reduction Methodologies (Case 1: O<sub>2</sub>)

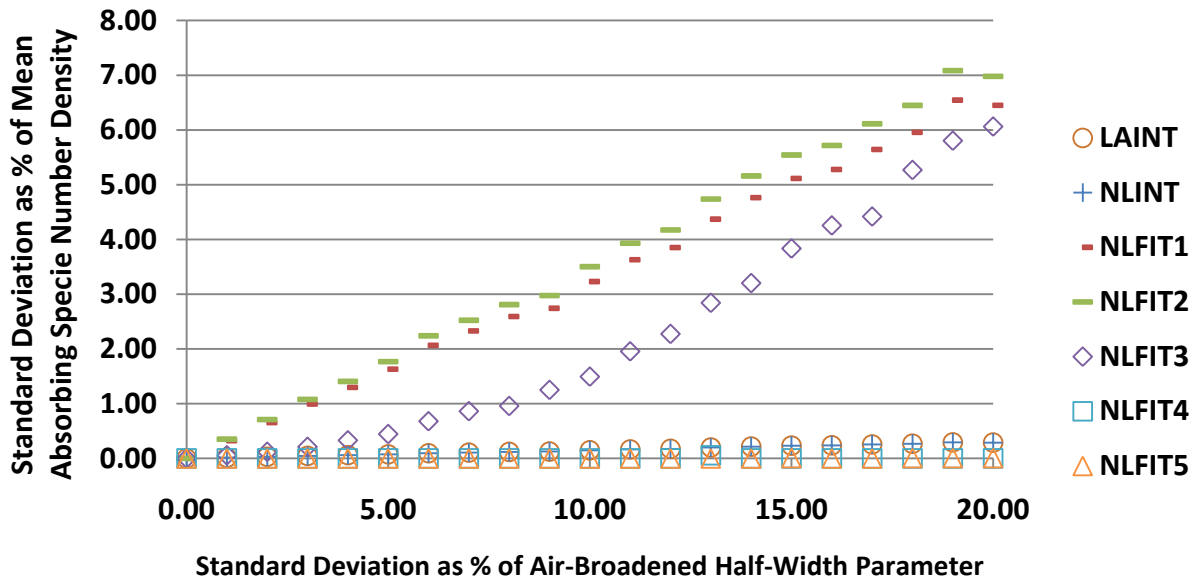


Figure 24. Uncertainty In Retrieved Mass Flux As A Function of Uncertainty In the Spectral Line Foreign Gas Broadening Parameter For Various Data Reduction Methodologies (Case 1: O<sub>2</sub>)

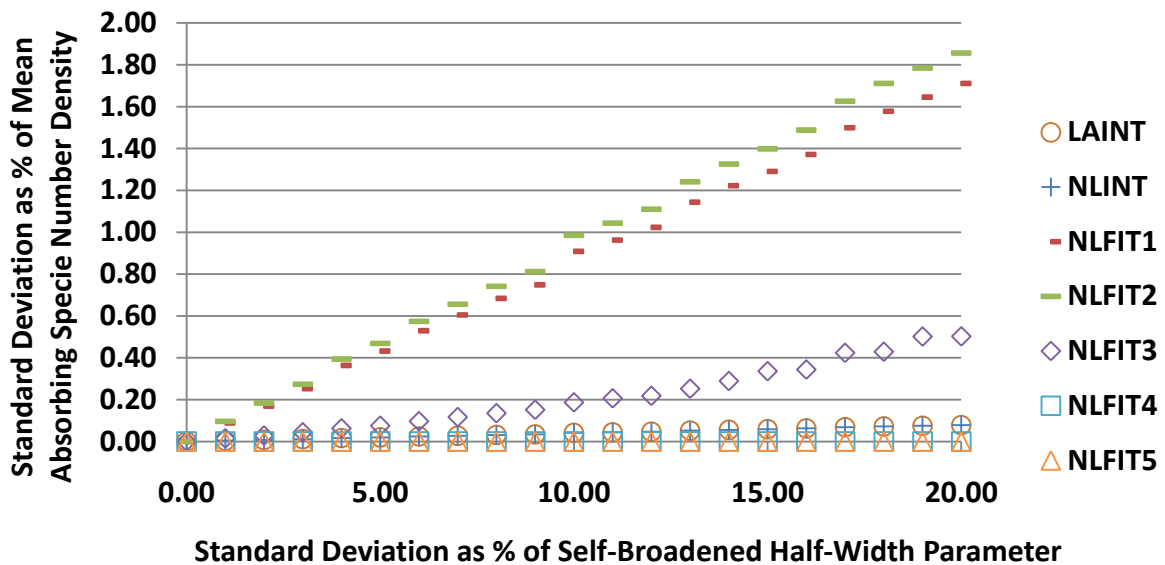


Figure 25. Uncertainty in Retrieved Mass Flux as a Function of Uncertainty in the Spectral Line Self- (O<sub>2</sub>) Broadening Parameter for Various Data Reduction Methodologies (Case 1: O<sub>2</sub>)

the spectral line wings affect the integrated measured absorbance. Performing a fit of the spectral line without adjusting the total number density (NLFIT1-NLFIT3), therefore the pressure, results in a few percent uncertainty in the retrieved absorbing specie number density. This stems from the fact that as the line width varies from the actual value, the nonlinear curve-fitting routines are forced to adjust the absorbing specie number density to minimize the overall residual. This produces an offset from the baseline absorbing specie number density which leads to the increased uncertainty in the absorbing specie number density. Note that for methods NLFIT4 and NLFIT5, in which the total number density is a fit parameter, the uncertainty is lower than the uncertainty obtained from the other nonlinear fit methods. This is because the fitting process is now offsetting the pressure, hence total number density, to compensate for the varying pressure-broadening half-widths. The result is much-reduced uncertainty in the absorbing specie number density at the expense of a large increase in uncertainty in the total number density. This strong connection between the spectral line broadening parameter and total number density is because the spectral line half-width appears as the pressure and broadening parameter product. As a result an uncertainty in one parameter will affect the other. Since  $O_2$  is approximately 20% of air by volume and partial pressure, one sees an approximate 20% less dependence on the  $O_2$  self-broadening uncertainty than the foreign gas broadening parameter uncertainty. This is readily observed by comparing Figs. 24 and 25.

Note that for the NLFIT4 and NLFIT5 methods the total number density is also a fit parameter. The uncertainty in those parameters affecting the pressure broadening has a large effect on the uncertainty in the retrieved total number density as shown in Fig. 26. Figure 26 illustrates the roughly linear relationship between uncertainty in the pressure-broadening parameter and the retrieved total number density. This result should not be surprising since the equations governing the absorption process contain the pressure, hence total number density, and the pressure-broadening parameter as a multiplicative product. Since the pressure-broadening correction is small because the Case 1 condition is near the reference temperature of 296K, the uncertainty dependency on the temperature correction exponent is rather small as illustrated in Fig. 27.

Only a slight temperature adjustment is required to spectral parameters for Test Case 1. This is because of the close proximity in temperature of the conditions of Test Case 1 and the reference temperature of the HITRAN database, 300 K and 296 K, respectively. This results in the small relative functional dependence of the absorbing specie number density on the broadening parameter temperature exponent. Figure 28 shows the resulting weak dependency of the uncertainty of the absorbing specie number density on the uncertainty in the broadening parameter temperature correction exponent. In addition all the retrieved parameters exhibited near-trivial propagated uncertainty due to increased uncertainty in the broadening temperature exponent for Case 1 conditions.

The  $O_2$  transition at 747.28 nm was chosen, in part, due to its relative insensitivity to temperature near the wind tunnel operating condition of approximately 300 K. This was particularly important since the temperature was provided by an independent measurement system that could potentially have a large intrinsic uncertainty. The resulting temperature insensitivity is demonstrated in the uncertainty plot of Fig. 29 which shows only a slight dependence of the uncertainty in the retrieved absorbing specie number density with increased uncertainty in the temperature.

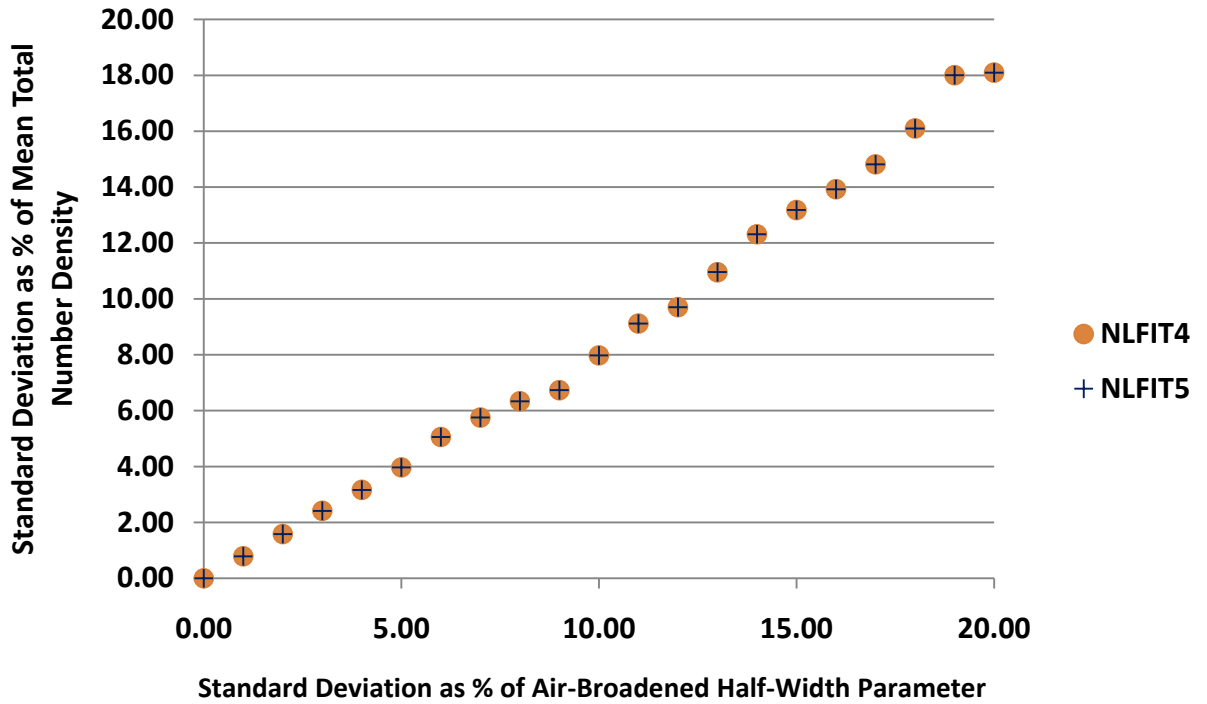


Figure 26. Uncertainty in Retrieved Total Specie Number Density as a Function of Uncertainty in the Pressure Broadening Parameter (Case 1: O<sub>2</sub>)

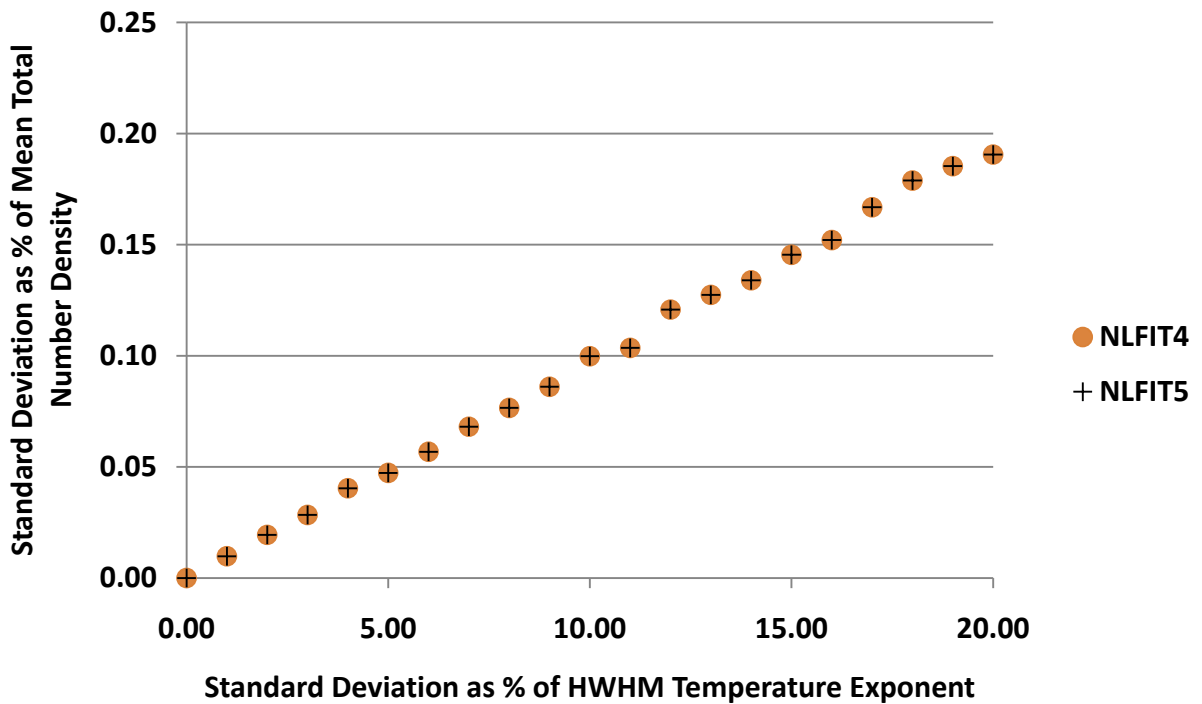


Figure 27. Uncertainty in Retrieved Total Number Density as a Function of Uncertainty in Broadening Temperature Correction Exponent (Case 1: O<sub>2</sub>)

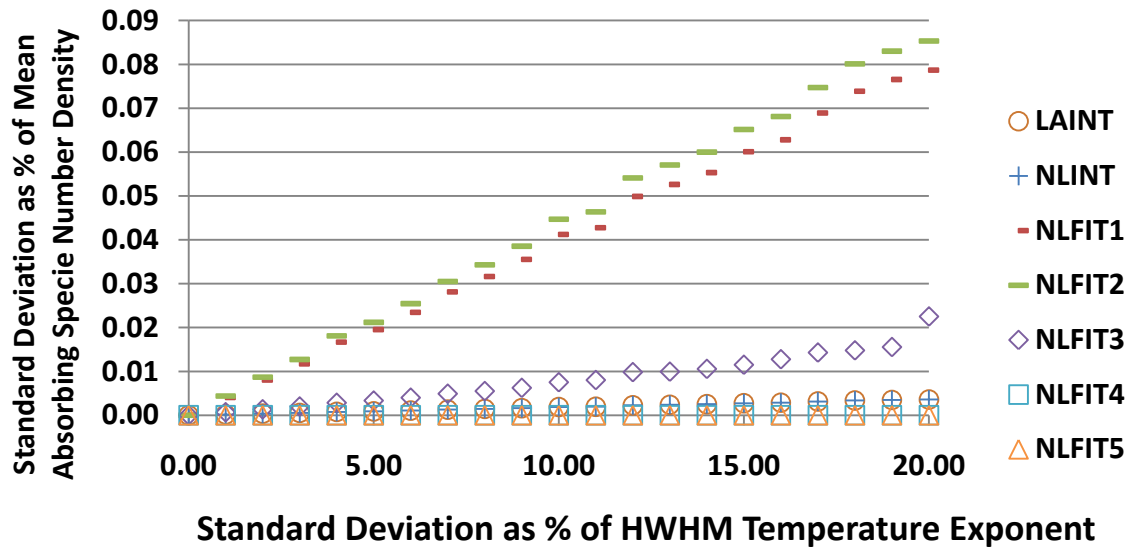


Figure 28. Uncertainty in Retrieved Absorbing Specie Number Density as a Function of Uncertainty in the Spectral Line Width Temperature Adjustment Exponent for Various Data Reduction Methodologies (Case 1: O<sub>2</sub>)

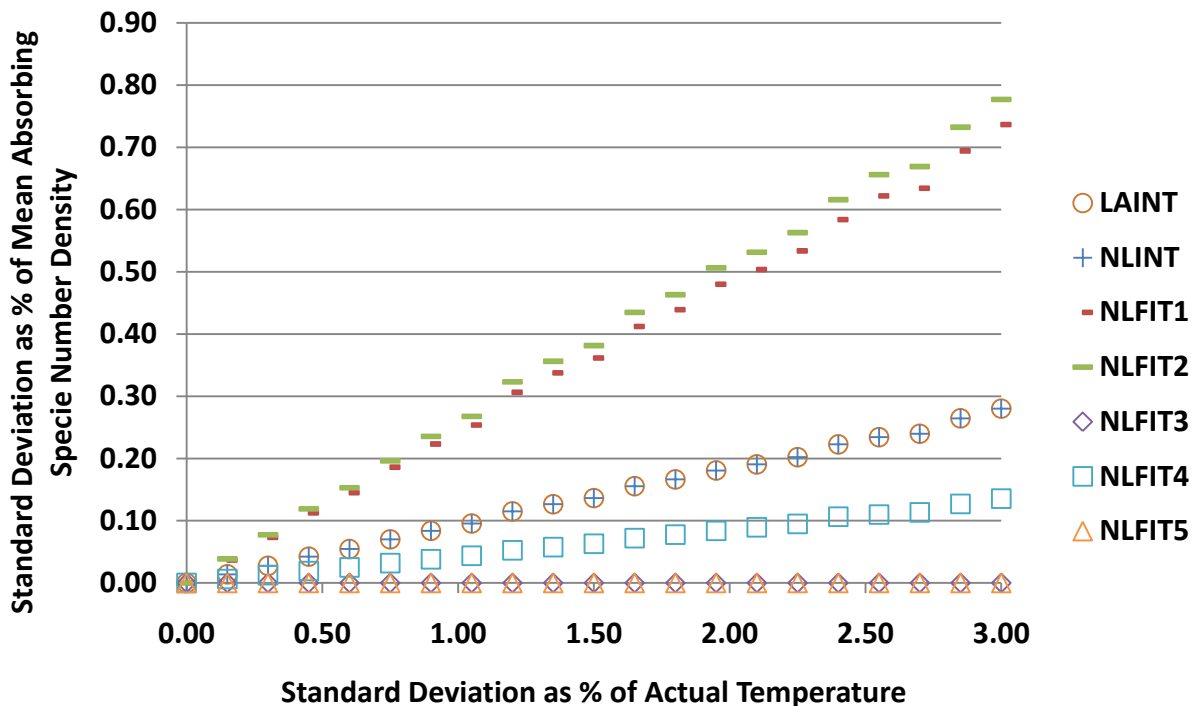
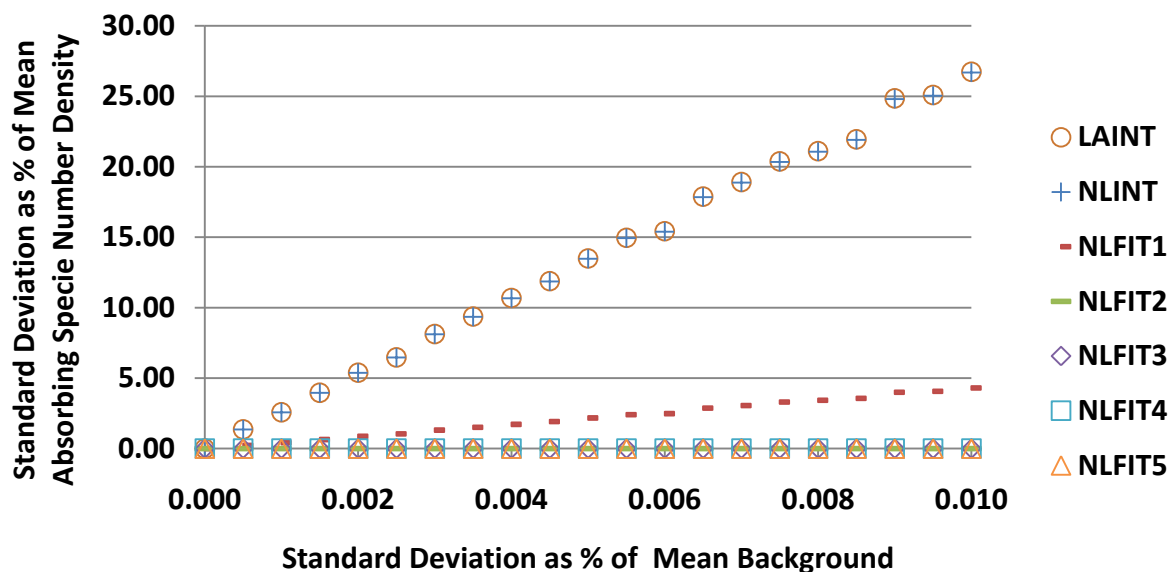


Figure 29. Uncertainty in Retrieved Absorbing Specie Number Density as a Function of Uncertainty in the Temperature (Case 1: O<sub>2</sub>)

One of the parameters with the greatest effect on uncertainty of retrieved parameters is the noise on the measured laser intensity. This fact is demonstrated in the plot of Figs. 30 and 31. Figure 30 shows the uncertainty in the retrieved absorbing specie number density vs. the uncertainty in the mean background level. This represents a scenario where the measured or inferred baseline or unattenuated intensity deviates from the actual baseline. It should be noted here that in all the ensuing discussions the baseline was assumed not to be optical frequency-dependent. This is rarely, if ever, the case, and one typically has some variability of laser intensity with optical frequency. However, the following calculations and discussions are still relevant in assessing the relative importance of background shift and signal-to-noise ratio on TDL absorption gas diagnostics. What is evident is that those data reduction methodologies that rely on simultaneous curve fitting the background level with the gas properties (i.e., methods NLFIT2 - NLFIT5) performed a much better job of not propagating the uncertainty in the mean background level. The one nonlinear fit method that does not fit the background (NLFIT1), but uses the provided background level, performed better than the integrated absorbance techniques but remained far inferior to other nonlinear fit methodologies.

The noise on the attenuated intensity has a similar effect on the uncertainty in the absorbing specie number density as shown in Fig. 31. However, all the nonlinear curve-fitting-based reduction methods exhibit much better results, or less propagated uncertainty, in absorbing specie number density, than the integrated absorbance techniques.

The temperature dependence of a single line absorption feature is obtained through the spectral line shape. The temperature dependence is predominately through the pressure broadening. This fact makes the retrieved temperature very sensitive to this particular spectral parameter. Figure 32 illustrates the sensitivity of the uncertainty of the retrieved temperature to uncertainty in the pressure-broadening parameter. From Fig. 32 one sees that the uncertainty for the retrieved temperature is approximately one and half times the uncertainty in the pressure-broadening parameter which can easily have a one sigma uncertainty on the order of 10 to 20% or more.



**Figure 30. Uncertainty in Retrieved Absorbing Specie Number Density as a Function of Uncertainty in the Mean Background Level (Case 1: O<sub>2</sub>)**

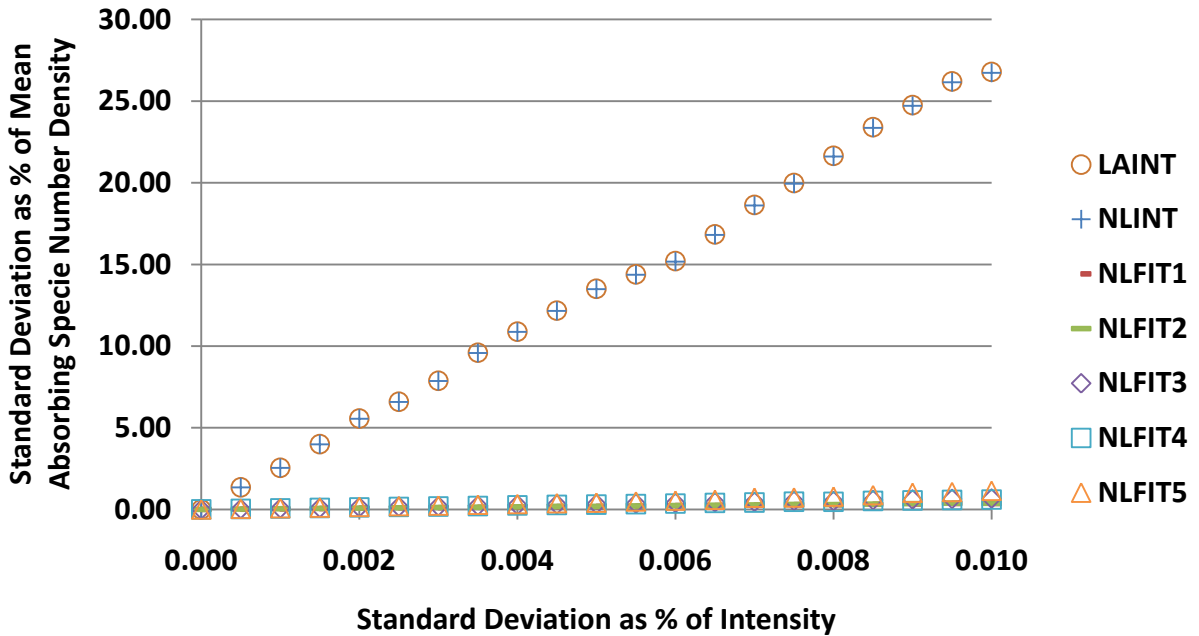


Figure 31a. Uncertainty in Retrieved Absorbing Specie Number Density as a Function of Uncertainty in Intensity (Case 1: O<sub>2</sub>)

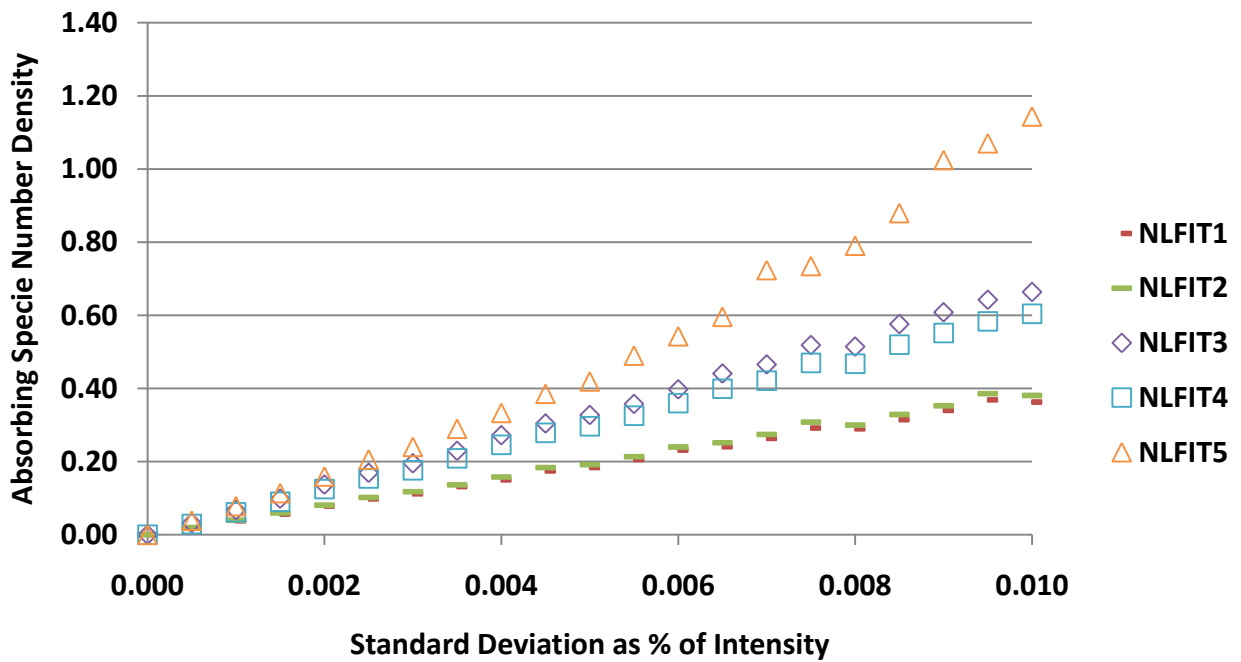
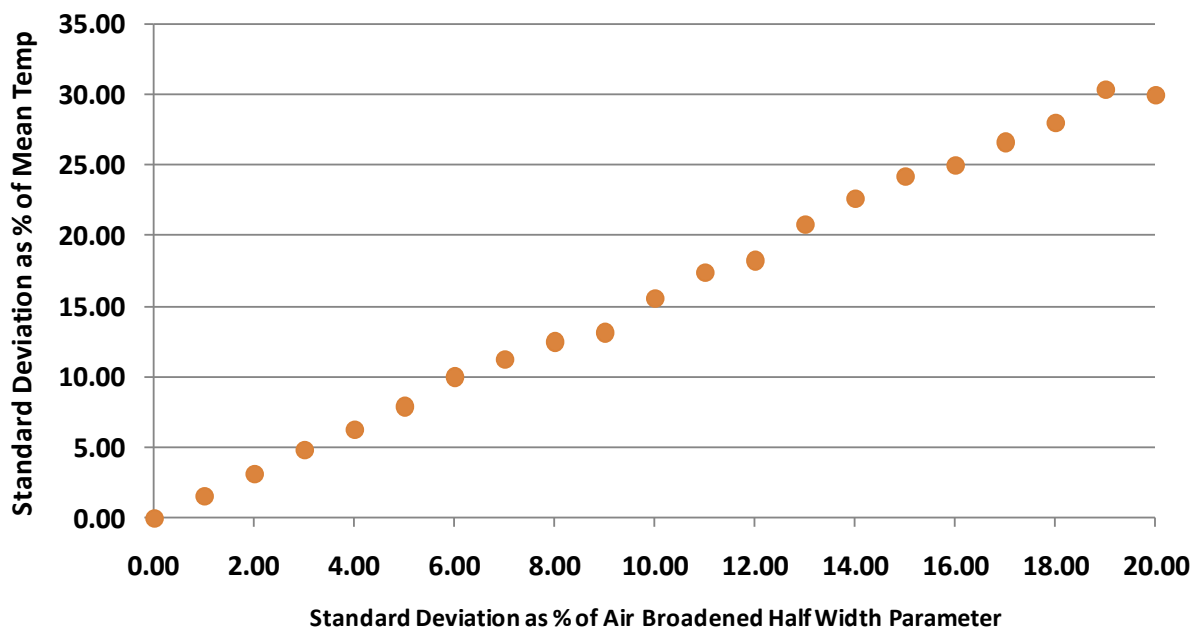


Figure 31b. Uncertainty in Retrieved Absorbing Specie Number Density as a Function of Uncertainty in Intensity (Case 1: O<sub>2</sub>)

## NLFIT3 Method



**Figure 32. Uncertainty in Retrieved Temperature as a Function of Uncertainty in the Air or Foreign Gas Broadening Parameter (Case 1: O<sub>2</sub>)**

### 7.2 CASE 2 AND 3: H<sub>2</sub>O

Test cases 2 and 3 represent a scenario of very weak absorption, multiple spectral lines, elevated temperatures, and low pressures. O'Bryne employed this particular spectral region for measurements of water downstream of a combustor in a flow with a temperature near 900 K. Here, the same 12 spectral lines employed by O'Bryne are employed (Table 4) at temperatures of 1,000 K and 2,000 K. The pressure considered is 0.01 atmospheres with a water mole fraction of 10% that would be representative of a high-speed vehicle test condition. The number densities are low due to the high temperatures and low pressures. This results in a much smaller water number density than those observed by O'Bryne who operated at a lower temperature and at atmospheric pressure. The reduced absorbing specie number density results in a very weak set of absorption features. The velocity chosen for these two cases, and the following Test Case 4, was 1500 m/sec to replicate what one would expect in a high-speed engine test environment.

The higher velocity of case 2 and 3 allowed the use of 4,000 points in the second-derivative spectrum rather than the 8,000 points for the slower speed (150 m/sec) Case 1 calculations. Examination of Fig. 33 shows the velocity error is relatively constant at 0.66% and is actually decreasing in the high-temperature case for increasing second-derivative spectral intensity noise. The constant error at low-noise conditions is due to the limited number of data points (4,000) utilized in the second-derivative spectrum. However, note in Fig. 34 that the uncertainty in the retrieved velocity is increasing with increasing uncertainty in the intensity for the 2,000 K condition and is relatively constant near 0 for the 1,000 K case. This is because at the increased temperature (at constant pressure) the number density and hence the absorption is decreasing. As a result, the noise has a more pronounced effect on the 2,000 K data that

possesses weaker absorption features. Note in comparison to Test Case 1 (oxygen at 0.5 atmospheres and 300 K) results shown in Figs. 16 and 17 the overall error is approximately the same using the 8,000 points in the slower speed Test Case 1 calculations. Similar results are obtained for the mass flux variation with second-derivative spectral intensity since the mass flux is a simple linear relationship to the product of the velocity and density.

The propagated uncertainty due to the line strength parameter significantly impacts the uncertainty in the retrieved absorbing specie number density and mass flux. Figures 35 through 37 have plots that show the dependency of the retrieved absorbing specie number density, percent error, and uncertainty in absorbing specie number density with uncertainty in the line strengths for the various data reduction methods for Test Case 2 (1,000 K). It is interesting to note the comparison to the oxygen absorption (Case 1) results of Figs. 18 through 20. The scatter in the absorbing specie number density for the Case 2 results is significant in comparison to the approximately linearly increasing results for Case 1. These are attributable to the fact that 12 H<sub>2</sub>O spectral lines are employed in the Case 2 calculations vs. only one O<sub>2</sub> line for the Case 1 calculations. The Monte Carlo simulations performed here assume the uncertainties in the line strengths, or other molecule-specific parameters, are uncorrelated. That is to say, the uncertainties in each individual spectral line parameter are independent of other parameters and spectral lines. This independence in the distribution of uncertainty among several spectral lines is a key contributor to the increased scatter observed in Cases 2 and 3. It is also noted that there is an increase in the uncertainty and error of the absorbing specie number density with data reduction methods NLFIT3 and NLFIT5 over the other methods.

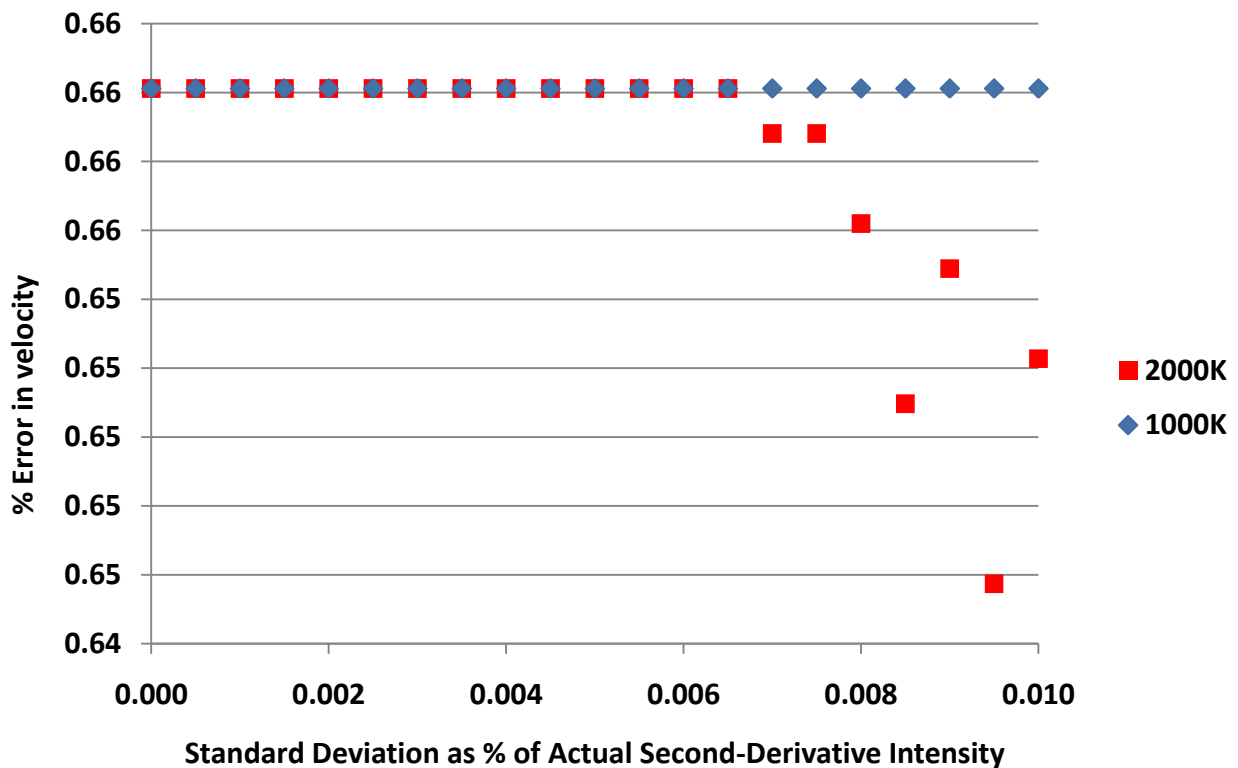


**Figure 33. Error in Retrieved Velocity a Function of Uncertainty in the Second-Derivative Spectral Intensity for Case 2 (1,000 K) and Case 3 (2,000 K) Conditions**

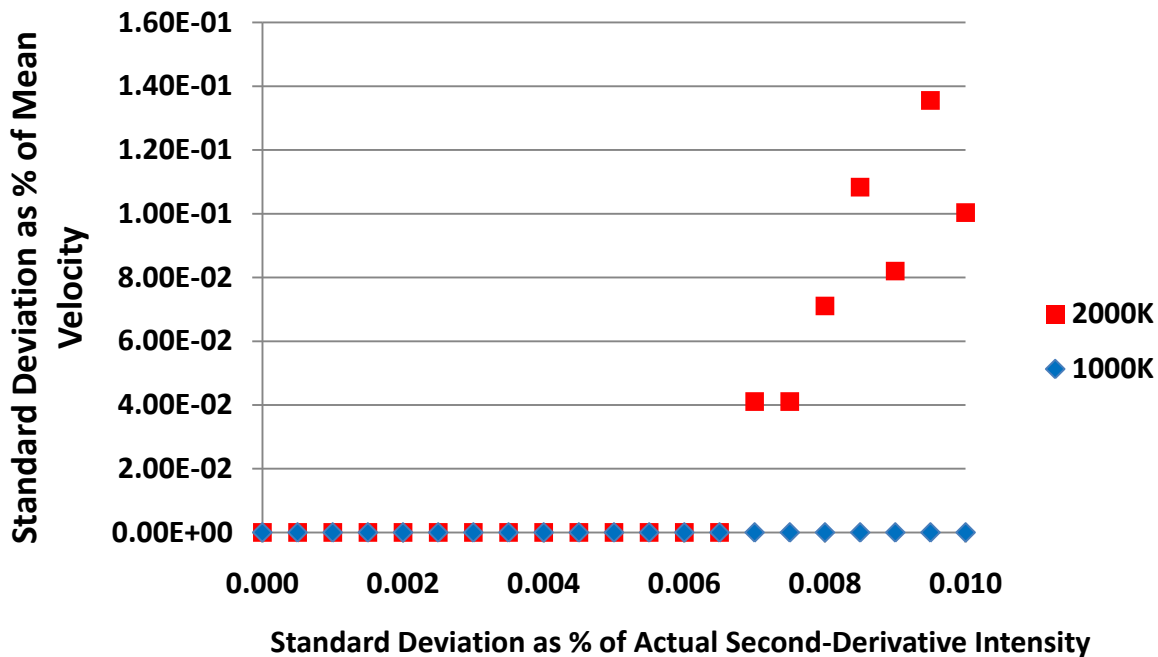


**Figure 34. Uncertainty in Retrieved Velocity a Function of Uncertainty in the Second-Derivative Spectral Intensity for Case 2 (1,000 K) and Case 3 (2,000 K) Conditions**

The common element in methods NLFIT3 and NLFIT5 is that each of these methods has temperature as a fit parameter. Other nonlinear methods produce approximately half the uncertainty in absorbing specie number density due to uncertainty in the line strength for Case 2 compared to Case 1 results. Again, this is attributable to the use of 12 uncorrelated spectral lines rather than a single spectral line for the Case 1 results. Figures 38 through 40 are plots of the retrieved absorbing specie number density for the higher temperature and resulting lower density Case 3 results. Note that the Case 3 (2,000 K) propagated uncertainty is approximately twice that of the Case 2 (1,000 K) results for NLFIT3 and NLFIT5 and approximately the same for the other methods. NLFIT3 and NLFIT5 methods each simultaneously fit for temperature and absorbing specie number density. It is likely that the line-to-line deviation in the line strength is compensated for by fitting the temperature. This in turn will result in a deviation in the resulting absorbing specie number density which is more susceptible to the overall spectral fit than the line-to-line variability of the spectrum. The mass flux results practically mirror the results for the absorbing specie number density and are not included for the sake of brevity.

Temperature also exhibited a strong dependence on uncertainty in line strength. Figures 41 through 43 show the effects of uncertainty in line strength on the retrieved temperature. It should be noted that for the single O<sub>2</sub> line of Case 1 the temperature dependence was almost exclusively through the line width dependence. However, for Cases 2 and 3 the pressure is much reduced, thereby lessening the temperature dependence through the line width. The bulk of the temperature dependency for Cases 2 and 3 is through the temperature-adjusted line strengths. This shifts the temperature dependence, hence the uncertainty propagation, to the line strength parameters. From Figs. 41 through 43 it is seen that the uncertainty in the temperature increases approximately linearly with the uncertainty in the line strengths. Also, it is apparent that simultaneous fitting for the total number density in the NLFIT5 method increases the uncertainty in the retrieved temperature over the NLFIT3 method that has a fixed total number density.

Spectral line pressure-broadening effects did not present a significant impact for Test Cases 2 and 3 on temperature or absorbing specie number density as observed in Figs. 44 through 46. This nonsensitivity is due to the low pressure and hence the low-pressure broadening dependency. This is borne out by examining Fig. 45 in which the sensitivity is slightly higher for Case 2 (1,000 K) case than Case 3 (2,000 K) due to the increased pressure. Even the retrieved temperature is relatively unaffected by uncertainty in the temperature correction exponent for the broadening parameters as seen in Fig. 46. This reinforces the obvious, that is, the temperature dependence is obtained primarily by the variability of line strengths with temperature rather than the line widths at these low pressures. However, the total number density, or pressure, is greatly affected by the pressure-broadening-related parameters. Examination of Figs. 47 through 49 illustrates the severity of the propagated uncertainties. Note that at the higher temperature (2,000 K) the uncertainty in the temperature correction exponent has a greater effect than the lower temperature Case 2 (1,000 K). This strong dependence on the pressure broadening is due to the low-pressure and high-temperature conditions giving rise to a low-pressure broadening component to the spectral line width.

A somewhat unexpected result is the dependence of the total number density uncertainty on the uncertainty in the line strength. The plots in Figs. 50 and 51 illustrate the significance of the large uncertainties. To better understand this phenomena, one has to recall that the total number density will appear functionally in the form of the product of the total number density, through the pressure, and the pressure-broadening parameter (i.e., through Eq. [13]). The broadening parameter scales inversely with temperature according to Eq. (14) and, for Cases 2 and 3, the pressure is at a low level of 0.01 atmospheres, thereby producing small pressure-broadened half-widths. Calculation of the pressure-broadening HWHM yields approximately  $2.5 \times 10^{-5}$  and  $1.4 \times 10^{-5} \text{ cm}^{-1}$  for Cases 2 and 3, respectively, whereas the pressure-broadened HWHM for Case 1 is on the order of  $0.025 \text{ cm}^{-1}$ . The Doppler HWHM for Cases 1, 2, and 3 are approximately 0.014, 0.027, and  $0.038 \text{ cm}^{-1}$ , respectively. Therefore, the contribution to the overall line width, or spectral absorbance profile, by varying the total number density is relatively small in comparison to the contribution by the Doppler HWHM at the elevated temperature conditions of Cases 2 and 3. This implies that the variation in line strength perturbs the total number density results indirectly through the strong temperature dependence of the spectral line widths at these conditions. One can see by examining Fig. 51 that the higher temperature (lower number density and pressure) case has a larger associated uncertainty in retrieved number density than the lower temperature (higher number density and pressure). This again reinforces the above arguments and indicates the difficulty of using spectral line width measurements for determining pressure, or total number density, in a high-temperature, low-pressure environment.

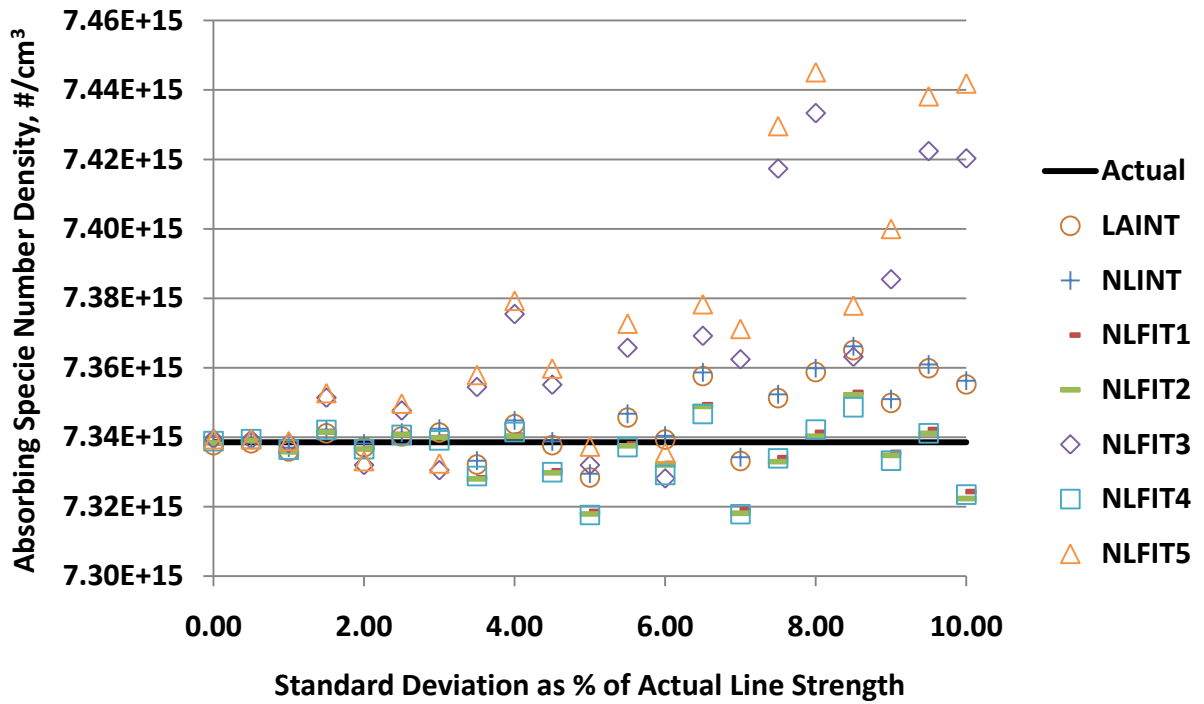


Figure 35. Retrieved Absorbing Specie Number Density vs. Uncertainty in Line Strength of for Case 2 Condition at 1,000 K

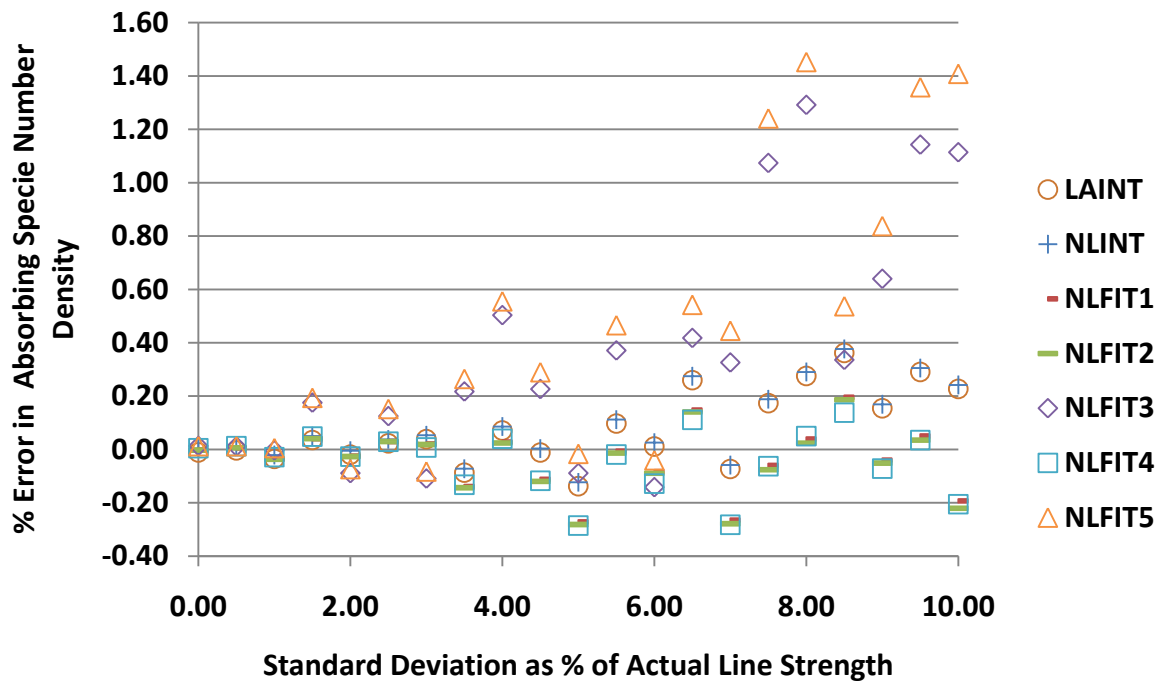


Figure 36. Retrieved Absorbing Specie Number Density Error vs. Uncertainty in Line Strength for Case 2 Condition at 1,000 K

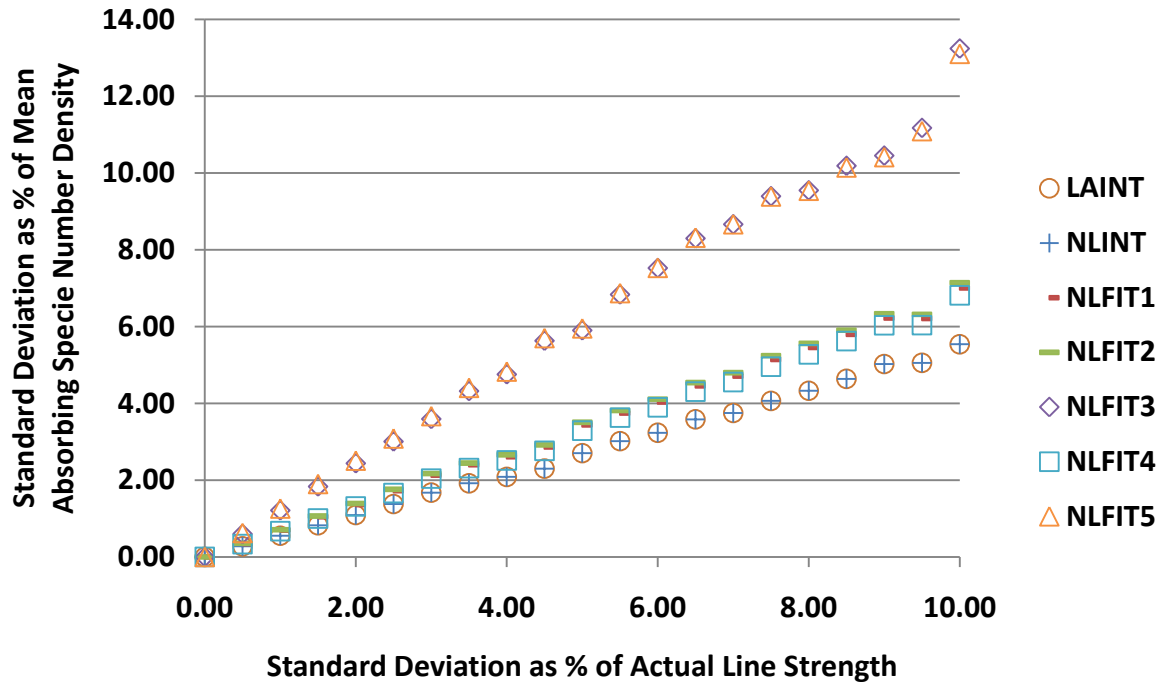


Figure 37. Uncertainty in Retrieved Absorbing Specie Number Density Error vs. Uncertainty in Line Strength for Case 2 Condition at 1,000 K

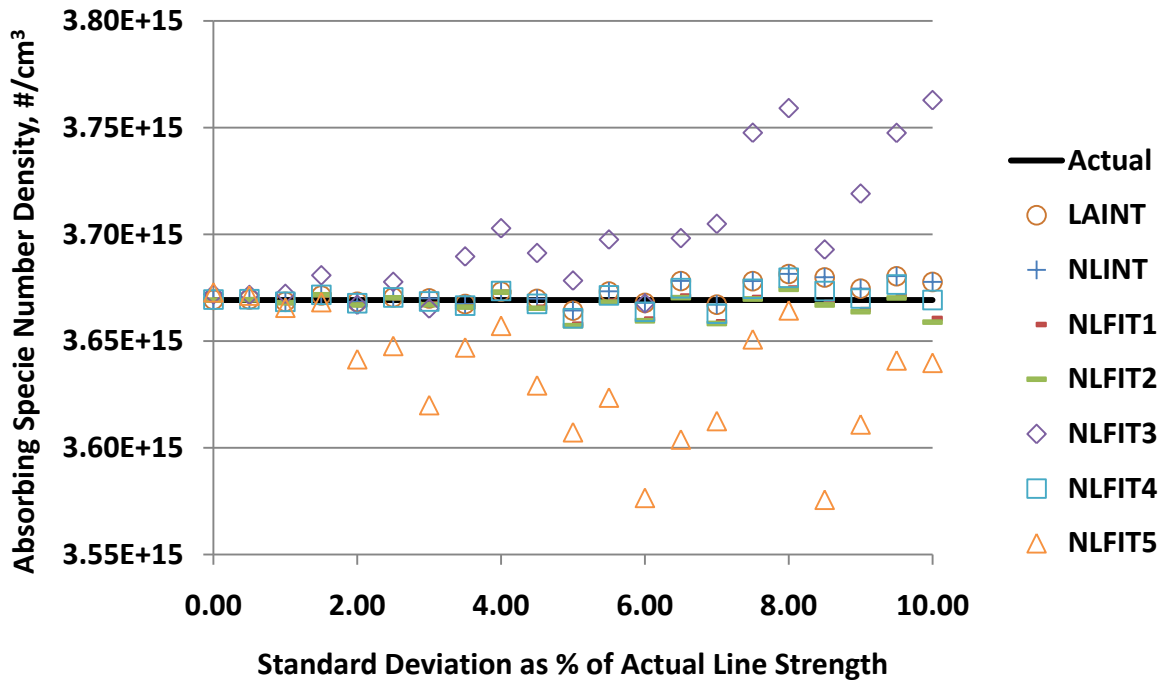


Figure 38. Retrieved Absorbing Specie Number Density vs. Uncertainty in Line Strength for Case 3 Condition at 2,000 K

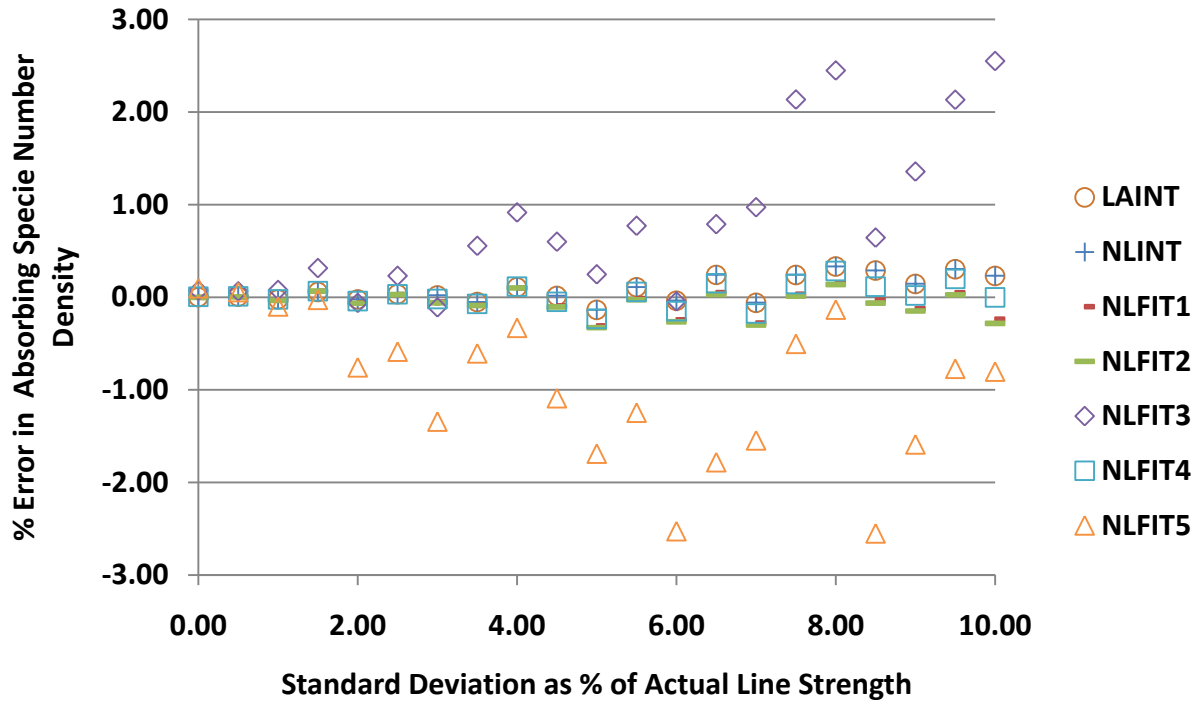


Figure 39. Retrieved Absorbing Specie Number Density Error vs. Uncertainty in Line Strength for Case 3 Condition at 2,000 K

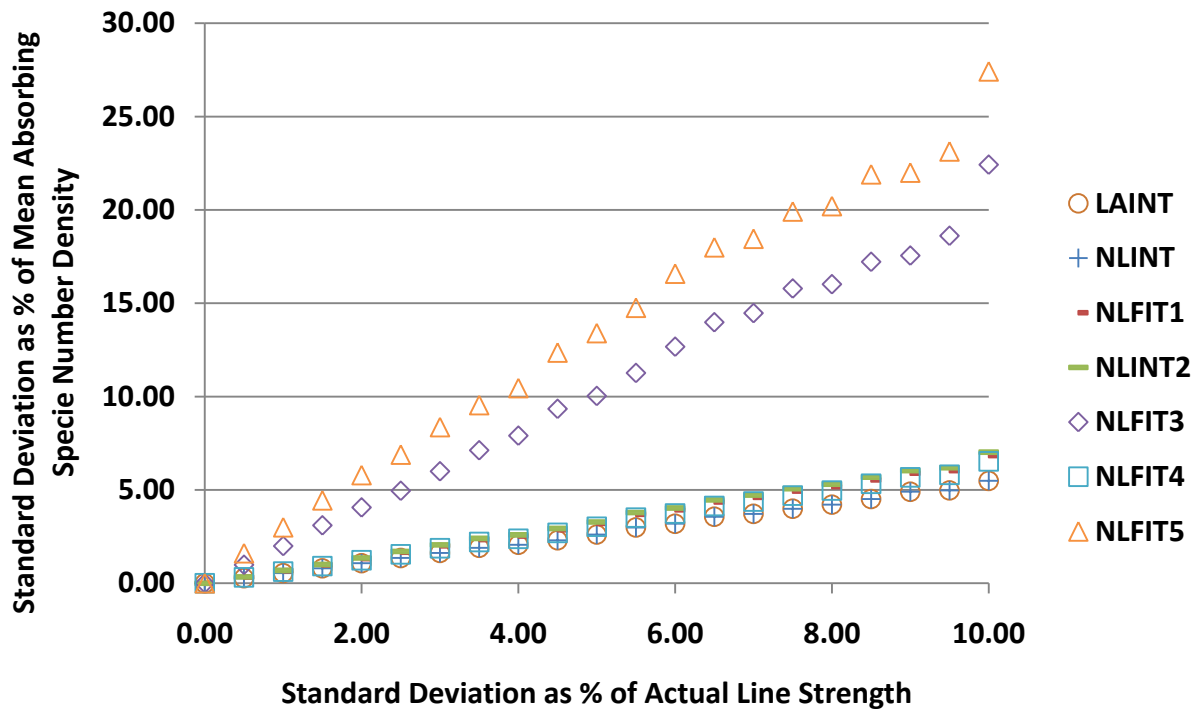


Figure 40. Uncertainty in Retrieved Absorbing Specie Number Density Error vs. Uncertainty in Line Strength for Case 3 Condition at 2,000 K

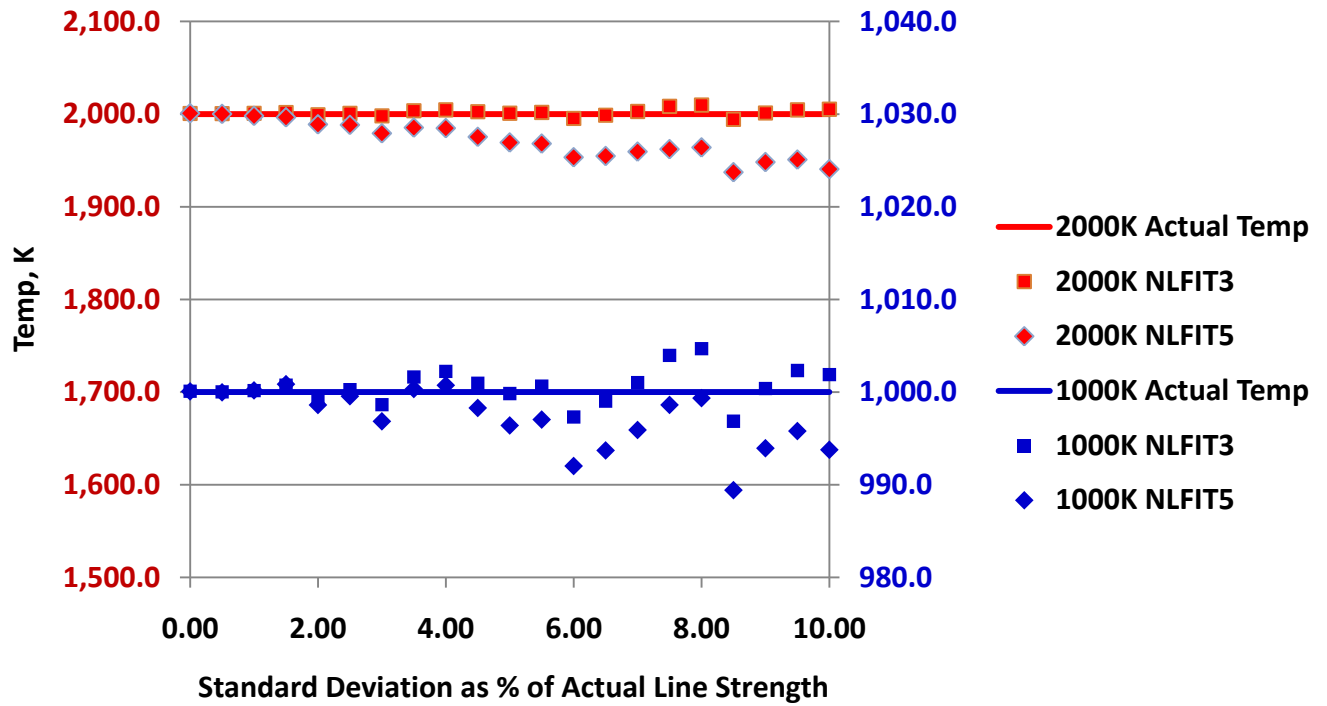


Figure 41. Actual and Retrieved Temperature for Case 2 (1,000 K) and Case 2 (2,000 K) Conditions vs. Uncertainty in Line Strengths

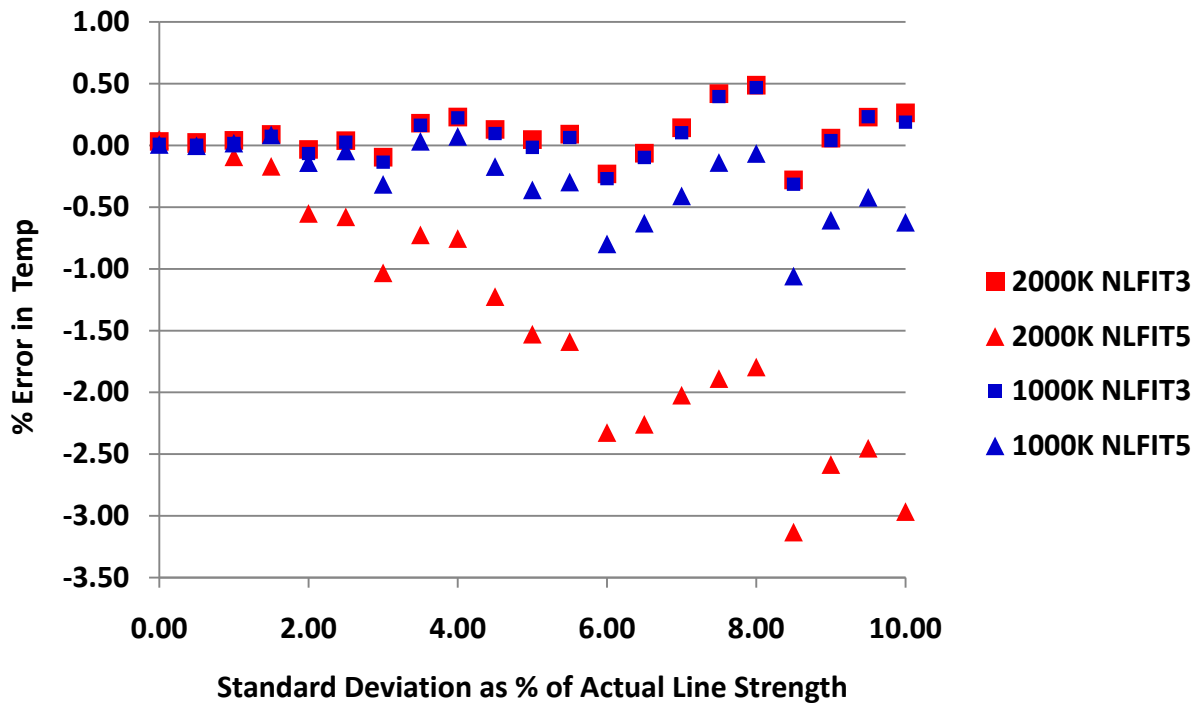


Figure 42. Error in Average Retrieved Temperatures for Case 2 (1,000 K) and Case 2 (2,000 K) Conditions vs. Uncertainty in Line Strengths

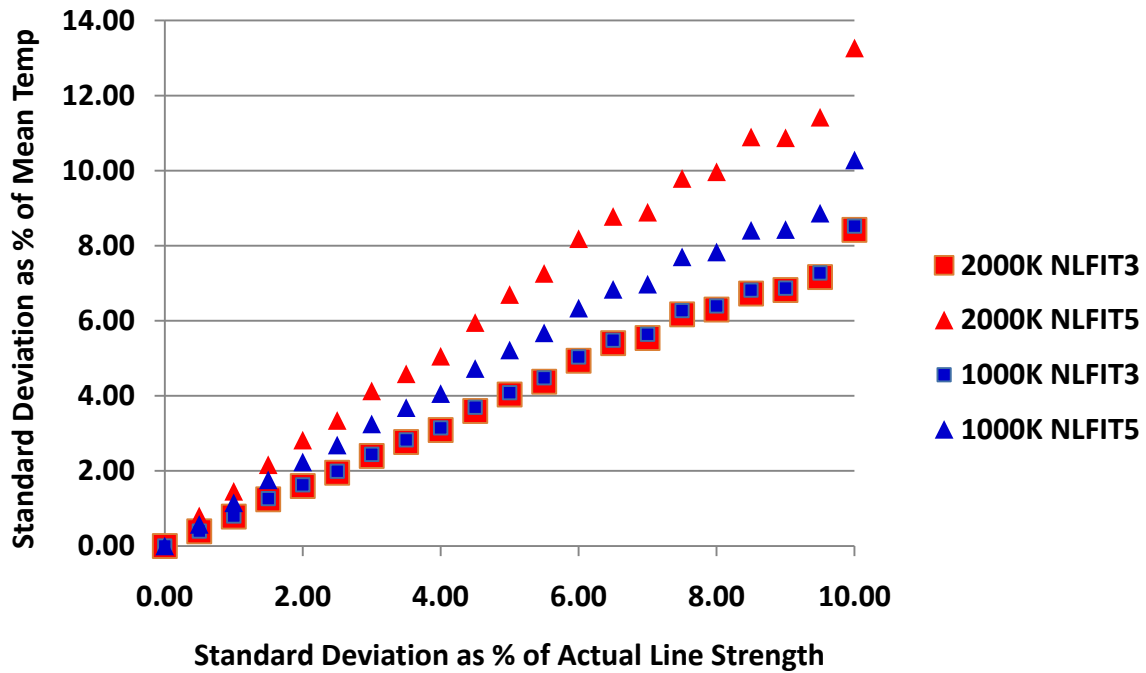


Figure 43. Uncertainty in Retrieved Temperature for Case 2 (1,000 K) and Case 3 (2,000 K) Conditions vs. Uncertainty in Line Strength.

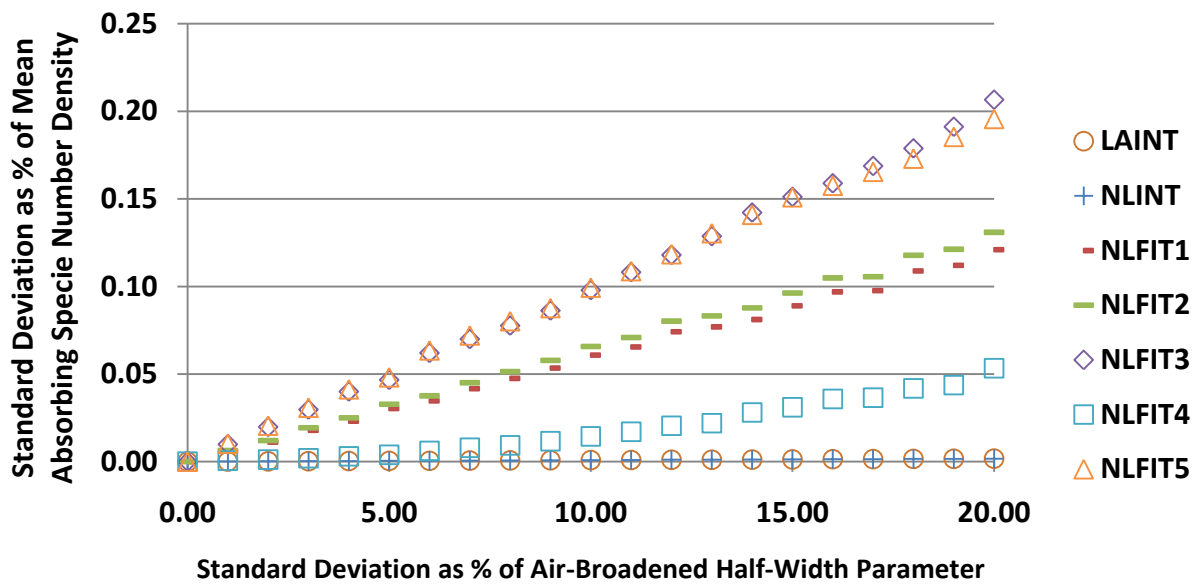


Figure 44. Uncertainty in Retrieved Absorbing Specie Number Density for Case 2 (1,000 K) vs. Uncertainty in Air Pressure Broadening Parameters

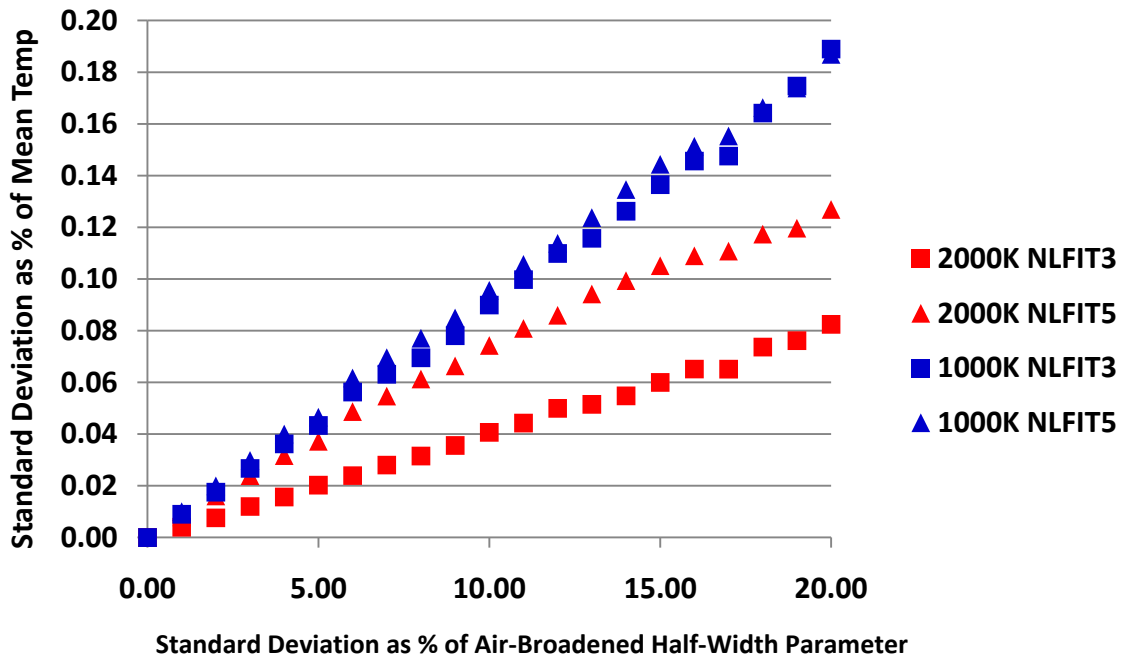


Figure 45. Uncertainty in Retrieved Temperature for Cases 2 and 3 (1,000 K and 2,000 K) vs. Uncertainty in the Air Pressure Broadening Parameter

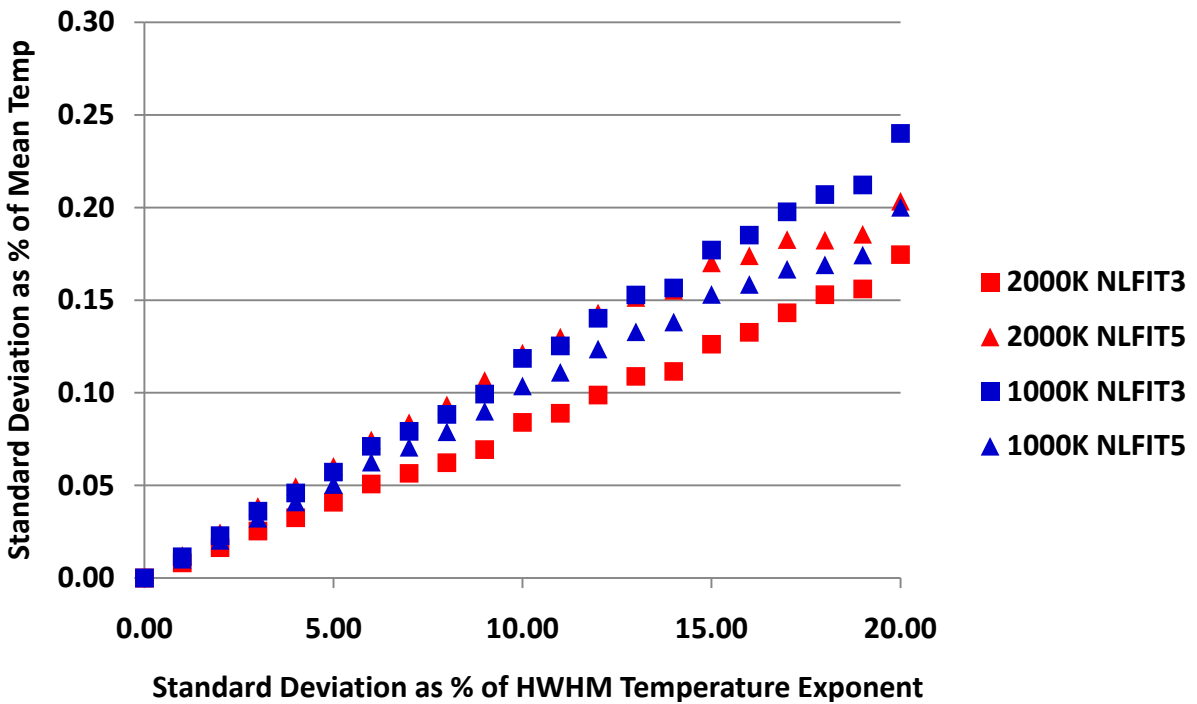


Figure 46. Uncertainty in Retrieved Temperature for Cases 2 and 3 (1,000 K and 2,000 K) vs. Uncertainty in the Air Pressure Broadening Parameter Temperature Correction Exponent

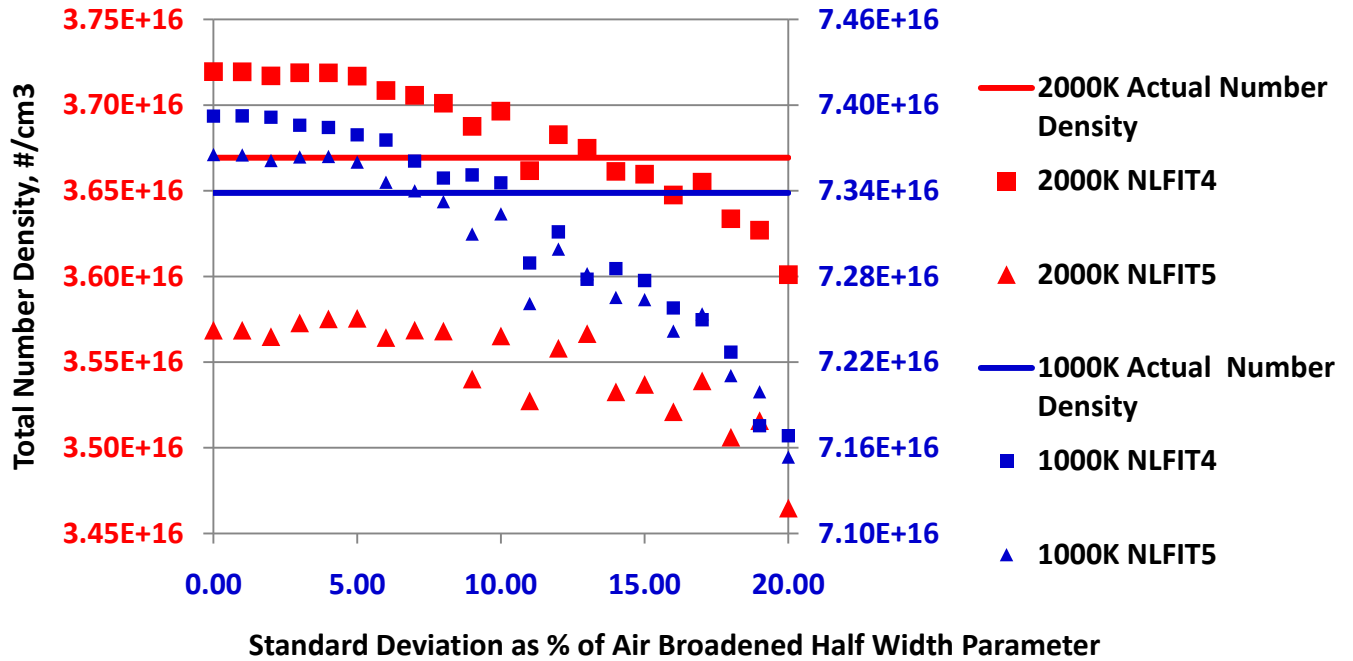


Figure 47. Actual and Retrieved Mean Total Number Densities for Cases 2 and 3 (1,000 K and 2,000 K) vs. Uncertainty in the Air Pressure Broadening Parameter. Blue symbols are associated with the right y-axis.

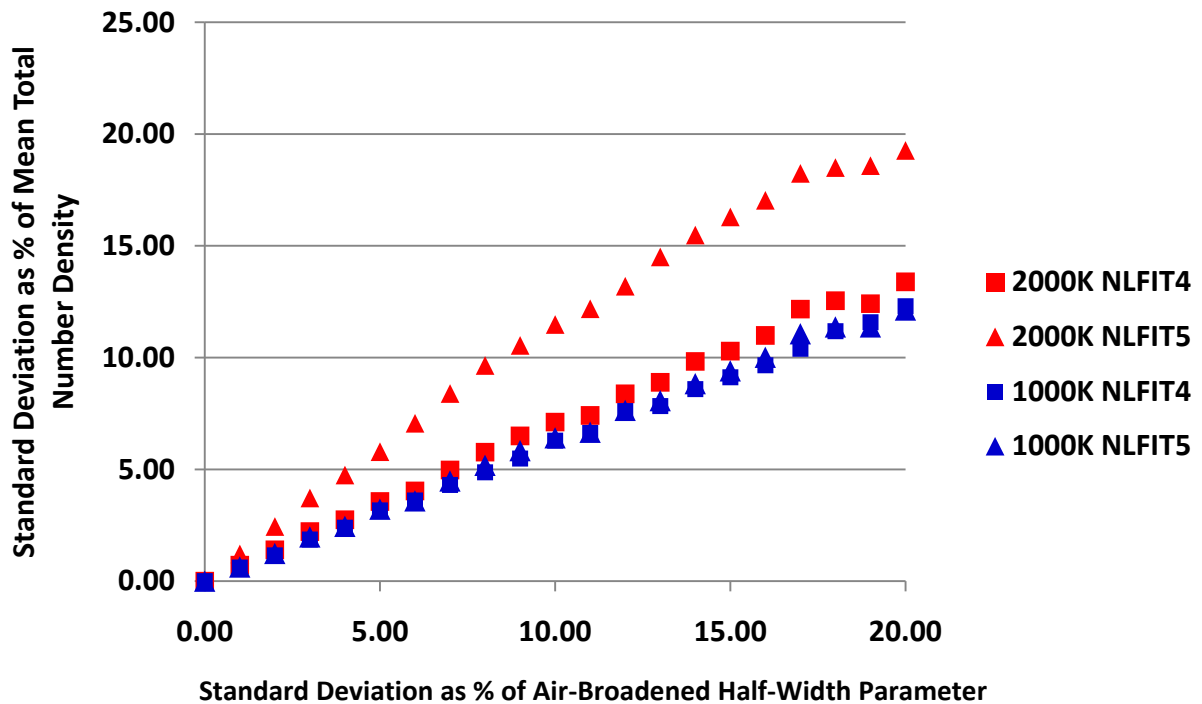


Figure 48. Uncertainty in Total Number Densities for Cases 2 and 3 (1,000 K and 2,000 K) vs. Uncertainty in the Air Pressure Broadening Parameter

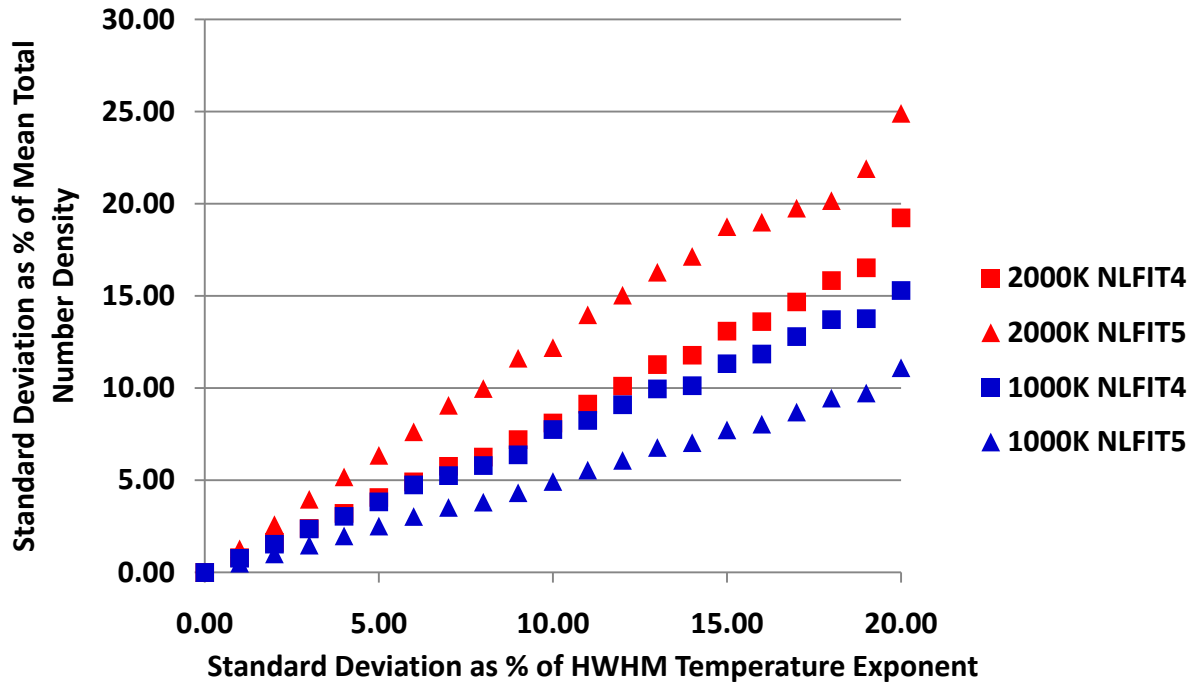


Figure 49. Uncertainty in Total Number Densities for Cases 2 and 3 (1,000 K and 2,000 K) vs. Uncertainty in the Air Pressure Broadening Parameter Temperature Correction Exponent

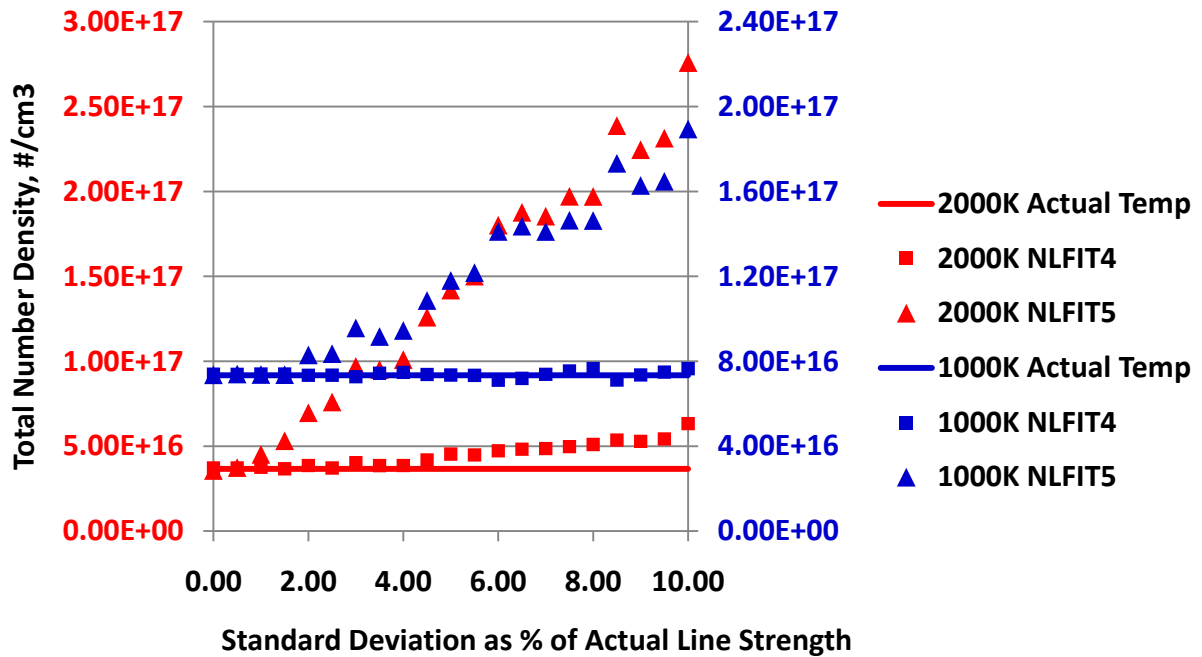
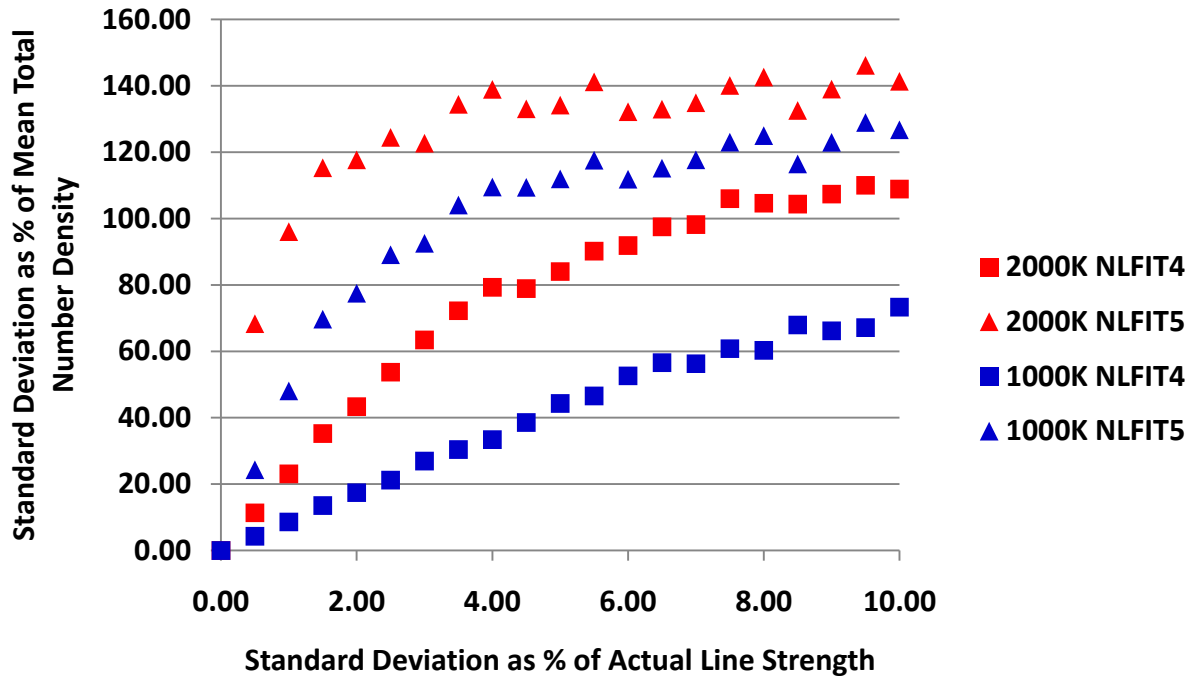


Figure 50. Actual and Retrieved Total Number Densities for Cases 2 and 3 (1,000 K and 2,000 K) vs. Uncertainty in Spectral Line Strength Parameter



**Figure 51. Uncertainty in Retrieved Total Number Densities for Cases 2 and 3 (1,000 K and 2,000 K) vs. Uncertainty in Spectral Line Strength Parameter**

The uncertainty associated with the mean background level and the detected laser intensity has a profound effect on Case 2 and 3 simulations due to the relatively weak absorbance levels. The integrated absorbance data reduction methods, LAINT and NLINT, failed at high noise or intensity uncertainty levels (low signal-to-noise ratios). Figures 52 and 53 show the actual and retrieved absorbing specie number densities vs. the uncertainty in the mean background level for Case 2 (1,000 K) and Case 3 (2,000 K). Note that for the higher temperature Case 3 the spread in retrieved absorbing specie number density is quite large in comparison to the lower temperature Case 2 results for those methods without a fitted background. This is due to the smaller absorbance levels for Case 3 in comparison to the variability in background vs. that of the lower temperature case. In Fig. 53 the integrated absorbance methods, LAINT and NLINT, produced erroneous results as many of the integrated absorbances were negative for the larger uncertainties in the mean background. As a result only the first 4 points are plotted for these methods in Fig. 53. Very good results were produced by those methods incorporating a background curve fit. The uncertainty plots in Figs. 54 and 55 show that the higher temperature (lower absorbance) Case 3 results possess a several fold increase in propagated uncertainty over the lower temperature Case 2 results. Again, this is driven by the lower absorbance levels. The effect of the mean background uncertainty on temperature and total number density was at a fraction of a percent level. This result is not surprising as the temperature and total number density for these test cases are primarily determined by spectral line shape and relative line absorption levels rather than constant shift in absorbance levels generated by an uncertainty in the mean background level.

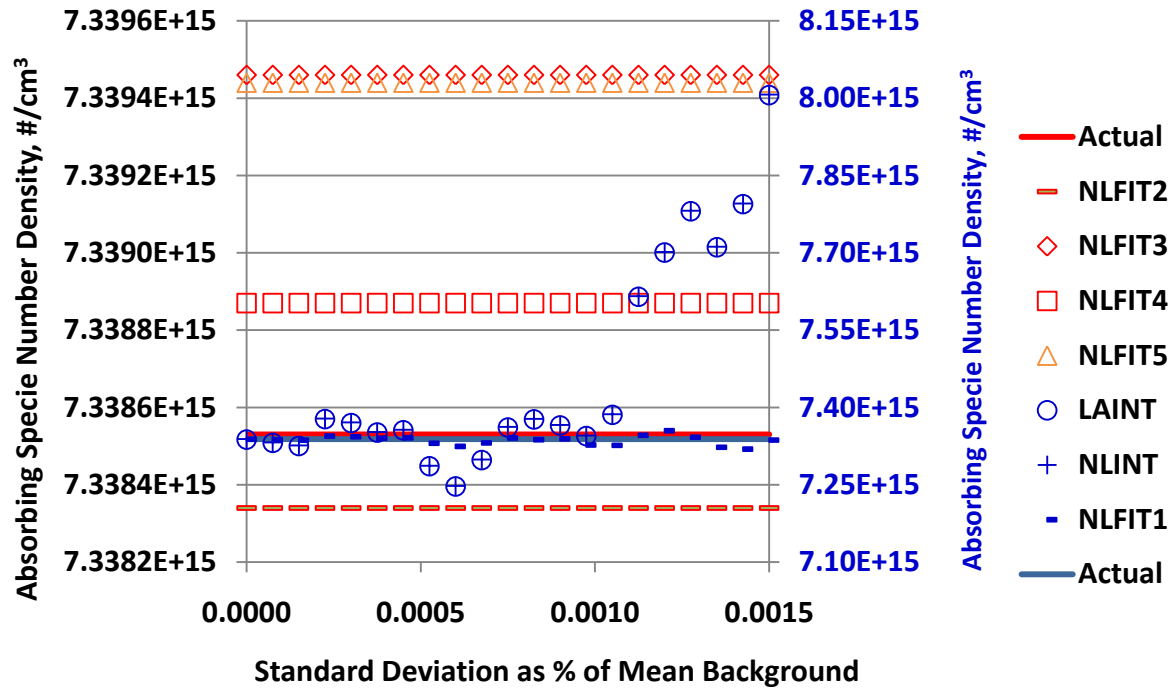


Figure 52. Actual and Retrieved Absorbing Specie Number Density for Case 2 (1,000 K) Conditions vs. Uncertainty in the Mean Background Intensity Level. Note the dark blue symbols in the plot use the right hand y-axis.

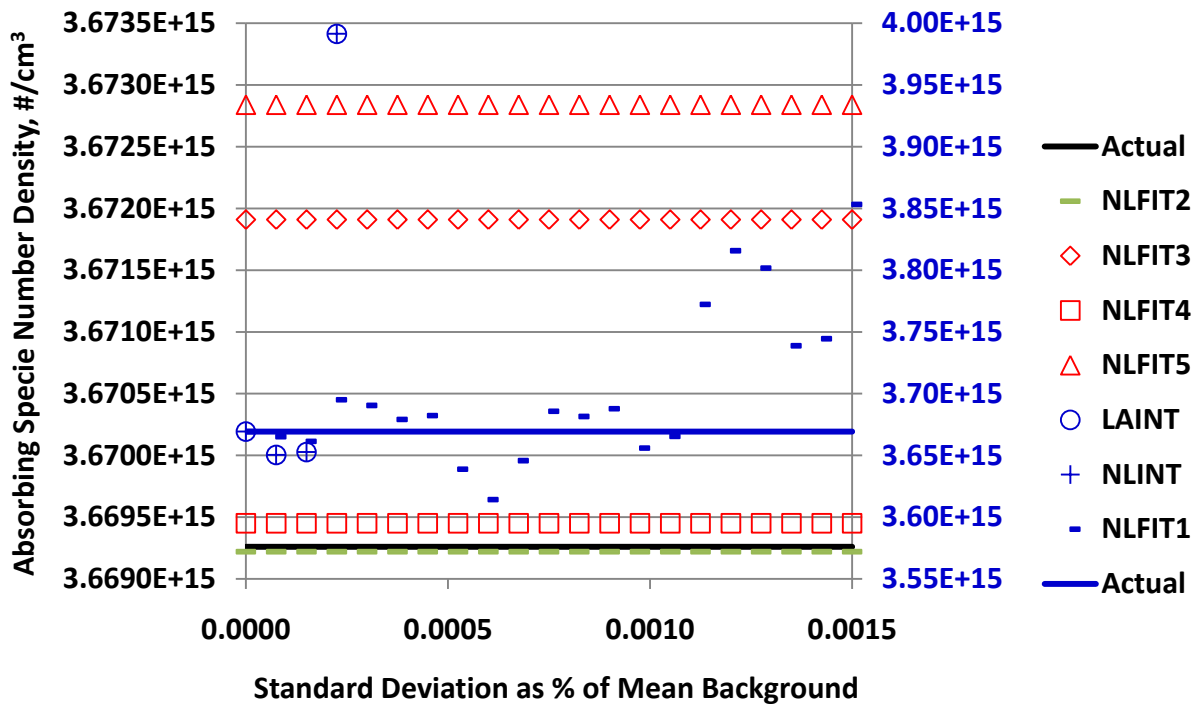


Figure 53. Actual and Retrieved Absorbing Specie Number Density for Case 3 (2,000 K) Conditions vs. Uncertainty in the Mean Background Intensity Level. Note the dark blue symbols in the plot use the right hand y-axis.

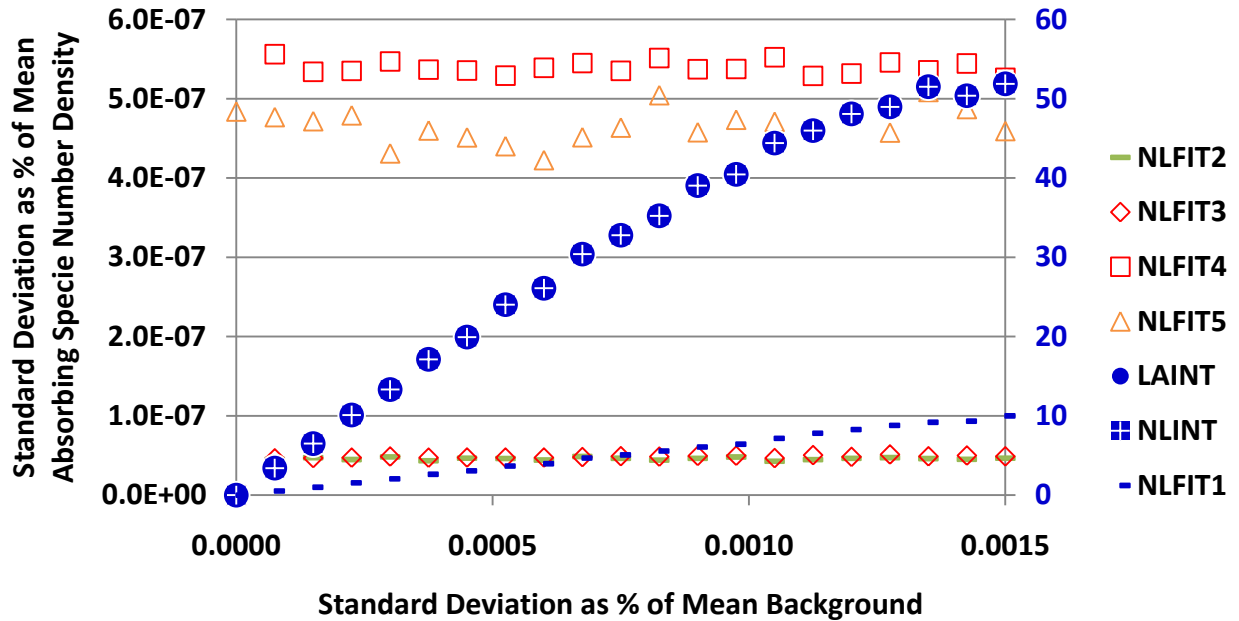


Figure 54. Uncertainty in Absorbing Specie Number Density for Case 2 (1,000 K) Conditions vs. Uncertainty in the Mean Background Intensity Level. Note the dark blue symbols in the plot use the right hand y-axis.

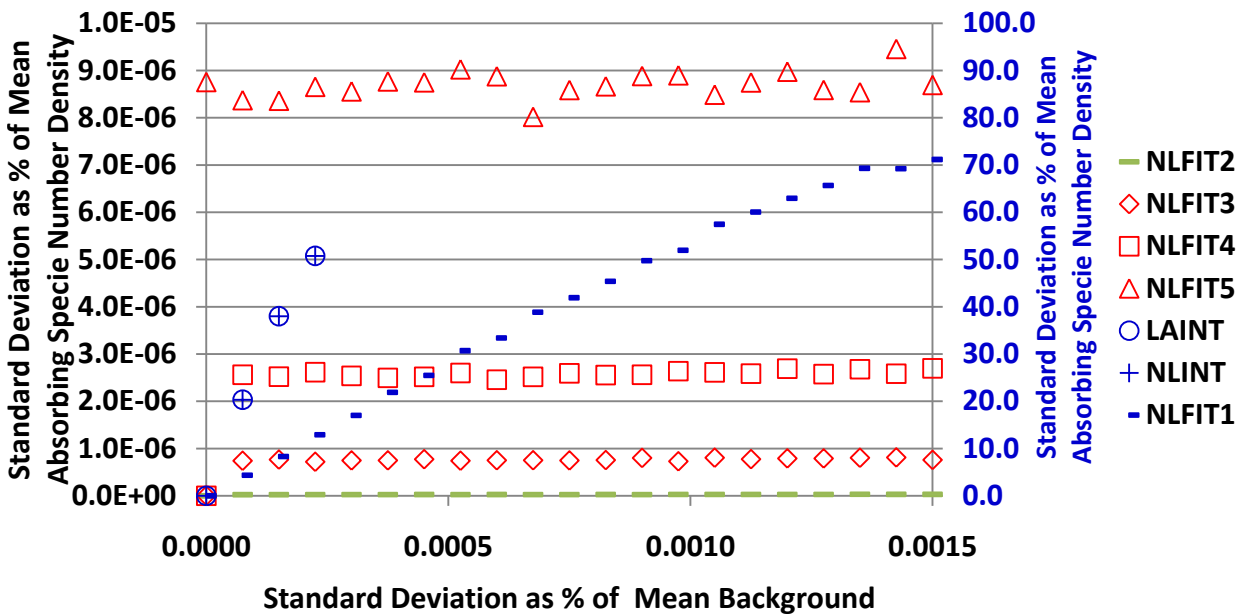
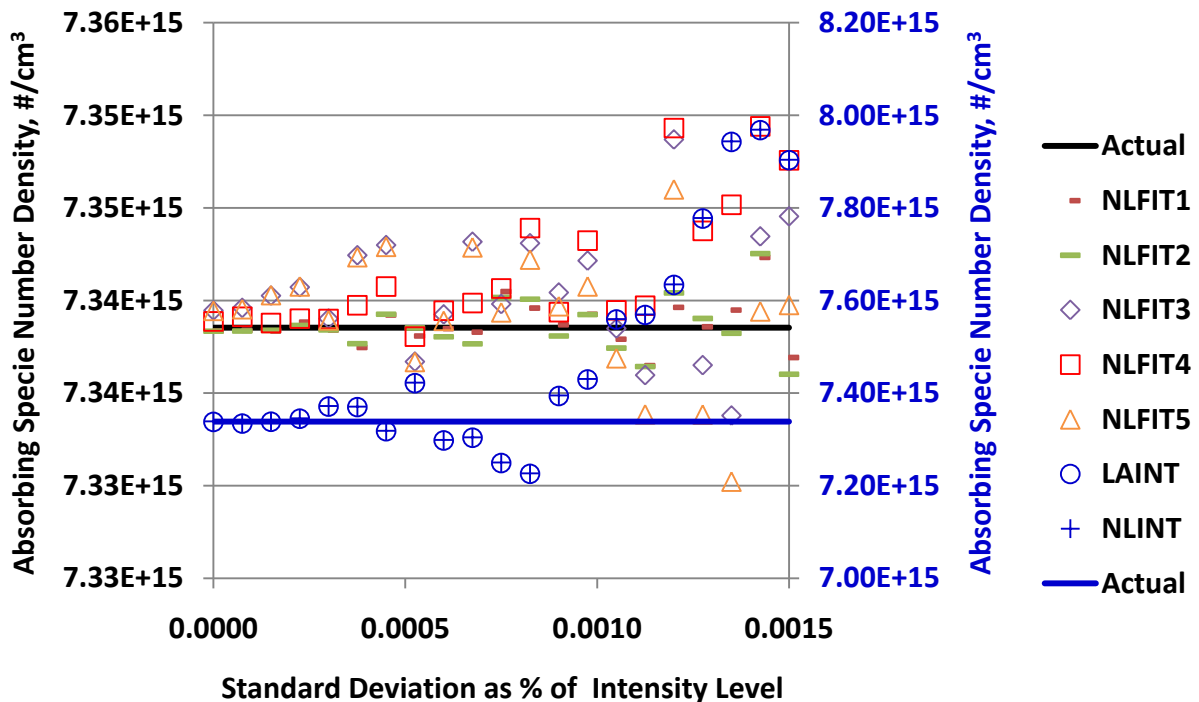


Figure 55. Uncertainty in Absorbing Specie Number Density for Case 3 (2,000 K) Conditions vs. Uncertainty in the Mean Background Intensity Level. Note the dark blue symbols in the plot use the right hand y-axis.

Uncertainty associated with noise of the detected laser intensity has a large impact on the retrieved quantities for these low absorbance cases. Figures 56 and 57 show the effect on absorbing specie number density due to the uncertainty in the intensity, or noise, level. Note that the x-axis extends to 0 to 0.0015% relative uncertainty. This is equivalent to a signal-to-noise ratio of infinity to 66666:1. The propagated uncertainty in absorbing specie number

density as a function of the uncertainty in laser intensity is shown in Figs. 58 and 59. Note that for the 2,000 K case (Case 3) only the first four points for the integrated absorbance methods are shown due to the failure of these methods at the high noise levels. A comparison of Figs. 58 and 59 shows that for the higher temperature Case 3 results, propagated uncertainties are drastically increased over the lower temperature Case 2 results. Again, this is due to the decreased absorbance levels. The uncertainty in the retrieved temperature is also greatly affected by the decreased absorbance levels of Case 3. Figure 60 shows the propagated uncertainty in temperature is slightly less than one order of magnitude greater for the higher temperature simulations than for the lower temperature case. The total number density is also affected by the decreased absorbance of the high-temperature cases as shown in Fig. 61 where the 2,000 K Case 3 has approximately a factor of two larger propagated uncertainties. Even for a very clean signal with a signal-to-noise ratio near 100,000:1 the potential uncertainty in the retrieved total number density is 10%. The size of the uncertainty likely precludes using weak absorption features at high temperatures and/or low pressures for ascertaining the total number density, hence pressure without appreciable signal averaging to improve the signal-to-noise ratio.

Owing to the exceptionally weak absorbance it is seen that the use of these particular sets of absorption features for exhaust gas diagnostics is problematic. Even with a generous 40-cm path length the uncertainty in absorbing specie number density, hence mass flux, is probably too sensitive to system noise to make it a viable choice for a “real world” application. However, examination of these particular transitions does shed some insight into the trade-offs of using weak absorption features for diagnostics.



**Figure 56. Actual and Retrieved Absorbing Specie Number Density for Case 2 (1,000 K) Conditions vs. Uncertainty in the Intensity Level. Note the dark blue symbols in the plot use the right-hand y-axis.**

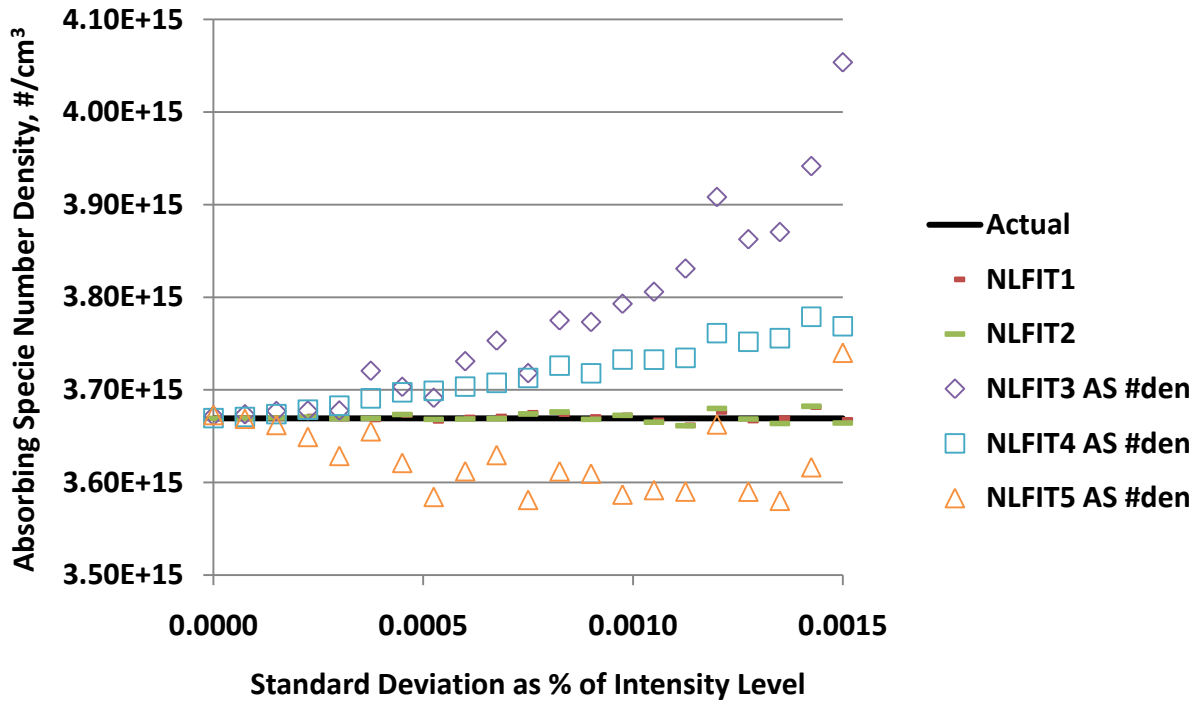


Figure 57. Actual and Retrieved Absorbing Specie Number Density for Case 3 (2,000 K) Conditions vs. Uncertainty in the Intensity Level. Note the dark blue symbols in the plot use the right-hand y-axis.

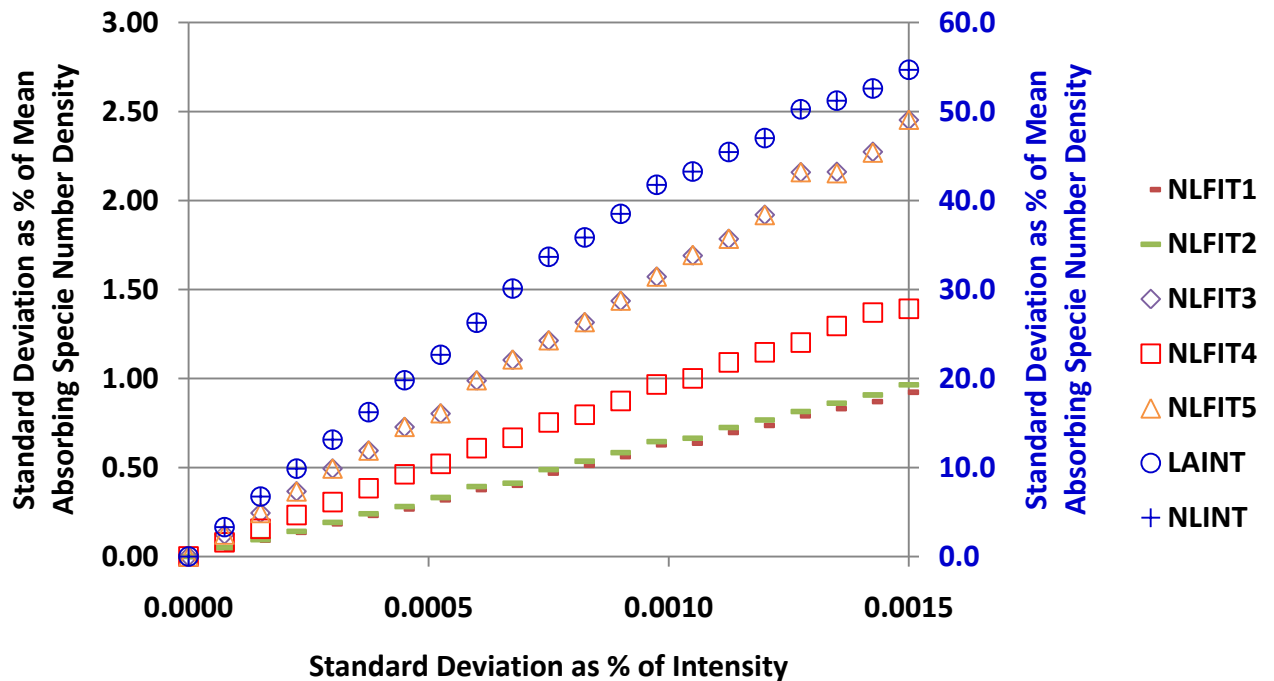


Figure 58. Uncertainty in Absorbing Specie Number Density vs. Uncertainty in the Intensity for Test Case 2 (1,000 K)

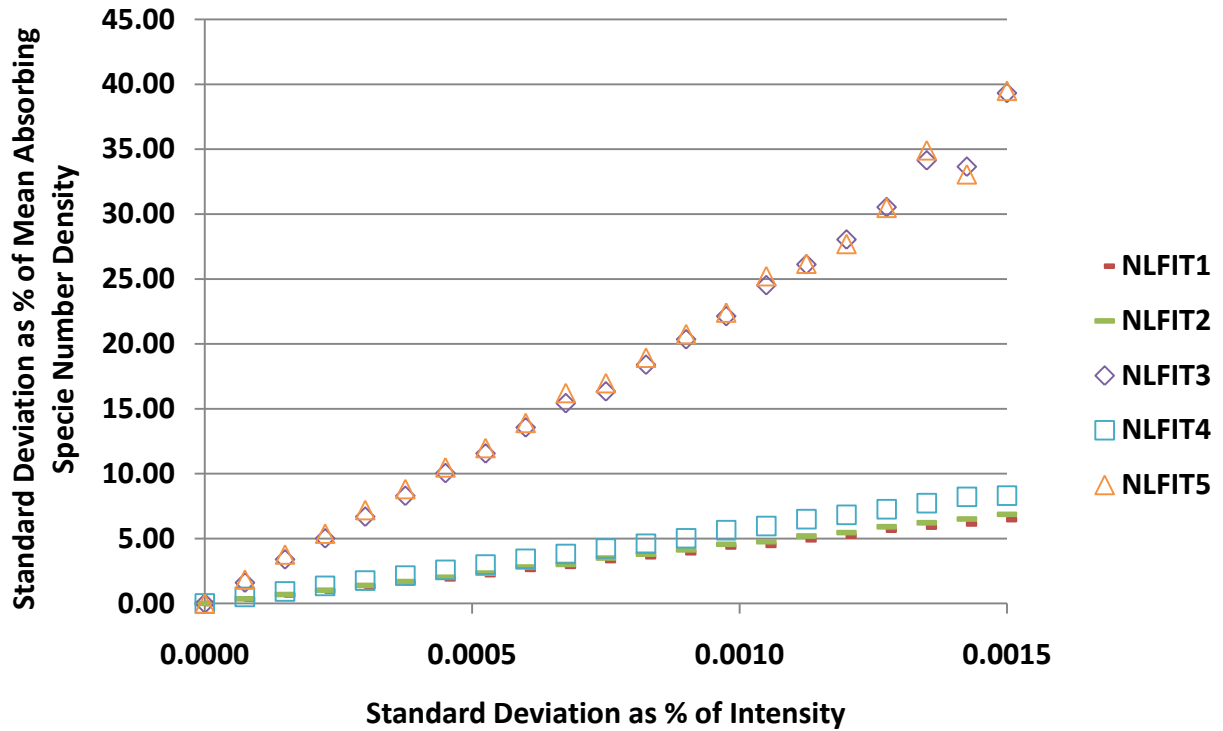


Figure 59. Uncertainty in Absorbing Specie Number Density vs. Uncertainty in the Intensity for Test Case 3 (2,000 K)

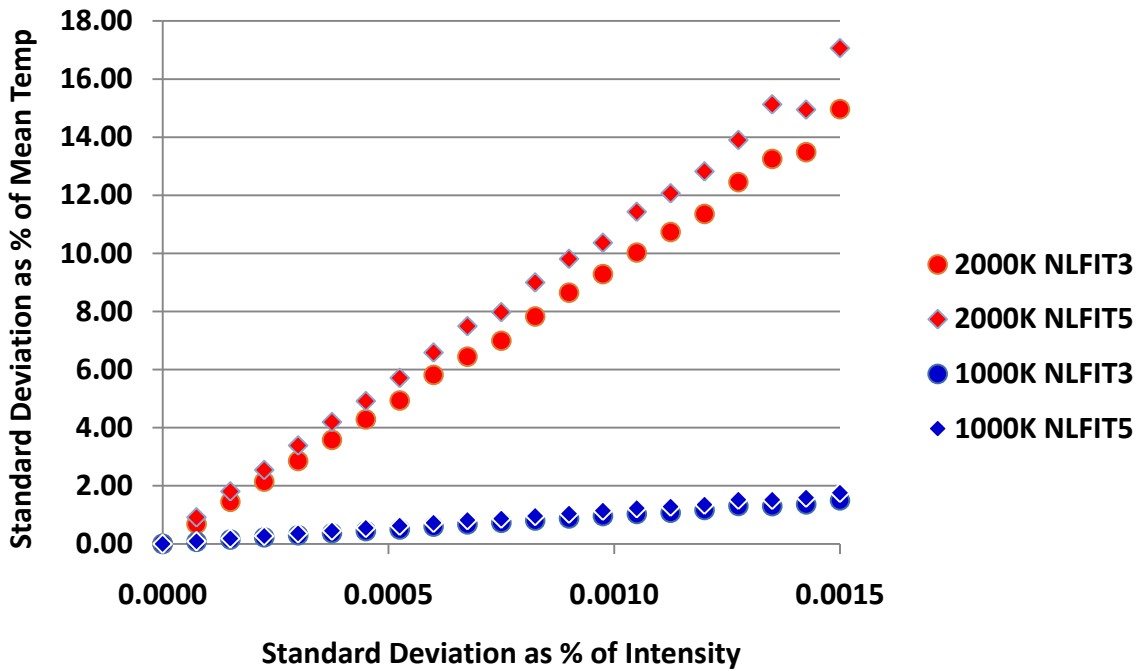
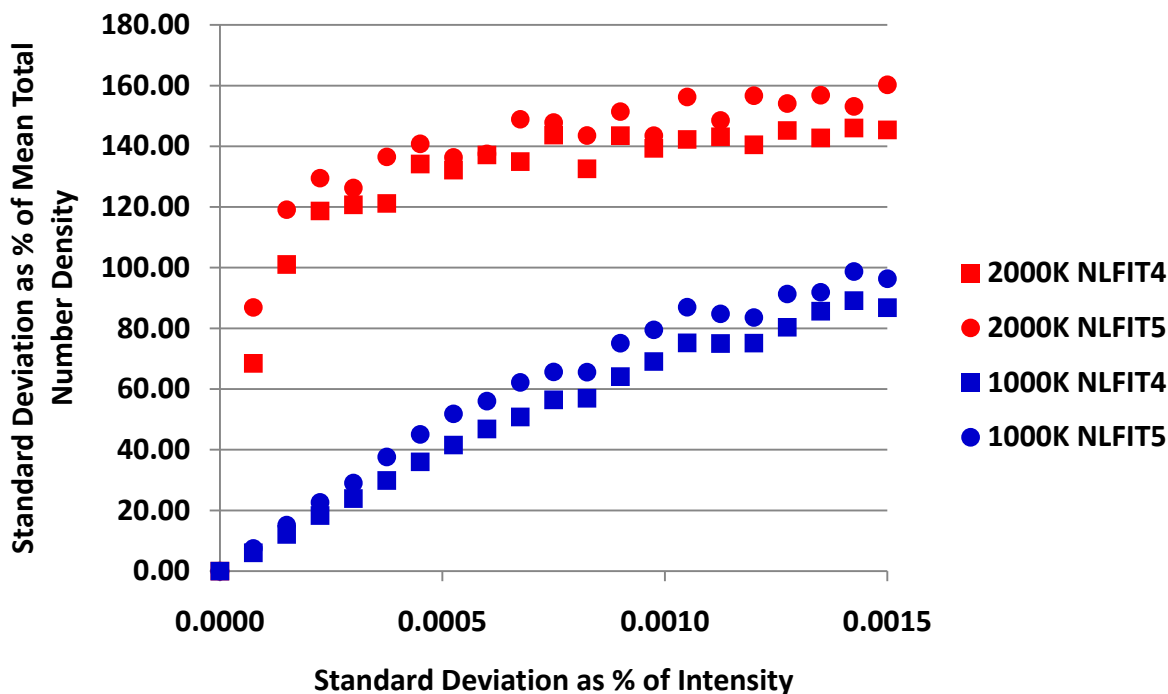


Figure 60. Uncertainty in Retrieved Temperature vs. Uncertainty in the Intensity Level for Case 2 (1,000 K) and Case 3 (2,000 K) Conditions



**Figure 61. Uncertainty in Retrieved Total Number Density vs. Uncertainty in the Intensity Level for Case 2 (1,000 K) and Case 3 (2,000 K) Conditions**

### 7.3 CASE 4: CO

Case 4 represents a scenario of strong absorption, multiple spectral lines, elevated temperatures, and low pressures. Here the target specie is carbon monoxide in the mid-infrared region. This type of data would be representative of measurements in support of combustion efficiency measurements in the exhaust of a scramjet or other very high-speed propulsion systems possibly utilizing a quantum cascade laser. The velocity and pressure are the same as in Cases 2 and 3, 1,500 m/sec and 0.01 atmospheres, respectively. The mole fraction of CO is assumed to be 1%. As can be seen from Fig. 10 the minimal fractional transmittance and peak absorbance for this case would be approximately 0.7 and 0.35, respectively. Note this is quite a departure from the previous cases where the fraction transmittance was greater than 0.99 or the absorbance was less than 0.01. This increased absorbance is indicative of what is achievable in the mid-infrared spectral region where the absorption cross section for most infrared active gases increases drastically over what is available in the near infrared.

The strong absorption features of CO make the retrieved velocity relatively insensitive to noise of the second-derivative spectral noise. Figures 62 and 63 show the results obtained from the Monte Carlo simulation. Note that compared to the previous Case 2 and 3 results the initial error in velocity is higher for the Case 4 mid-infrared conditions. This is due to several factors including nearness of the peak spectra feature to one of the sample points, the difference in optical frequencies of the observations, and the range of spectral data. The velocity induced Doppler shift scales with the optical frequency of the observation as given in Eq. (18). Cases 2 and 3 were simulated H<sub>2</sub>O observations near 10,500 cm<sup>-1</sup>, whereas the Case 4 simulated observations are at approximately 2150 cm<sup>-1</sup>. In addition, the Case 2 and 3 spectral calculations covered a 2-cm<sup>-1</sup> spectral region, whereas the Case 4 conditions cover a 1-cm<sup>-1</sup> spectral region. However, with 4,000 points in the second-derivative spectrum, the uncertainty

in the velocity does not change over the range of uncertainty in the intensity level or signal-to-noise ratio. However, over this same range of uncertainty or noise on the second-derivative spectrum, the Case 2 and 3 conditions indicated an increasing uncertainty in the velocity. The difference in behavior is due to the increased absorption for the CO feature of Case 4 vs. that of Cases 2 and 3.

The effects of uncertainty of the line strength parameter on the retrieved absorbing specie number density are shown in Figs. 64 through 66. Note in Figs. 64 and 65 that the LAINT method has substantially more uncertainty than the other methods, including the other integrated absorbance method NLINT, at retrieving the absorbing specie number density even at low line strength uncertainty levels. This was not observed in the previous test cases. This is due to the large increase in absorbance levels for the current case resulting in the failure of the linear absorbance approximation given in Eq. (20). Note that the same linear relationship of uncertainty in line strength to uncertainty in absorbing specie number density exists as was illustrated in the previous test cases. Also note from Fig. 66 that the methods incorporating the total number density as a fit parameter gave poorer retrievals than other methods. This same behavior was observed in Test Cases 2 and 3, which also employed multiple spectral line curve fitting. The cause for this, addressed in the Case 2 and 3 discussions, is the small pressure-broadening component at these high temperatures and low pressures.

Uncertainties in parameters affecting the pressure-broadening line width had little impact on the retrieved absorbing specie number density. As with Test Cases 2 and 3, the effects of the air-broadened line width parameter on retrieved absorbing specie number density was a few tenths of a percent with a 20% variation in the air-broadening parameter. As with the previous test cases the uncertainty in mass flux is driven primarily by the uncertainty in the absorbing specie number density. This is easily observed by comparing, uncertainty in mass flux in Fig. 67 and uncertainty in absorbing specie number density in Fig. 66.

Temperature determination for the two-spectral-line Test Case 4 exhibits similar dependencies as the multiple-spectral-line Test Cases 2 and 3. Figures 68 through 70 show the retrieved temperature, the error, and the uncertainty as a function of the uncertainty in the line strength. Note that the uncertainty in temperature varies almost linearly with uncertainty in line strengths as was observed with the multiple-spectral-line Test Cases 2 and 3. However, the error is significantly less for the current Test Case 4 than with the previous test cases. This is attributable to the stronger absorbance of the CO transitions in Test Case 4 than in Test Cases 2 and 3, and possibly because Lowry and Fisher deliberately chose this specific pair of transitions for their temperature sensitivity at elevated temperatures. The uncertainty in the retrieved temperature was relatively independent of the uncertainty in the parameters affecting the pressure-broadened half-width. The air- and self-broadened half-width parameters, as well as the temperature correction exponent, only resulted in a few tenths of a percent uncertainty in temperature even when the half-width parameters had uncertainties as high as 20%. This is due to the small value of the pressure broadening at these high-temperature and low-pressure conditions.

Total number density, and hence the pressure, was greatly impacted by uncertainty in the line strengths and the pressure-broadening-related parameters as illustrated in the plots of Figs. 71 through 73 and Figs. 74 and 75, respectively. Figures 71 through 73 show that both methods that retrieve total number density have a significant propagated uncertainty due to the line strength and that method NLFIT4 carries an approximately four-fold increase in error and uncertainty over method NLFIT5. Method NLFIT5 has temperature as a fit parameter whereas NLFIT4 does not. The line-to-line deviations in the line strength are compensated for in the

nonlinear fitting by adjusting temperature. This adjustment has two effects. First, it produces an uncertainty in the temperature retrieval with increasing uncertainty in the line strength (see Fig. 70). Second, the adjusted temperature changes the line-broadening parameters which in turn affect the total number density as it adjusts to compensate for the broadening parameter. This strong dependency of the uncertainty in the total number density, hence pressure, with the pressure-broadening parameters is verified by examining Figs. 74 and 75. Both, the pressure-broadening parameter and its temperature adjustment exponent propagate an approximate one-for-one uncertainty to the total number density. Note, as with the low-pressure H<sub>2</sub>O absorption Test Cases 2 and 3, it is highly impractical to retrieve an accurate total number density or pressure from the spectral data with any reasonable uncertainty without obtaining equally accurate values for the pressure-broadening parameters.

Uncertainty in the optical spectral background level and mean background level were seen to be significant sources of uncertainty in the retrieved parameters associated with Cases 2 and 3. However, due to the overall increased absorption of the CO spectral lines of this case, the role of noise, or baseline shift for the mean background, is less important. Figures 76 and 77 show the actual and retrieved absorbing specie number density and the uncertainty in the absorbing specie number density vs. uncertainty in the mean background level. Note that when comparing Fig. 55 and the 2,000 K water spectral absorption Test Case 3 to Fig. 73 (CO at 2,000 K), one sees an overall improvement in the propagated uncertainties. This is particularly evident when one considers the difference in the uncertainty scales of these two plots. This disparity is due to the increased absorption amount in Test Case 4 (CO). As with previous test cases, the uncertainty in the mean background has a dramatic effect on those methods that do not incorporate a background curve fit (i.e., LAINT, NLINT, and NLFIT1). The effect of intensity uncertainty, or noise, has a slight impact on the absorbing specie number density. Figure 78 illustrates that the effect of noise is in the subpercent level for those methods not employing integrated absorbances. However, for the integrated absorbance base methods, LAINT and NLINT, the propagated uncertainty in absorbing specie number density is several percent. Methods NLFIT3 and NLFIT5, which retrieve temperature, propagated a slight uncertainty due to noise as shown in Fig. 79. A signal-to-noise ratio of 10,000:1 or 0.01% uncertainty in the measured intensity produced only an approximately 0.25% uncertainty in the temperature. However, the effect of intensity noise on the uncertainty in the total number density, or resulting pressure, as shown in Fig. 80 had a large dependency. This is typical of the low-pressure/high-temperature scenarios examined here and is attributable to the small pressure-broadened half-widths.

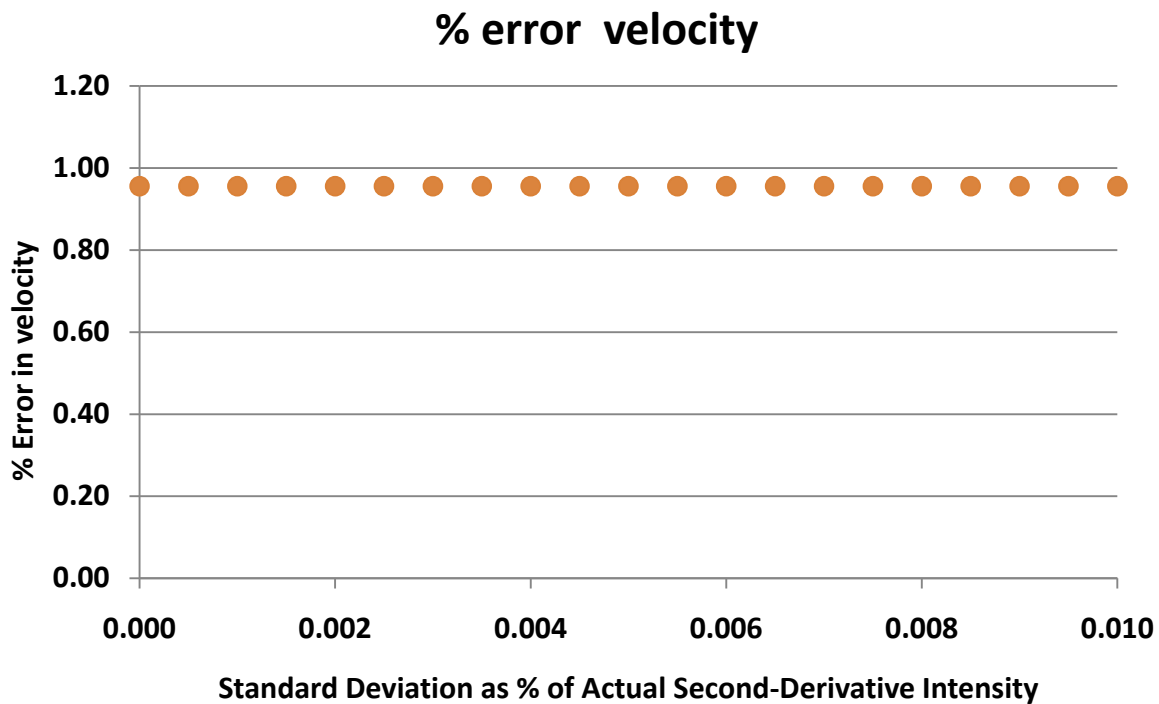


Figure 62. Error in Retrieved Velocity a Function of Uncertainty in the Second-Derivative Spectral Intensity for Case 4. Note this represents a signal-to-noise going from infinity to 10,000:1.

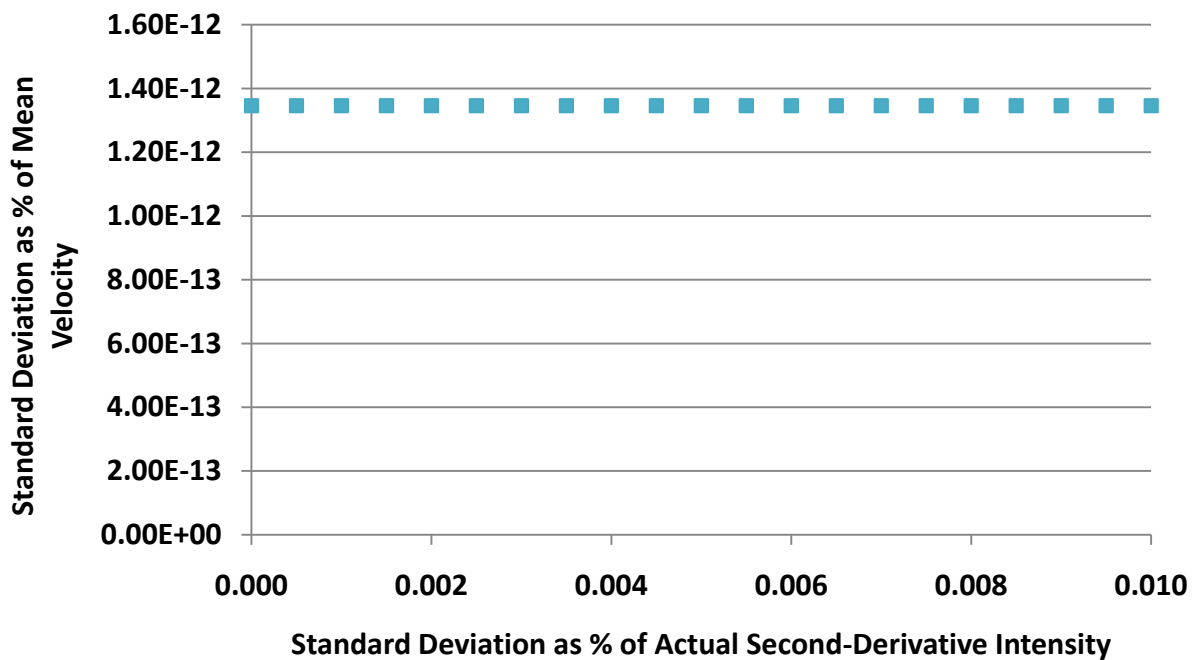


Figure 63. Uncertainty in Retrieved Velocity a Function of Uncertainty in the Second-Derivative Spectral Intensity for Case 4. Note this represents a signal-to-noise going from infinity to 10,000:1.

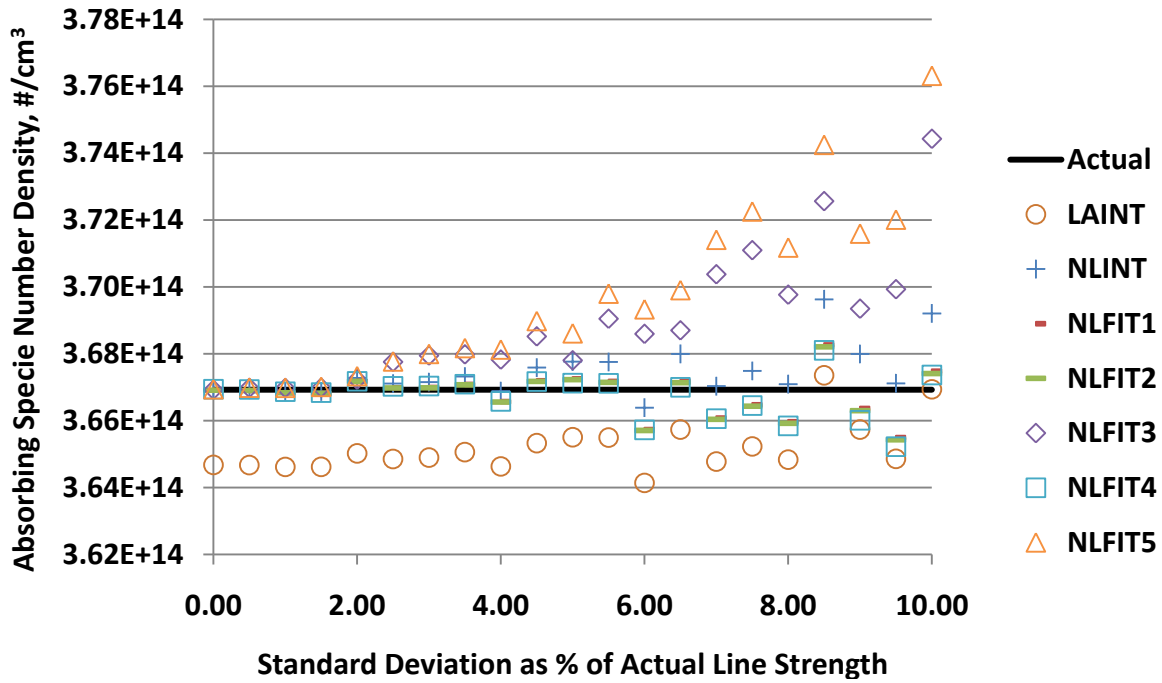


Figure 64. Retrieved Absorbing Specie Number Density vs. Uncertainty in Line Strength for CO Absorption Case 4 Condition at 2,000 K

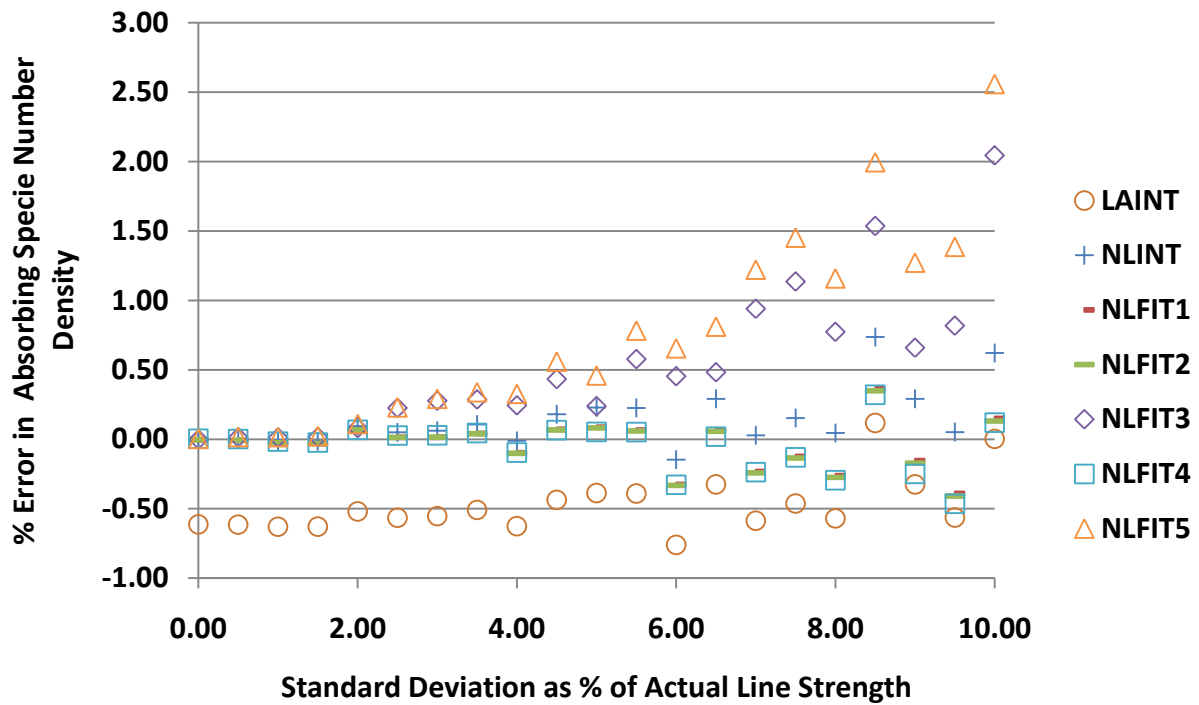


Figure 65. Retrieved Absorbing Specie Number Density Error vs. Uncertainty in Line Strength for CO Absorption Case 4 Condition at 2,000 K

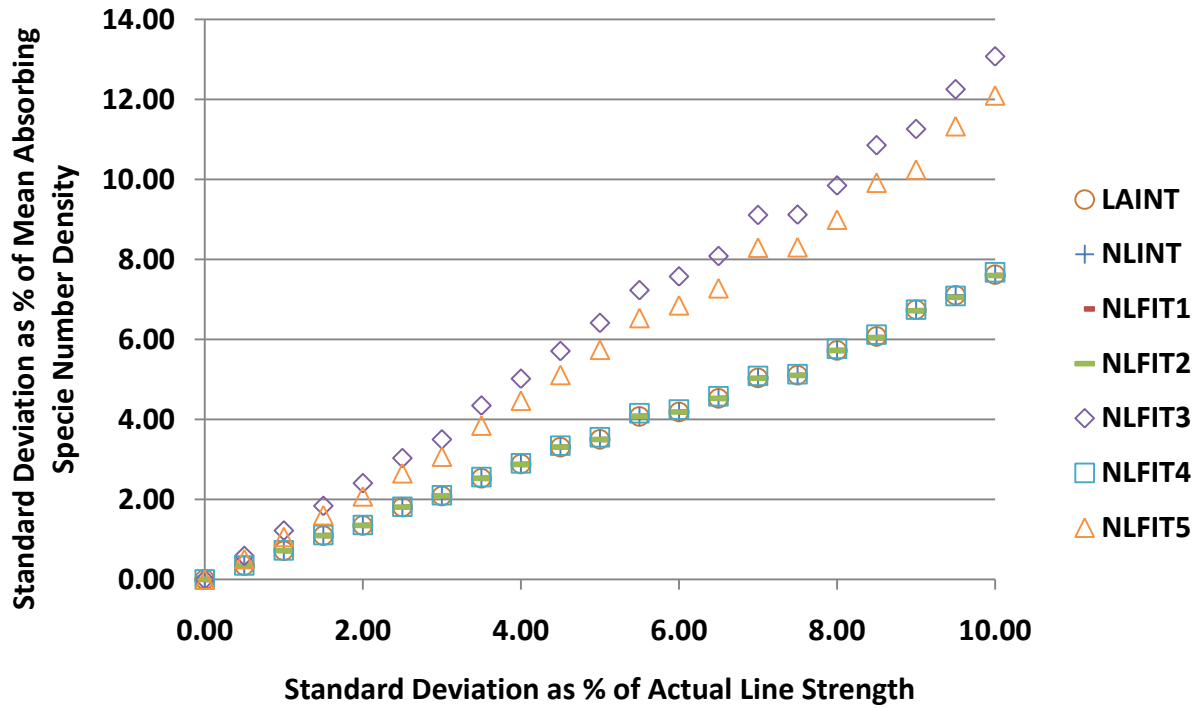


Figure 66. Uncertainty in Retrieved Absorbing Specie Number Density Error vs. Uncertainty in Line Strength for the CO Absorption Case 4 Condition at 2,000 K

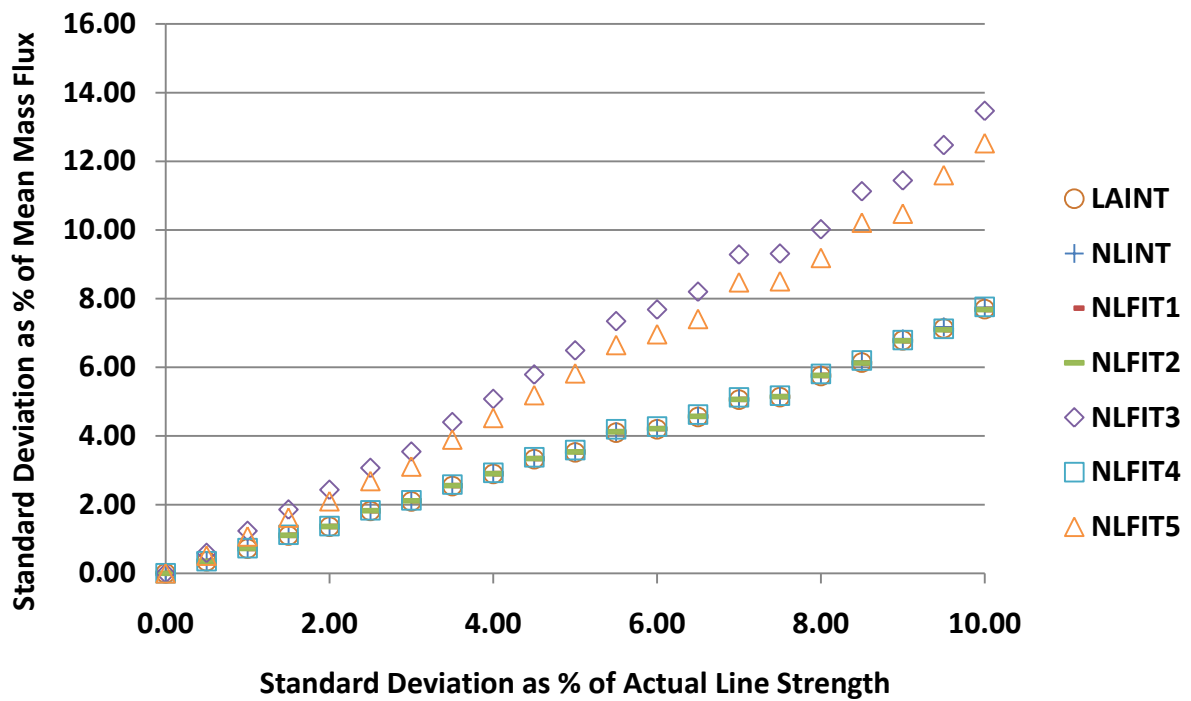


Figure 67. Uncertainty in Mass Flux for Test Case 4 (CO, 2,000 K) Conditions vs. Uncertainty in the Line Strength

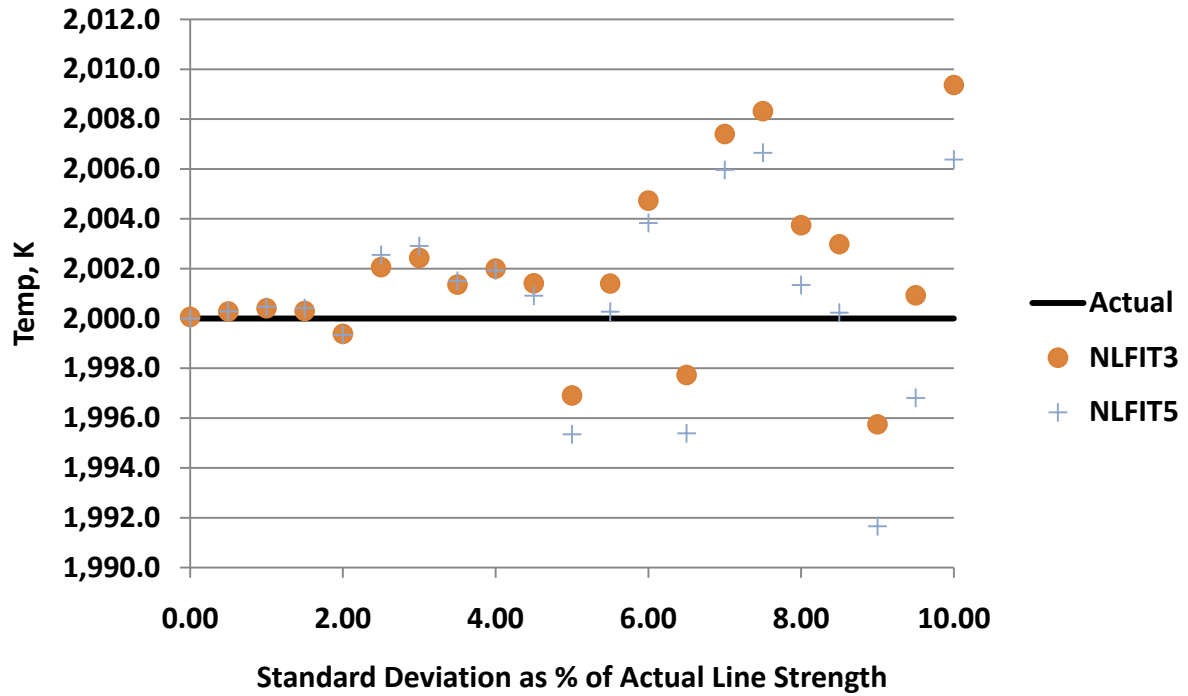


Figure 68. Actual and Retrieved Temperature for Case 4 (CO, 2,000 K) Conditions vs. Uncertainty in Line Strengths

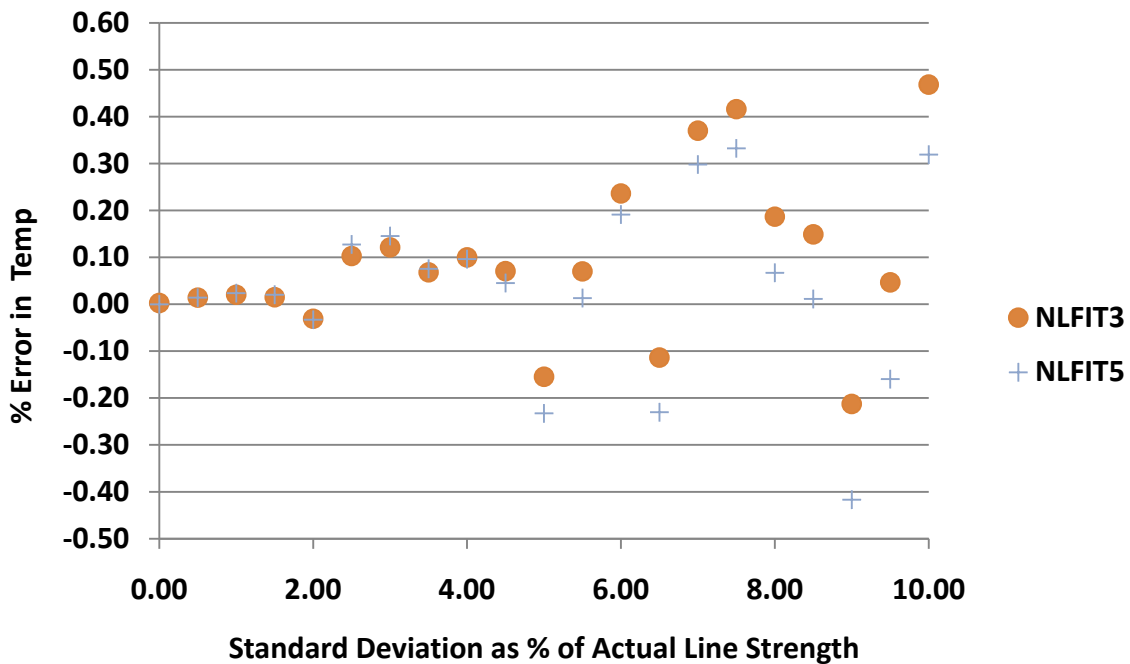


Figure 69. Error in Average Retrieved Temperatures for Case 4 (CO, 2,000 K) and Conditions vs. Uncertainty in Line Strengths

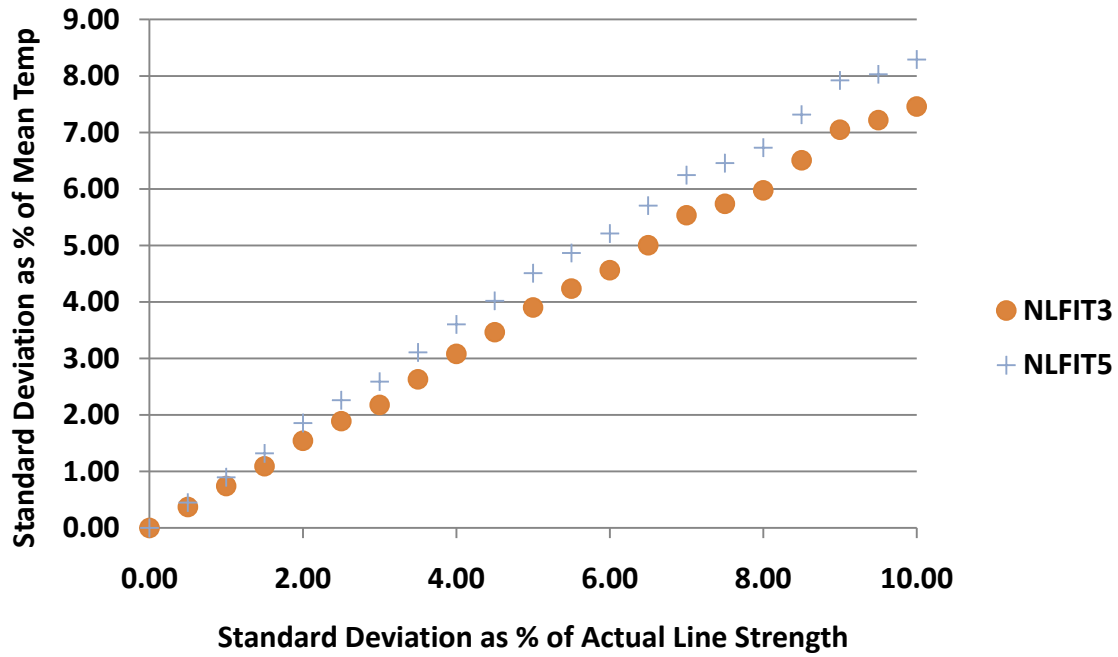


Figure 70. Uncertainty in Retrieved Temperature for Case 4 (CO 2,000 K) Conditions vs. Uncertainty in Line Strength

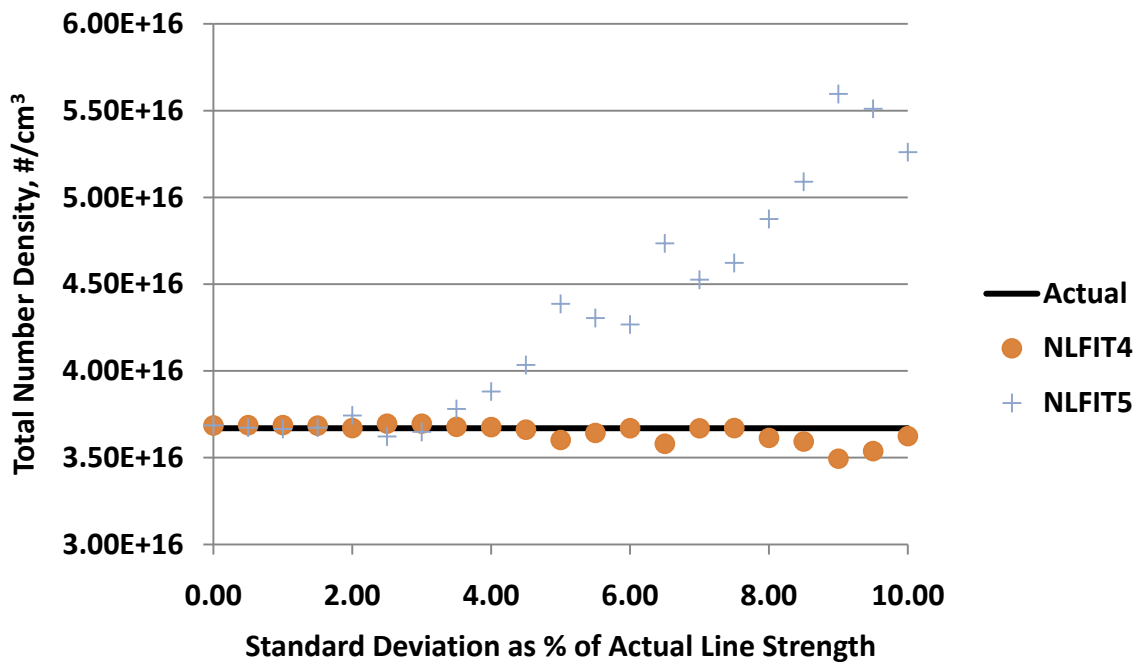


Figure 71. Actual and Retrieved Total Number Density for Test Case 4 (CO, 2,000 K) Conditions vs. Uncertainty in Line Strength

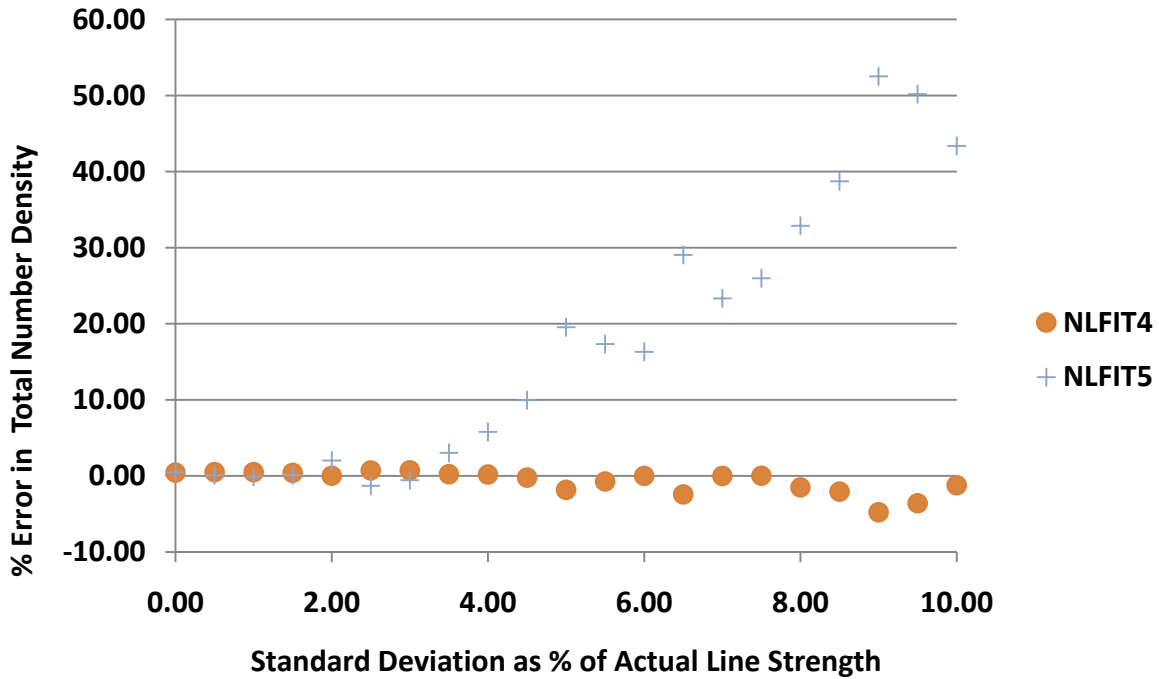


Figure 72. Error in Mean Total Number Density for Test Case 4 (CO, 2,000 K) Conditions vs. Uncertainty in Line Strength

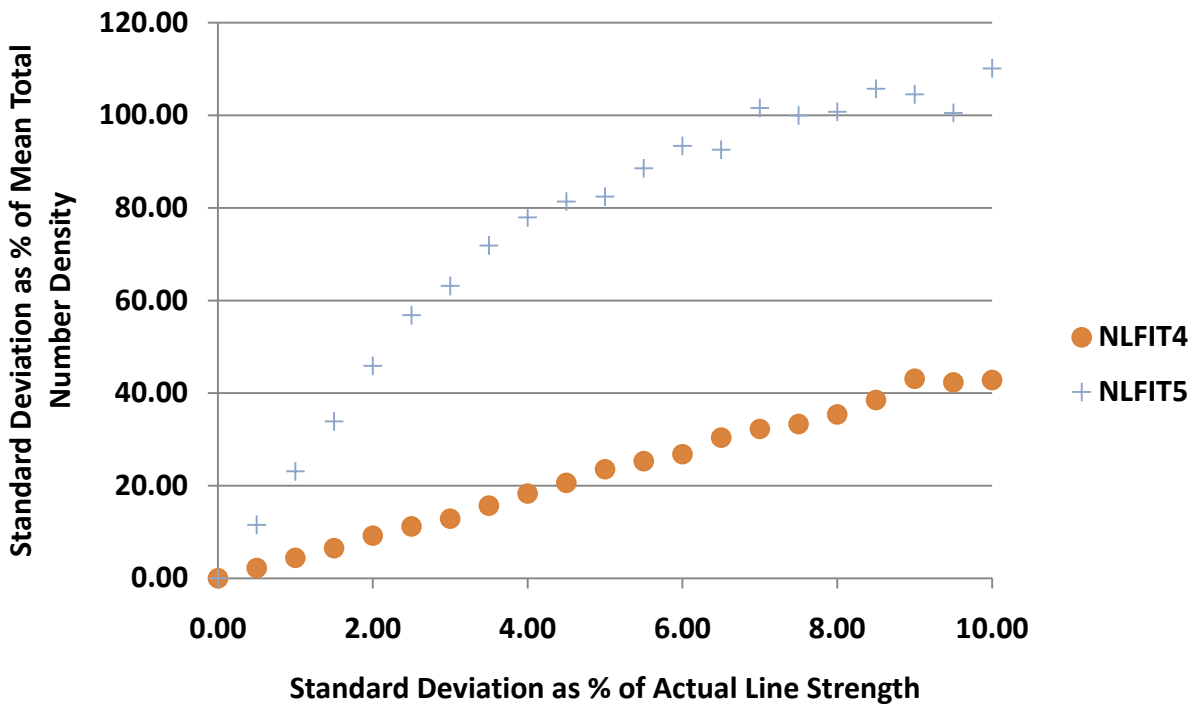


Figure 73. Uncertainty in Total Number Density for Test Case 4 (CO, 2,000 K) Conditions vs. Uncertainty in Line Strength

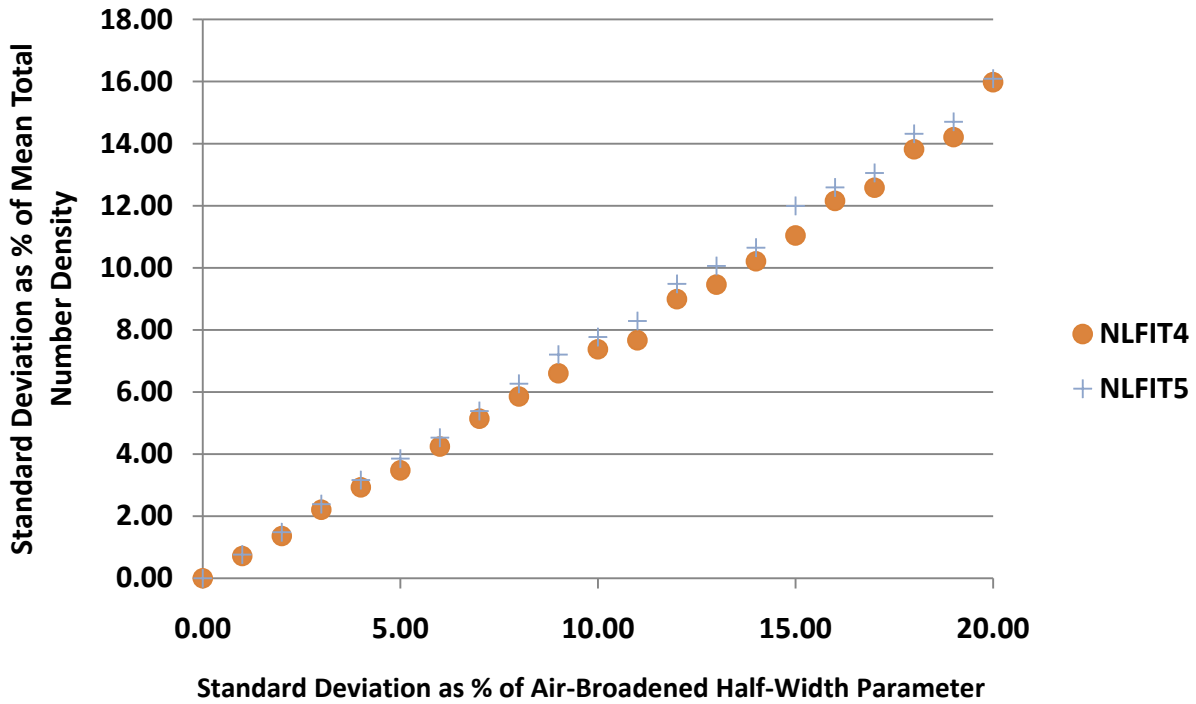


Figure 74. Uncertainty in Total Number Density for Test Case 4 (CO, 2,000 K) Conditions vs. Uncertainty in Air-Broadening Parameter

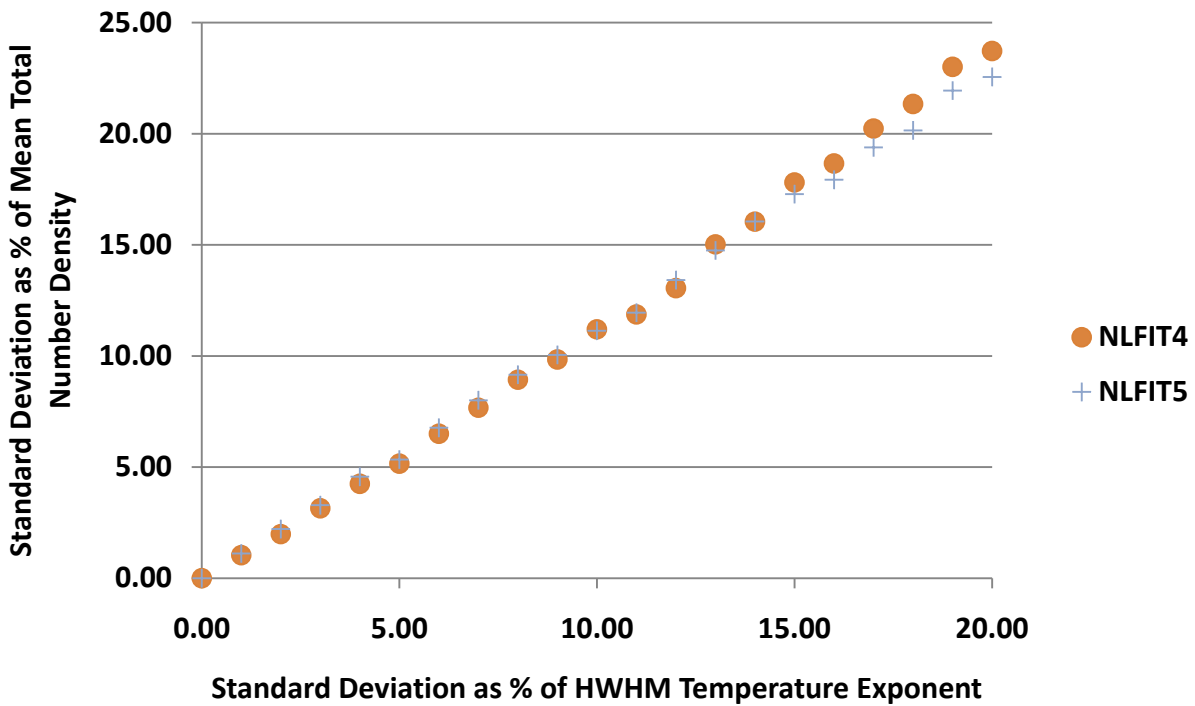


Figure 75. Uncertainty in Total Number Density for Test Case 4 (CO, 2,000 K) Conditions vs. Uncertainty in Pressure-Broadening Temperature Correction Exponent

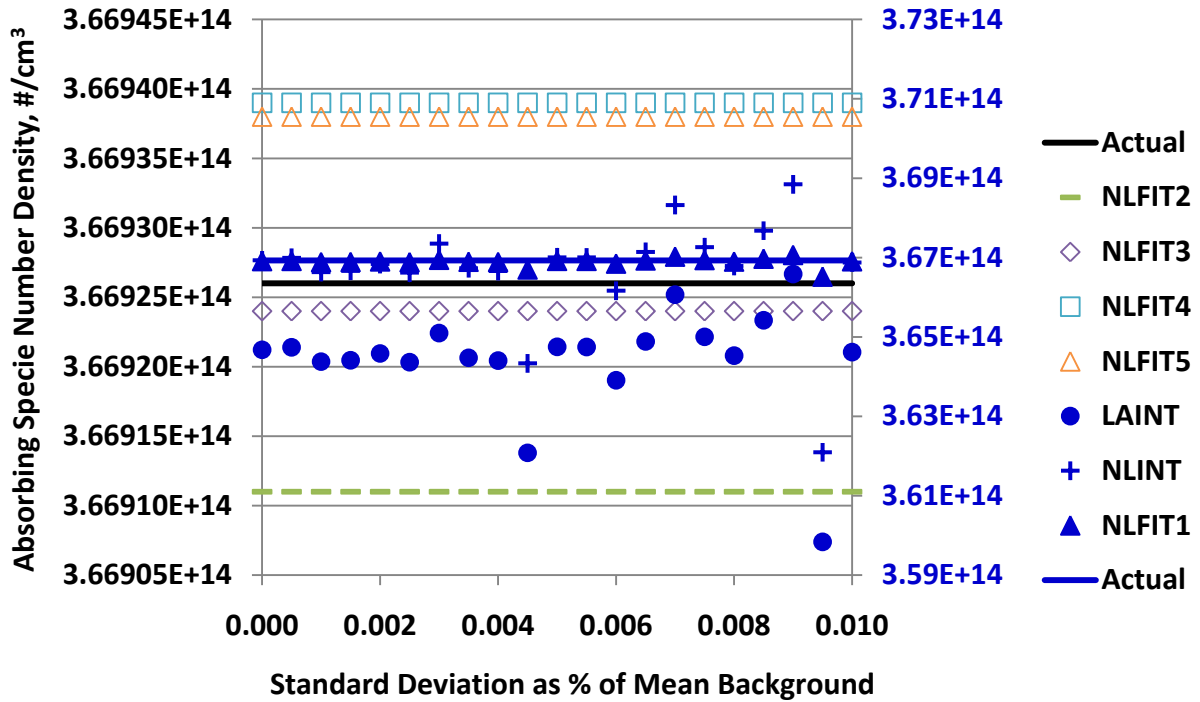


Figure 76. Absorbing Specie Number Density for Test Case 4 (CO, 2,000 K) Conditions vs. Uncertainty in Mean Background Level. Lines and symbols in dark blue are associated with the right y-axis.

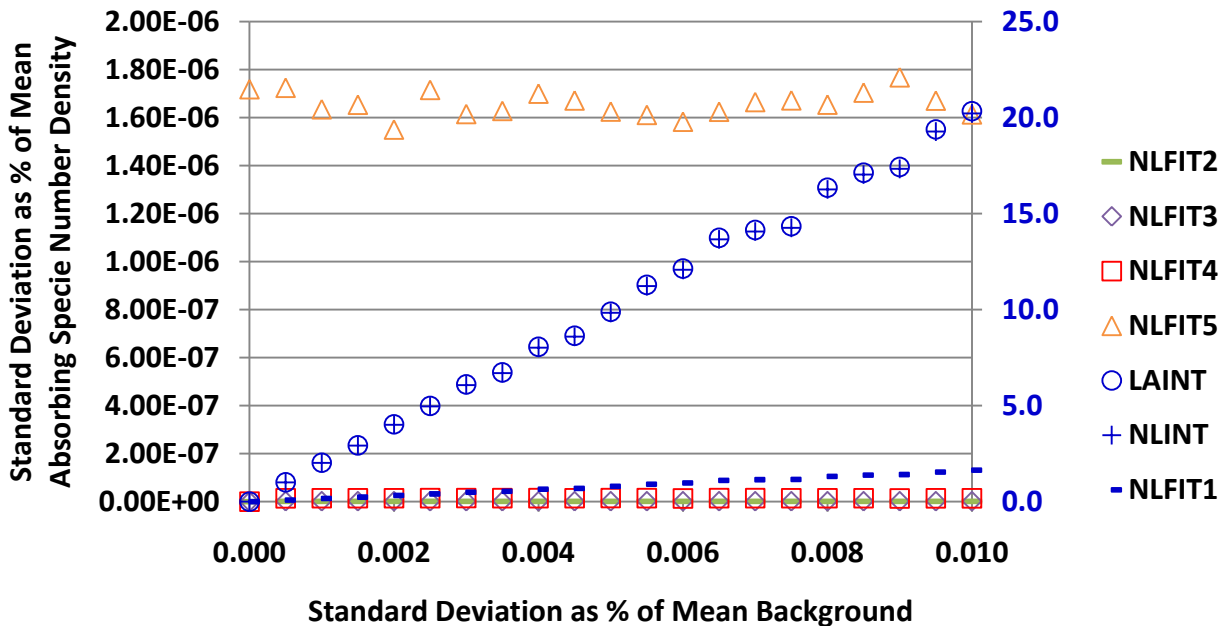


Figure 77. Uncertainty in Absorbing Specie Number Density for Test Case 4 (CO, 2,000 K) Conditions vs. Uncertainty in Mean Background Level. Lines and symbols in dark blue are associated with the right y-axis.

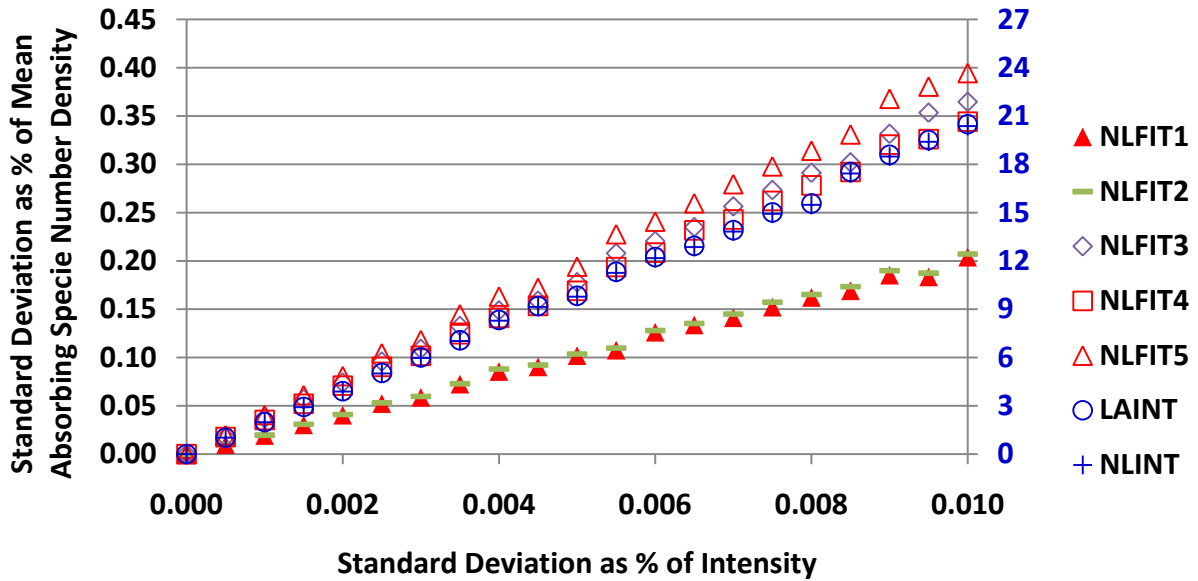


Figure 78. Uncertainty in Absorbing Specie Number Density for Test Case 4 (CO, 2,000 K) Conditions vs. Uncertainty in Mean Background Level. Lines and symbols in dark blue are associated with the right y-axis.

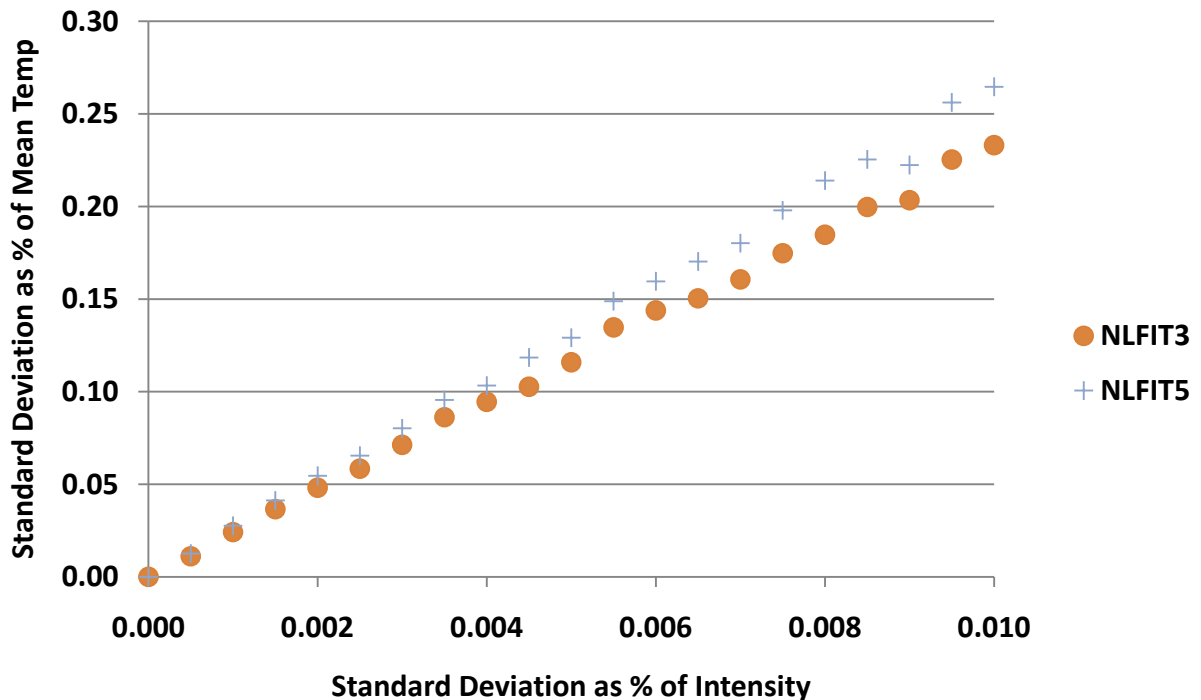
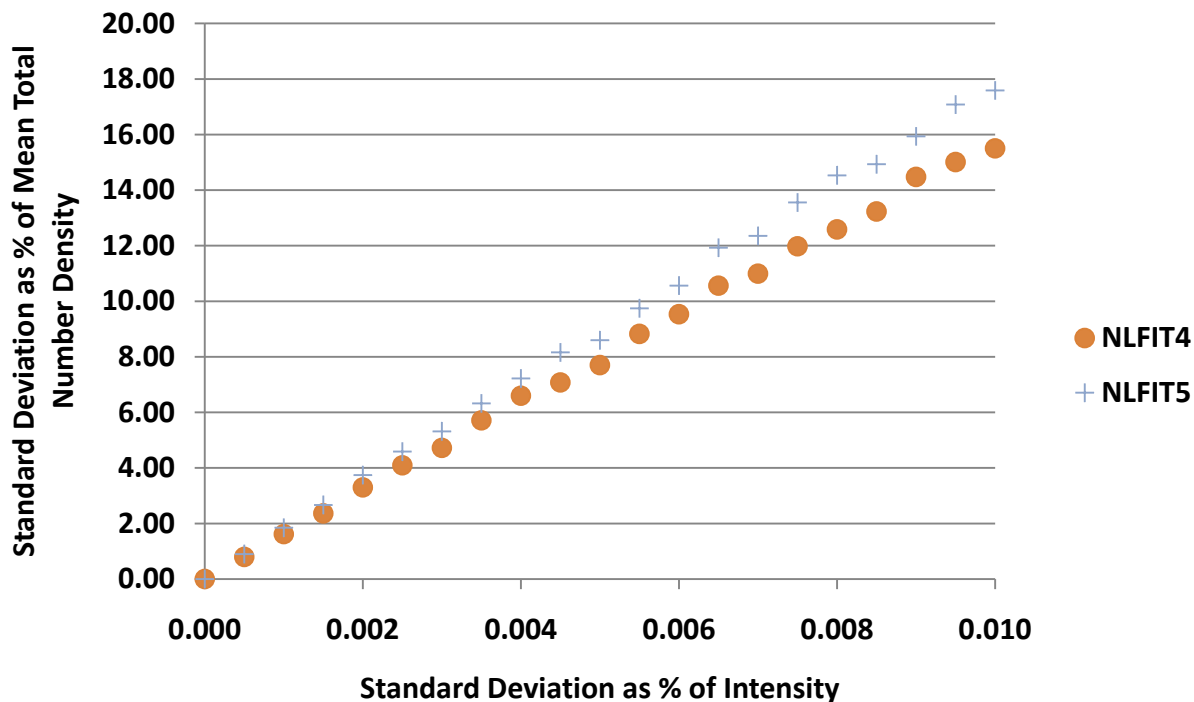


Figure 79. Uncertainty in Retrieved Temperature for Test Case 4 (CO, 2,000 K) Conditions vs. Uncertainty in the Spectrum



**Figure 80. Uncertainty in Retrieved Total Number Density for Test Case 4 (CO, 2,000 K) Conditions vs. Uncertainty in the Spectrum**

## 8.0 CONCLUSION

A Monte Carlo uncertainty analysis of some typical TDL data reduction methods has provided insight into those molecular spectral or instrumentation parameters affecting accuracy of retrieved gas properties. Two major parameters found to be pivotal are intensity noise and spectral line strength. It was determined that stronger absorbance lessened the dependency of the retrieved absorbing specie number density uncertainty on intensity noise. However, it should be stated that all the cases considered did not possess very strong absorption nearing saturation conditions. Even with a generous path length of 40 cm it is very difficult to obtain percent level uncertainty in absorbing specie number density by measuring weak absorbing spectral features. It was found that utilizing a background fit parameter in the data reduction method was universally preferable. Data reduction methods relying on integrated measured absorbance spectra are applicable only under a restricted set of conditions. These include narrow spectral features in comparison to the spectral scan region, a sufficiently large number of samples to ensure accuracy in the numerical integration, and incorporation of an integrated line wing correction.

Uncertainty associated with the absorbing specie number density and mass flux is a strong function of the uncertainty in the measured intensity (i.e., signal-to-noise), the spectral line strength uncertainties, and the absorbance levels. As addressed above, selection of target species and absorption features that provide strong absorption characteristics is important. Most high-speed test and evaluation ground-test, and particularly flight-test, applications have severe constraints on the optical path length available. Therefore the only remaining method for achieving stronger absorption is through the selection of absorption features with larger optical cross sections. The advent of the quantum cascade laser will hopefully provide routine access to the mid-infrared spectral region where most infrared active gases have a much larger optical

cross section. Uncertainty in retrieved absorbing specie number density was found to be approximately equal to that of the line strength parameters utilized in the analysis. Unfortunately, at this time the bulk of the spectral line parameters in the merged HITRAN/HITEMP database have approximately a 20% uncertainty. Therefore, careful selection and/or measurement of the spectral line(s) employed in the measurement should be undertaken. A key parameter affecting all retrieved parameters is measured intensity noise. This parameter can be minimized by careful examination of data acquisition techniques, the use of averaging scans where possible, and the use of more powerful laser systems.

Temperature determination from absorption spectra has been applied to nonintrusive measurements for many years. However, based on this study the uncertainty in the retrieved temperature is heavily driven by several factors. For a single spectral line the temperature uncertainty dependence is affected by those parameters affecting the spectral line width parameters, such as the pressure-broadening parameter and its temperature correction exponent. As seen from the statistics of the merged HITRAN/HITEMP database, the uncertainty in these parameters for the bulk of the spectral lines is on the order of 20%. However, it should be noted that through a meticulous survey of the database and literature it is possible to select spectral lines with better individual accuracy in the spectral line parameters. The Monte Carlo analysis performed in this work suggests, for a single spectral line at near-ambient conditions, that the uncertainty in the retrieved temperature is approximately equal to that of the uncertainty in the pressure-broadening parameter. The situation is different when employing two or more spectral lines that have been judiciously chosen for their temperature sensitivity. The key parameter that controls the uncertainty in temperature retrieval in this case is the spectral line strength. The analysis of the uncertainty statistics of the merged HITRAN/HITEMP database indicated that the uncertainty in the line strength for the bulk of the spectral lines is in the 10 to 20% range. Specifically, for the two specific mid-infrared CO spectral lines of Test Case 4 (temperature: 2000K, pressure: 0.01 atmosphere, 1% CO) the Monte Carlo analysis indicated an approximate 10 to 20% uncertainty in temperature. Again, this number can be greatly improved by the proper selection and/or measurement of the spectral lines to improve the accuracy in the parameters that drive the uncertainty.

Low uncertainty total number density, or pressure, is the most difficult to retrieve from absorption measurements. As one approaches atmospheric pressures, the uncertainty dependence of the retrieved total number density was shown, for the specific single O<sub>2</sub> absorption line (Test Case 1), to depend approximately linearly with the uncertainty of the pressure-broadening parameter. Unfortunately, this spectral line parameter is typically one of the less well-quantified parameters in the spectral databases. At low pressures and/or high temperatures the uncertainty in the retrieved total number density grows due to the lessened dependence of the spectral line shape or pressure broadened line width. This would suggest that at the high-temperature and low-pressure conditions experienced in high-speed propulsion testing, the retrieval of low uncertainty total number density or pressure from an absorption measurement may be problematic at this time.

Mass flux uncertainty was driven almost totally by the uncertainty in the absorbing specie number density. In this study the mass flux was determined by a linear function involving the product of the absorbing specie number density and the velocity. The velocity was determined from the second-derivative transmitted intensity spectrum by means of wavelength modulated spectroscopy. Owing to the high signal-to-noise ratio obtainable using WMS, the velocity could be obtained with low uncertainty, even with the simplistic peak-picking technique implemented in this work. It was found that a key issue in obtaining accurate velocities is to utilize a sufficient

number of second-derivative spectral points. This has also been observed by Galyen and Plemmons through experimental wind tunnel measurements.

The Monte Carlo technique for analysis of uncertainty was found to be highly valuable. It provides a robust test for the data reduction method or algorithm under consideration by testing it under a whole range of anticipated data and/or input parameters. Application of this technique makes it relatively easy to test the “as used” data reduction algorithm and does not require analytical or numerical evaluation of partial derivatives. The biggest drawback is the computational time required. It is necessary to perform repeated calculations through many cycles to ensure statistical viability of the analysis. It should be noted that the main purpose of this work was to ascertain the key functional dependencies of various input parameters that drive the uncertainties of retrieved gas properties. The Monte Carlo technique was invaluable in obtaining that information. However, the Monte Carlo technique can easily be adapted to provide actual uncertainties based on experimentally determined uncertainties of a combination of input parameters. Since this would not require looping through various magnitudes of parameters under consideration or a separate analysis for each individual parameter, it would be computationally more efficient than the analysis performed in this survey study.

## 9.0 RECOMENDATIONS

Several “lessons learned” obtained through the execution of this study have provided insight into those areas requiring additional attention and key helpful comments for those that may be considering the use of Monte Carlo uncertainty analysis. Listed below in bullet form are some recommendations and notes:

- Debugging a Monte Carlo analysis computer code is difficult due to the intrinsic random nature of the technique. As a result it is highly recommended that investigators in the early stages of their code development write all intermediate calculated quantities to an unformatted or binary file for each cycle. Then, it is relatively quick and easy to go back and pick up the calculations on the offending condition without repeating the entire set of calculations.
- Parallelizing the Monte Carlo analysis code to take advantage of multiple processor computers would reduce execution time.
- A systematic investigation into instrument related sources of noise should be conducted as a mean of identifying potential sources of noise and minimizing those sources. This should culminate with verification in a relevant test environment.
- The selection of absorption features to utilize in an absorption measurement should be carefully chosen. Many issues must be considered. However, to minimize the uncertainty in the retrieved gas properties, key things to consider are strength of absorption and accuracy of those spectral parameters utilized in the analysis. This step may require following the source of the database parameters back to their origin to determine their specific uncertainties.
- A comprehensive improvement in spectral line parameter accuracy through experimental measurement and verification at precisely controlled, specifically elevated temperature, conditions is required to make the merged HITRAN/HITEMP spectral database more viable for elevated temperature applications.

- The effects of other line shape profiles such as the Dicke or Rautian spectral line profiles should be investigated.
- The addition of other sources of uncertainty such as digitization bit resolution (dynamic range), nonuniform flow field, 0% transmittance baseline shift, and nonconstant laser intensity effects should be investigated.
- Spectral database listings should be expanded to include pressure broadening parameters due to combustion byproduct gases found in high concentrations such as H<sub>2</sub>O and CO<sub>2</sub>.

## 10.0 SUMMARY

A Monte Carlo-based uncertainty propagation analysis was performed on simulated high spectral resolution absorption data to ascertain those key input parameters that most effect uncertainty of retrieved properties of the gas path in question. A systematic study of uncertainty propagation through several typical data reduction methods employed in the analysis of high-resolution spectra, typical of that obtained from tunable diode laser absorption measurements, was investigated using four different test cases. Seven different data reduction methods were incorporated to test the strengths and weaknesses of each. The merged HITRAN/HITEMP spectral database was examined, and a distribution of the quoted uncertainties of spectral parameters for the two most common combustion byproduct gases, H<sub>2</sub>O and CO<sub>2</sub>, was obtained. This information was used in conjunction with the Monte Carlo uncertainty propagation analysis to determine the state of propagated uncertainties based on currently available spectral data.

The four specific test cases examined were chosen based on previous use by researchers in the field and their wide range of conditions. Included was a single O<sub>2</sub> absorption line measurement at near-ambient temperature and 0.5 atmosphere pressure which possessed a relatively weak absorption feature in the near infrared. Two additional cases were high-temperature, 1,000 K and 2,000 K, low-pressure (0.01-atm) H<sub>2</sub>O absorption spectra consisting of 12 absorption lines, which represented a very weak absorption feature in a high temperature low pressure environment with little pressure-broadening contribution. These test cases are extensions of applicability, based on some recent measurements, to an environment one may expect in a high-speed propulsion test facility. The fourth, and last, test case consisted of two CO spectral lines in the mid-infrared at high-temperature (2,000 K) and low-pressure (0.01-atm) conditions. This case was chosen for its previous applications to high-temperature diagnostics and its much stronger absorption features in the mid-infrared spectral range accessible to quantum cascade lasers. This test case would be representative of a measurement one would conduct to obtain data for quantification of combustion efficiency in a high-speed facility or engine exhaust flow.

The Monte Carlo analysis method and associated computer code has applicability as a standard against which other more computationally efficient, albeit approximate, uncertainty analysis algorithms can be benchmarked. The Monte Carlo analysis for the test cases presented indicated an almost one-to-one relationship between the uncertainty in the line strength parameter and propagated uncertainty in the absorbing specie number density. The viability of retrieving precise total number density, or pressure, from high resolution absorption spectra is strongly dependent on the test conditions. Low-pressure and/or high-temperature test environments result in extremely high propagated uncertainties in the total number density due

to uncertainty in the spectral line parameters affecting the pressure-broadened spectral linewidths. Specifically, the pressure-broadening parameter and the pressure-broadening temperature correction exponent. Noise in the intensity measurement is a universal source of uncertainty and was found to be particularly detrimental for low absorbance spectral measurements.

A set of recommendations for further investigations, hints for potential users of a Monte Carlo analysis, and recommendation for improvement in high-resolution or tunable diode laser-based absorption measurements is presented. Chief among the recommendations is obtaining improved accuracy in spectral line parameters and the investigation of improved instrumentation and data acquisition methodologies to improve signal-to-noise ratios.

## REFERENCES

1. Chang, L., Jeffries, J., and Hanson, R. "Mass Flux Sensing via Tunable Diode Laser Absorption of Water Vapor." AIAA-2010-303 ,48th AIAA Aerospace Sciences Meeting Including the New Horizons Forum and Aerospace Exposition, Orlando, FL, 4-7 Jan 2010.
2. Bryner, E., et al. "Tunable Diode Laser Absorption Technique Development for Determination of Spatially Resolved Water Concentration and Temperature." AIAA-2010-299, 48th AIAA Aerospace Sciences Meeting Including the New Horizons Forum and Aerospace Exposition, Orlando, FL, 4-7 Jan 2010.
3. Meyers, J., et al. "Diode Laser Absorption Measurements of Free Stream Hypervelocity CO<sub>2</sub> Flow at 1.6  $\mu\text{m}$ ," AIAA-2009-4326, 41st AIAA Thermophysics Conference, San Antonio, TX, 22-25 June 2009.
4. Li, H., et al. "Near-Infrared Diode Laser Sensor for Real-Time Equivalence Ratio in Gas Turbine Combustors." AIAA-2009-5522, 45th AIAA/ASME/SAE/ASEE Joint Propulsion Conference and Exhibit, Denver, CO, 2-5 Aug. 2009.
5. Wehe, S. D., et al. "Tunable Diode-Laser Absorption Measurements of Temperature, Velocity, and H<sub>2</sub>O in Hypervelocity Flows." AIAA-1997-3267 AIAA/ASME/SAE/ASEE Joint Propulsion Conference and Exhibit, 33rd, Seattle, WA, 6-9 July 1997.
6. Mohamed, A., et al. "Tunable Diode Laser Measurements on Nitric Oxide In A Hypersonic Wind Tunnel." *AIAA Journal*, Vol. 34, No. 3, 1996, pp. 494-499.
7. Galyen, N. and Plemmons, D. "Optical Mass Flux Sensor." AIAA-2010-4910, 27<sup>th</sup> AIAA Aerodynamic Measurement Technology and Ground Testing Conference, Chicago, IL, June 2010.
8. Walker, H., Phillips, W. "High Resolution Tunable Diode Laser Spectroscopy of Methane." AEDC-TR-85-37, March 1986.
9. Phillips, W. and Walker, H. "Nitrogen-Broadened Linewidths and Strengths of NO Utilizing Tunable Diode Laser Spectroscopy." *J. Chem. Phys.*, Vol. 85, 1986, pp. 3211-3216.
10. Lowry, H. S. and Fisher, C. J. "Line Parameter Measurements and Calculations of CO Broadened by H<sub>2</sub>O and CO<sub>2</sub> at Elevated Temperature." *J. Quant. Spectrosc. Radiat. Transfer*, Vol. 31, No. 6, 1984, pp. 575-581.
11. Sells, J. A. "Infrared Diode Laser Spectroscopy of Nitric Oxide." *J. Quant. Spectrosc. Radiat. Transfer* Vol. 25, 1981, pp.19-24.
12. Webster, C. R., et. al. "Quantum-Cascade Laser Measurements of Stratospheric Methane and Nitrous Oxide", *App. Opt.*, Vol. 40, No. 3, 2001, p. 321.
13. Phillips, M. C., Myers, T.L., and Taubman, M.S. "Broadly Tunable External Cavity Quantum Cascade Laser Development." US DoE, PNNL Report No. PNNL-17218, December 2007.
14. Martin, W. B. et. al. "Middle Infrared, Quantum Cascade Laser Optoelectronic Absorption System for Monitoring Glucose in Serum." *App. Spect.* Vol. 59, No. 7, 2005, p. 881.

15. Kosterev, A. A., et. al. "Effective Utilization of Quantum-Cascade Distributed-Feedback Lasers in Absorption Spectroscopy." *App. Opt.* Vol. 39, No.24, 2000, p. 4425.
16. Sonnenfroh, D. M., et. al. "Application of Balanced Detection to Absorption Measurements of Trace Gases with Room-Temperature, Quasi-CW Quantum-Cascade Lasers." *App. Opt.* Vol. 40, No. 6, 2001, p. 812.
17. Hancock, G., et. al. "Direct and Wavelength Modulation Spectroscopy Using a CW External Cavity Quantum Cascade Laser." *App. Phy. Let.* Vol. 94, 2009, p. 201110.
18. Birnbaum, G, "Microwave Pressure Broadening and Its Application to Intermolecular Forces." *Advances in Chemical Physics: Intermolecular Forces*, Vol. 12, ed. J.O. Hirschfelder, John Wiley & Sons, Inc. 2007, Hoboken, NJ.
19. Humlicek, J. "Optimized Computation of the Voigt and Complex Probability Functions." *J. Quant. Spectrosc. Radiat. Transfer*, Vol. 27, 1982, pp. 437-444.
20. Abrarov, S.M, et. al. "Rapidly Convergent Series for High-Accuracy Calculation of the Voigt Function." *J. Quant. Spectrosc. Radiat. Transfer*, Vol. 111, 2010, pp. 372-375.
21. Faddeyeva, V. N and Terentev, N. M. "Tables of Values of the Error Function for Complex Argument." Pergamon Press, New York, 1961.
22. McClatchey, R. A., et al. "AFCRL Atmospheric Absorption Line Parameter Compilation," Air Force Cambridge Research Laboratories Report AFCRL-TR-73-0096, January 1973.
23. Rothman, L. S., et al. "AFGL Atmospheric Absorption Line Parameters Compilation: 1982 Edition." *App. Opt.*, Vol. 22, No.15, August 1983, pp. 2247-2256.
24. Rothman, L. S., et al. "AFGL Trace Gas Compilation: 1982 Edition." *App. Opt.*, Vol. 22, No. 11, June 1983, pp. 1616-1627.
25. Rothman, L. S., et al. "The HITRAN Database: 1986 Edition." *App. Opt.*, Vol. 26, No. 19, October 1987, pp. 4058-4097.
26. Rothman, L. S., et al. "The HITRAN Molecular Spectroscopic Database and Hawks (HITRAN Atmospheric Workstation): 1996 Edition." *J. Quant. Spectrosc. Radiat. Transfer*, Vol. 60, No. 5, 1998, pp. 665-710.
27. Rothman, L. S., et al. "The HITRAN 2004 Molecular Spectroscopic Database." *J. Quant. Spectrosc. Radiat. Transfer*, Vol. 110, 2009, pp. 533-572.
28. Rothman, L. S. "The Evolution and Impact of the HITRAN Molecular Spectroscopic Database." *J. Quant. Spectrosc. Radiat. Transfer*, Vol. 111, 2010, pp. 1565-1567.
29. Rothman, L. S., et al. "HITEMP, The High-Temperature Molecular Spectroscopic Database." *J. Quant. Spectrosc. Radiat. Transfer*, Vol. 111, 2010, pp. 2139-2150.
30. Barber, R. J., et al. *Mon. Not. R. Astro. Soc.*, Vol. 368, Issue 3, 2006, pp. 1087-1094.
31. Tashkun, S. A., et al. "CDSD-1000, The High-Temperature Carbon Dioxide Spectroscopic Databank." *J. Quant. Spectrosc. Radiat. Transfer*, Vol. 82, 2003, pp. 165-196.

32. [www.bipm.org/en/publications/guides/](http://www.bipm.org/en/publications/guides/), Guides to the Expression of Uncertainty in Measurement.
33. Joint Committee for Guides in Metrology, "Evaluation of Measurement Data – Supplement 1 to the Guide to the Expression of Uncertainty in Measurements – Propagation of Distributions Using a Monte Carlo Method." 1<sup>st</sup> Ed., June 2008, JCGM 101-2008.
34. O'Byrne, S. "Diode Laser Sensor for Scramjet Inlets." AFOSR/AOARD Reference Number: AOARD-08-4019, 12 May 2010.

## APPENDIX A. WAVELENGTH MODULATED SPECTROSCOPY

Typically, a laser is wavelength modulated with a current ramp to scan the laser wavelength over the absorption feature of a spectral line. If  $I^o(\omega)$  represents the spectral intensity emitted at optical frequency  $\omega$ , then the attenuated signal through the absorbing media is given by

$$I(\omega) = I^o(\omega)e^{-k(\omega)} \quad (29)$$

where  $I(\omega)$  is the transmitted intensity and  $k(\omega)$  is the absorbance which is a function of temperature, pressure, and other molecular parameters. If the output of the laser is ramped in time the above expression can be expressed as function of time

$$I(t) = I^o(\omega_o + \alpha t)e^{-k(\omega_o + \alpha t)} \quad (30)$$

where  $\omega_o$  is the starting optical frequency and  $\alpha$  is the sweep rate which could range from sub-Hertz to a few kilohertz. Note the above expression is for one scan, after which another scan would start (i.e.,  $t = 0$ ). If one adds a small sinusoidal modulation onto the ramp signal, then the above becomes

$$I(t) = I^o(\omega_o + \alpha t + \beta \sin 2\pi f t)e^{-k(\omega_o + \alpha t + \beta \sin 2\pi f t)} \quad (31)$$

or simply

$$I(t) = I(\omega_o + \alpha t + \beta \sin 2\pi f t) \quad (32)$$

If one assumes that the dither frequency,  $f$ , is much larger than the scan rate (e.g.,  $f$  is on the order of +10 kilohertz vs. several hertz for the ramp scan rate), then at any particular moment in time the above can be represented by

$$I(t) \approx I(\omega'_o + \beta \sin 2\pi f t) \quad (33)$$

where  $\omega'_o$  is approximately a constant in comparison to the dither frequency term. If  $\beta$  is very small in comparison to  $\omega'_o$ , then we can expand the above in a Taylor series about  $\omega'_o$ .

$$I(t) \approx \sum_{n=0}^{\infty} \frac{I^{[n]}(\omega'_o)}{n!} (\beta \sin 2\pi f t)^n \quad (34)$$

Representing the sine function as complex exponentials

$$I(t) \approx \sum_{n=0}^{\infty} \frac{I^{[n]}(\omega'_o)}{n! 2^n} (-i)^n \beta^n (e^{i2\pi f t} - e^{-i2\pi f t})^n \quad (35)$$

Using the binomial expansion the power of the exponential term can be recast as

$$(e^{i2\pi ft} - e^{-i2\pi ft})^n = \sum_{k=0}^n (-1)^k e^{i2\pi ft(n-2k)} \binom{n}{k} \quad (36)$$

where the last term in parenthesis is the binomial coefficient. Combining the above equations one has

$$I(t) \approx \sum_{n=0}^{\infty} \sum_{k=0}^n \frac{I^{[n]}(\omega'_o)}{n! 2^n} (-i)^n (-1)^k \beta^n e^{i2\pi ft(n-2k)} \binom{n}{k} \quad (37)$$

The function  $I(t)$  can also be expanded in a Fourier series as

$$I(t) \approx \sum_{m=-\infty}^{\infty} C_m e^{i2\pi f t m} \quad (38)$$

where the coefficients are given by

$$C_m = \frac{1}{T} \int_0^T I(t) e^{-i2\pi f t m} dt \quad (39)$$

and  $T$  is the period or  $f^{-1}$ . Making the substitution into the above equation gives

$$C_m = \frac{1}{T} \sum_{n=0}^{\infty} \sum_{k=0}^n \frac{I^{[n]}(\omega'_o)}{n! 2^n} (-i)^n (-1)^k \beta^n \binom{n}{k} \int_0^T e^{-i2\pi f t(2k-n+m)} dt \quad (40)$$

Note the integral values are given by

$$\int_0^T e^{-i2\pi f t(2k-2-n+m)} dt = \begin{cases} 0 & 2k - n + m \neq 0 \\ T & 2k - n + m = 0 \end{cases} \quad (41)$$

Substituting back into Eq. (12) gives

$$C_m = \sum_{n=0}^{\infty} \frac{I^{[n]}(\omega'_o)}{n! 2^n} (-i)^n (-1)^k \beta^n \binom{n}{k} \text{ where } k = \frac{n-m}{2} \quad (42)$$

The fact that  $k$  is a positive integer will restrict possible values of  $n$  for a given value of  $m$ . Now consider the various cases:

$m = 0$  case

In this case  $k$  is an integer only for even values of  $n$ , and  $k$  has a value of  $n/2$ .

$$C_0 = \sum_{n=0,2,4..} \frac{I^{[n]}(\omega'_o)}{n! 2^n} (-i)^n (-1)^{n/2} \beta^n \binom{n}{n/2} \quad (43)$$

or

$$C_0 = I(\omega'_o) + \frac{I^{[2]}(\omega'_o)}{4}\beta^2 + \frac{I^{[4]}(\omega'_o)}{32}\beta^4 + \dots \quad (44)$$

m = 1 case

$$C_1 = \sum_{n=1,3,5..} \frac{I^{[n]}(\omega'_o)}{n! 2^n} (-i)^n (-1)^k \beta^n \binom{n}{k} \text{ where } k = \frac{n-1}{2} \quad (45)$$

and

$$C_{-1} = \sum_{n=1,3,5..} \frac{I^{[n]}(\omega'_o)}{n! 2^n} (-i)^n (-1)^k \beta^n \binom{n}{k} \text{ where } k = \frac{n+1}{2} \quad (46)$$

or

$$C_1 = -i \frac{I^{[1]}(\omega'_o)}{2} \beta + i \frac{I^{[3]}(\omega'_o)}{16} \beta^3 - i \frac{I^{[5]}(\omega'_o)}{384} \beta^5 + \dots \quad (47)$$

and

$$C_{-1} = i \frac{I^{[1]}(\omega'_o)}{2} \beta + i \frac{I^{[3]}(\omega'_o)}{16} \beta^3 + i \frac{I^{[5]}(\omega'_o)}{384} \beta^5 + \dots \quad (48)$$

m = 2 case

$$C_2 = \sum_{n=2,4..} \frac{I^{[n]}(\omega'_o)}{n! 2^n} (-i)^n (-1)^k \beta^n \binom{n}{k} \text{ where } k = \frac{n-2}{2} \quad (49)$$

and

$$C_{-2} = \sum_{n=2,4..} \frac{I^{[n]}(\omega'_o)}{n! 2^n} (-i)^n (-1)^k \beta^n \binom{n}{k} \text{ where } k = \frac{n+2}{2} \quad (50)$$

Note that in this case n = 0 is not possible since this would mean k > n, which is not allowed, thus

$$C_2 = -\frac{I^{[2]}(\omega'_o)}{8}\beta^2 - \frac{I^{[4]}(\omega'_o)}{64}\beta^4 - \frac{I^{[6]}(\omega'_o)}{768}\beta^6 + \dots \quad (51)$$

and

$$C_{-2} = -\frac{I^{[2]}(\omega'_o)}{8}\beta^2 + \frac{I^{[4]}(\omega'_o)}{64}\beta^4 - \frac{I^{[6]}(\omega'_o)}{768}\beta^6 + \dots \quad (52)$$

Keeping the first term in each expansion since  $\beta$  is assumed to be small and substituting back into Eq. (10) gives

$$I(t) \approx I(\omega'_o) + I^{[1]}(\omega'_o)\beta \sin 2\pi ft + I^{[2]}(\omega'_o)\frac{\beta^2}{4} \cos 4\pi ft + \dots \quad (53)$$

Therefore, if one selectively detects only the AC portion of the signal at the dither frequency, the intensity is proportional to the first derivative of the transmitted intensity. Likewise, detection at the first harmonic of the dither frequency, or a frequency of  $2f$ , and out of phase by  $\pi/2$  results in an intensity value proportional to the second derivative of the transmitted intensity. Note the key assumption in this derivation is that the amplitude of the dither,  $\beta$ , is assumed to be small.

## APPENDIX B. WING CORRECTION TO INTEGRATED ABSORBANCE CALCULATIONS

Integration of the absorbance profile is restricted to the spectral region available from the data. However, to correctly capture the true integrated absorbance one needs to integrate the absorbance over all optical frequencies. To develop a correction factor to the partially integrated absorbance profiles, consider Eq. (2) for the absorbance due to multiple spectral lines. Here, it is assumed the lines are due to one specie and the summation over species is dropped.

$$k(\omega) = \sum_j S_j f_j(\omega) \quad (54)$$

Applying the unit normality of the absorption profile,  $f(\omega)$  via Eq. (3), the integrated absorbance can be written as

$$\int_0^{\infty} k(\omega) d\omega = \sum_j S_j = \int_0^{\alpha} k(\omega) d\omega + \int_{\alpha}^{\beta} k(\omega) d\omega + \int_{\beta}^{\infty} k(\omega) d\omega \quad (55)$$

which can be rewritten as

$$\int_0^{\infty} k(\omega) d\omega = \int_{\alpha}^{\beta} k(\omega) d\omega \left[ 1 + \frac{\int_0^{\alpha} k(\omega) d\omega + \int_{\beta}^{\infty} k(\omega) d\omega}{\int_{\alpha}^{\beta} k(\omega) d\omega} \right] \quad (56)$$

Using the above equation one can express the integrated absorbance over all frequencies as the product of the absorbance integrated over a finite region, determined from measured quantities, times the correction factor in brackets evaluated from the approximate gas path and line parameter values. Thus we have:

$$\int_0^{\infty} k(\omega) d\omega = f(\alpha, \beta, S, \gamma, \omega_o, \chi, \eta, T) \int_{\alpha}^{\beta} k_m(\omega) d\omega \quad (57)$$

where  $f(\alpha, \beta, S, \gamma, \omega_o, \chi, \eta, T)$  represents the correction factor and the integral on the right is the integrated absorbance determined from the transmitted intensity.

Evaluation of the correction factor employed here utilizes trapezoidal integration over 10,000 steps using the Voigt spectral profile. The correction factor for cases examined in this work was as high as 10% of the measured integrated absorbance. The integrated absorbance was only required for the first two data reduction methodologies under consideration, LAINT and NLINT, that relied on integrated absorbances.

## APPENDIX C. PREDOMINATE SPECTRAL LINE PROFILES

The following figures illustrate the combined effect of temperature and pressure extremes on spectral line shape. The following spectral absorbances and transmittances were calculated based on the equations given Section 2.1. A constant integrated absorbance is assumed in all the calculations performed in this appendix to better illustrate only those effects that temperature and pressure have on the spectral line shape. In reality, an increase in temperature at constant pressure will decrease the integrated absorbance through its dependency on the molecular number density.

Three of the most predominately used spectral line profiles are presented: Doppler, Lorentz, and Voigt. These are discussed in Section 2.1. The profiles plotted are for the following conditions:

- Integrated Absorbance: 0.02
- Spectral Line Position:  $2000.0 \text{ cm}^{-1}$
- Foreign and Self Pressure Broadening Parameter:  $0.06 \text{ cm}^{-1}$
- Foreign and Self Broadening Temperature Correction Exponent: 0.75
- Molecular Weight: 25.0 gm/mole
- Temperature: 300 and 2,000 K
- Pressure: 0.01 and 1.0 atm

An ambient condition absorption profile is shown in Fig. C-1. Here, the temperature is 300 K at a pressure of 1 atm. Notice that in this particular case the pressure broadening is dominate with a HWHM of approximately  $0.06 \text{ cm}^{-1}$ , whereas the Doppler width is approximately  $0.0025 \text{ cm}^{-1}$ . Since the pressure broadening is many times greater than the Doppler broadening, the overall line profile is predominately Lorentzian in nature, and the Voigt profile is very near the Lorentz profile shape. Since the integrated absorbance is constant and represents the areas under absorption profiles, the narrow Doppler profile has a much higher peak absorbance. Figure C-2 is a plot of the absorbances at these conditions plotted to different scales so that the shapes of the profile are easier to visualize.

The effects of decreasing the pressure while maintaining the temperature is to reduce the pressure broadening while maintaining the Doppler width. Figure C-3 provides an example in which the pressure is 0.01 atm, resulting in a pressure-broadened HWHM of approximately  $0.0006 \text{ cm}^{-1}$ . In this instance the pressure broadening and Doppler broadening are of the same order, and the Voigt profile is broader than either the Doppler or Lorentz profiles. To better visualize the difference in the Lorentz, Doppler, and Voigt profiles at these conditions, a plot of only absorbance profiles over a narrower wave number range is provided in Fig. C-4.

An increase in temperature has the effect of decreasing the pressure-broadening coefficient. This results in a small pressure-broadening HWHM. Simultaneously, the Doppler HWHM increases with increasing temperature. The effects of these trends are easily seen by comparing Figs. C-1 (300 K and 1 atm pressure) and C-5 (2,000 K and 1 atm pressure). In Fig.

C-5, one notices that the Doppler profile is wider than in the ambient temperature case of Fig. C-1. Likewise, the increasing temperature has decreased the pressure broadening half-width.

Extreme conditions of small pressure-broadening effects are obtained by a simultaneous increase in temperature and decreasing pressure. Both these trends drive the pressure broadening smaller while the Doppler broadening increases with temperature. This scenario is illustrated in Figs. C-6 and C-7. In this particular case, the gas conditions are a temperature of 2,000 K and a pressure of 0.01 atm. Due to the extremely high temperature and low pressure, the pressure-broadening HWHM is approximately  $0.002 \text{ cm}^{-1}$ , whereas the Doppler-broadening HWHM is now approximately  $0.006 \text{ cm}^{-1}$ . This represents an opposite scenario from the ambient condition case illustrated in Fig. C-1. A wave number expanded plot of the absorbance profiles alone is shown in Fig. C-7. Notice that the Voigt profile more closely resembles the Doppler profile than the Lorentz profile for this extreme case.

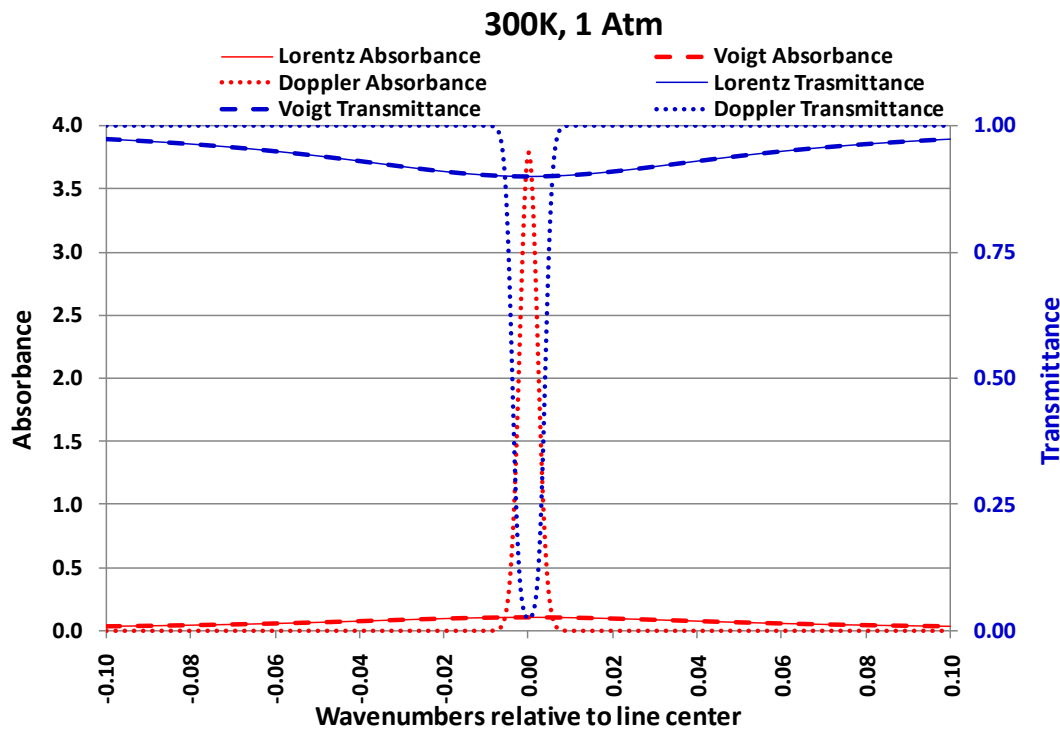


Figure C-1. Ambient Conditions (300 K and 1 atm) Spectral Line Profiles (Absorbances and Transmittance)

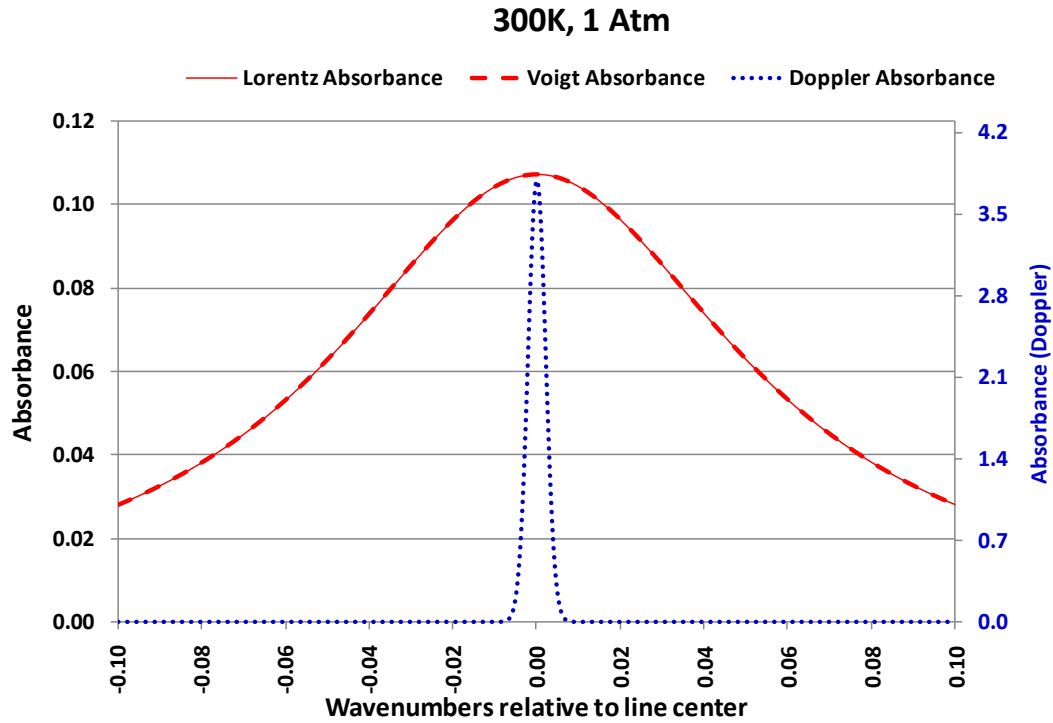


Figure C-2. Ambient Conditions (300 K and 1 atm) Spectral Absorbance Line Profiles

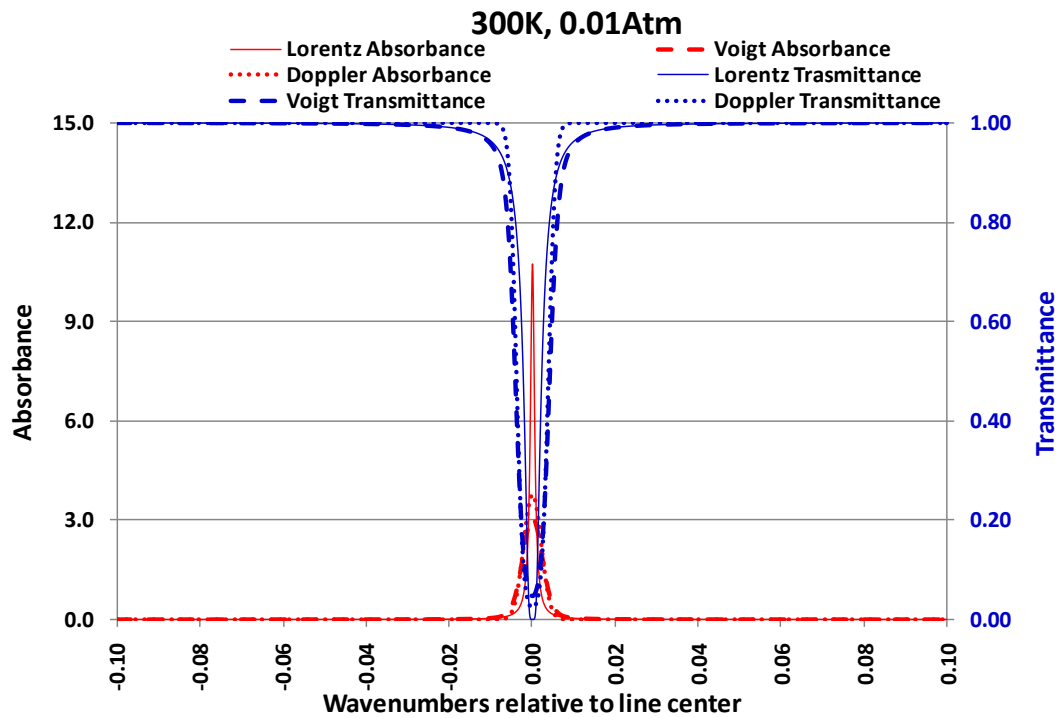


Figure C-3. Low-Pressure Absorbance and Transmission Profile at a Temperature of 300 K

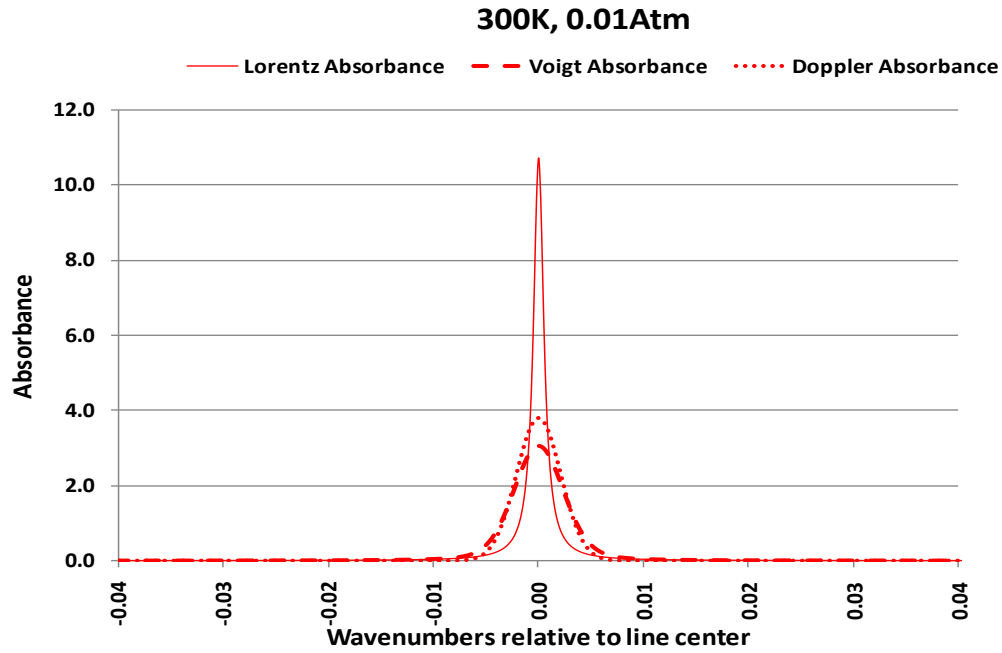


Figure C-4. Low-Pressure Absorbance Profile at a Temperature of 300 K

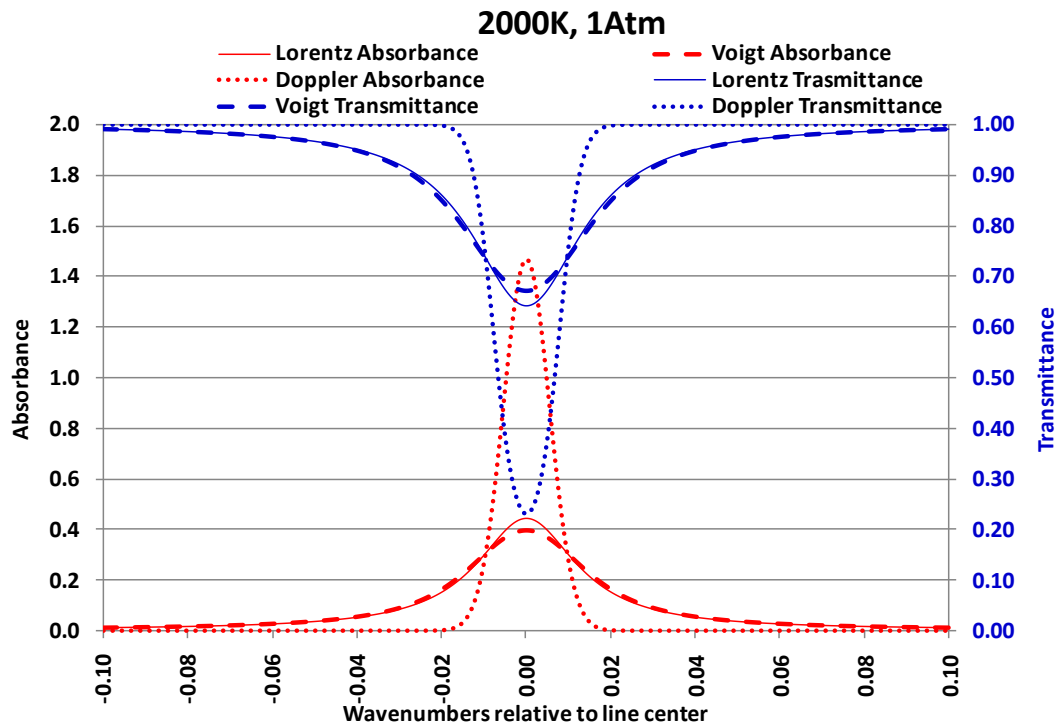


Figure C-5. Absorbance and Transmission Profiles at a Temperature of 2,000 K and 1 atm

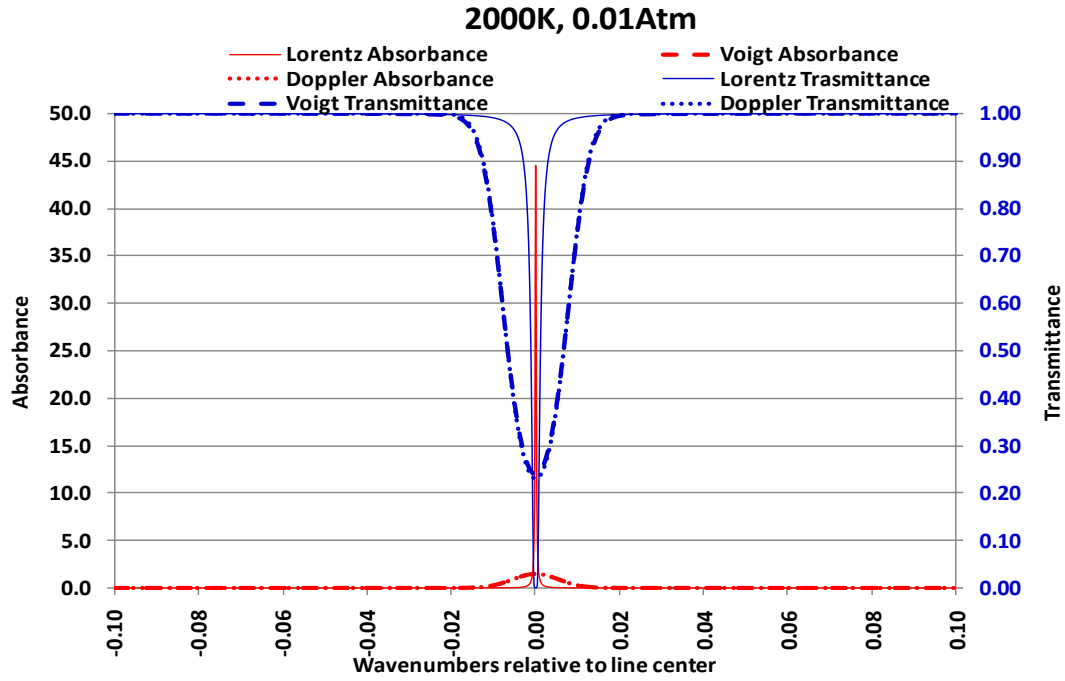


Figure C-6. Absorbance and Transmission Profiles at a Temperature of 2,000 K and 0.01 atm

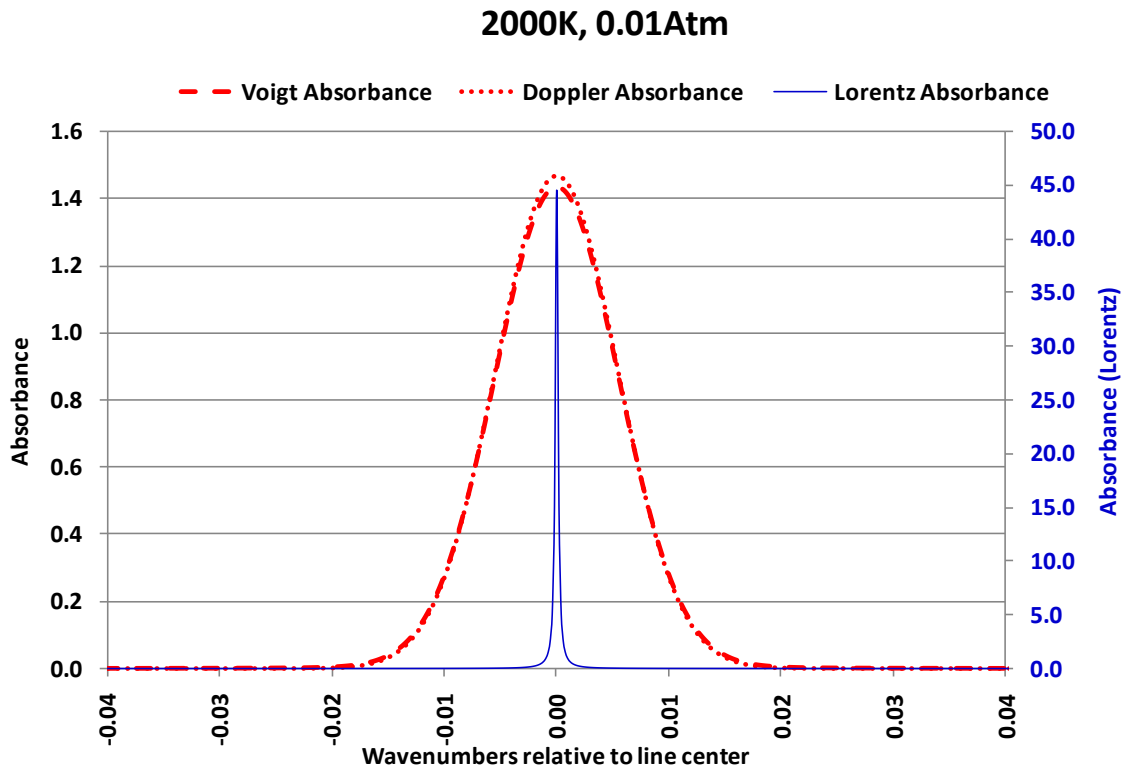


Figure C-7. Absorbance Profiles at a Temperature of 2,000 K and 0.01 atm

## NOMENCLATURE

$I(\omega)$	Spectral intensity [arbitrary units]
$I^o(\omega)$	Unattenuated spectral intensity or background [arbitrary units]
HWHM	Half width at half maximum
MC	Monte Carlo
$h$	Planck's constant [ $6.6260693 \times 10^{-27}$ erg sec]
$c$	Speed of light in vacuum [ $2.99292458 \times 10^{10}$ cm/sec]
$k(\omega)$	Absorbance [no units]
$l$	Path length [cm]
$S$	Integrated absorbance [ $\text{cm}^{-1}$ ]
$S^o(T)$	Line strength at temperature T [ $\text{cm}^{-1}/(\text{molecule}/\text{cm}^2)$ ]
$N$	Number density [molecules/ $\text{cm}^3$ ]
$N_{as}$	Number density of absorbing specie [molecules/ $\text{cm}^3$ ]
$N_T$	Total number density [molecules/ $\text{cm}^3$ ]
$f(\omega)$	Line shape function [cm]
$\omega$	Optical frequency [ $\text{cm}^{-1}$ ] Note: Reciprocal of wavelength in cm
$\chi$	Mole fraction [no units]
$P$	Pressure [atmospheres, unless otherwise stated]
$E$	Quantum state energy [ $\text{cm}^{-1}$ ]
$k$	Boltzmann's constant [ $1.3806505 \times 10^{-16}$ erg/K]
$g$	Quantum state degeneracy values [no units]
$\omega_o$	Optical frequency of a spectral line [ $\text{cm}^{-1}$ ]
$N_A$	Avogadro constant [ $6.0221415 \times 10^{23}$ molecules/mole]
$M_W$	Molecular weight [grams/mole]
$\gamma_D$	Doppler broadened half-width-at-half-maximum [ $\text{cm}^{-1}$ ]
$\gamma_L$	Lorentz or pressure-broadened half-width-at-half-maximum [ $\text{cm}^{-1}$ ]
$\gamma_L^o(T)$	Lorentz or pressure-broadening parameter at temperature T [ $\text{cm}^{-1}/\text{atm}$ ]
$\eta$	Pressure-broadening temperature exponent [no units]
$v$	Gas velocity [cm/sec]
$mf$	Mass flux [grams/( $\text{cm}^2$ sec)]
$T$	Temperature (Kelvin)